SPIN VALVE SENSOR ARRAYS FOR MAGNETIC BIO-LABEL DETECTION

A Dissertation

Presented to

the Faculty of the Department of Chemical and Biomolecular Engineering

University of Houston

in Partial Fulfillment

of the Requirements for the Degree

Doctor of Philosophy

in Chemical Engineering

by

Yu-Chi Liang

May 2014

Spin Valve Sensor Arrays for Magnetic Bio-Label Detection

Yu-Chi Liang

Approved:

Chair of the Committee
Dr. Dmitri Litvinov, Professor
Chemical and Biomolecular Engineering
Electrical and Computer Engineering

Committee Members:

Dr. Richard C. Willson, Professor
Chemical and Biomolecular Engineering

Dr. Gila Stein, Assistant Professor
Chemical and Biomolecular Engineering

Dr. Jiming Bao, Assistant Professor
Electrical and Computer Engineering

Dr. Paul Ruchhoeft ,Associate Professor
Electrical and Computer Engineering

Dr. Suresh K. Khator
Associate Dean
Cullen College of Engineering

Dr. Michael P. Harold
Professor and Chair
Chemical and Biomolecular Engineering

Acknowledgements

First and foremost, I would like to express my greatest gratitude to my advisor, Dr. Dmitri Litvinov for his invaluable and excellent guidance during these years. I appreciate all his contributions of funding, networking, ideas, and time to make my Ph.D. experience smooth, stimulating, and productive. The result-oriented guidance and insightful suggestion he gave me have greatly influence not only on my Ph.D. study but also the way I solve problems in my life. The freedom he gave me makes me conduct my research in a very efficient way and also allows me to have good research-life balance. He sets an excellent example as a successful professor. I feel very fortunate and honored to be one of his PhD students.

Furthermore, there are many past and present colleagues in Dr. Litvinov's group that I would like to acknowledge for their help during these years. I accept great assistance in my lab work particularly from Dr. Yi-Ju Wang, Dr. Long Chang, and Dr. Pawilai Chinwangso. I am thankful that they spent their treasure time to train me so that I was able to get accustomed to daily work in a short time. Thanks to Dr. Kelley Bradley, Alex, and Dr. Guo Jing's contribution, I can use facilities in the cleanroom without any problems. Without their assistance, I am unable to finish this project today. I owe so much to them. I also like to thank Dr. Zhen, DaHye, Ivan, and Gloria for their company. It is my pleasure to work with all of them.

My life without my dearest friends would be like the dawn without the sun. I am lucky to have so many great, kind, and thoughtful friends with me along the long road of pursuing my PhD. I appreciate the friendship with Dr. Chen-Chi Chu and Chao-Lun Mai.

They are not only my admirable role models but also the closest friends who I can share joy and sorrow feelings with. I would also like to thank my classmates I study with when we were in grips of heavy duty coursework in the first year. I owe all of my friends in greater Houston area a debt of gratitude for their thoughtful care of me. Most importantly, I would especially like to thank to a graceful and charming woman, Ching-Yi Wu. I love you from the bottom of my heart, but for you my heart has no bottom.

Words cannot describe my deep appreciation to my dearest parents, Jen-Ping Hsu, and Jimmy Liang for their unconditional love to me. I would like to dedicate my thesis to them to express my sincerest gratitude for their continuous education and full support throughout my life.

Last but not least, I thank Almighty God for bringing me through all the difficulties. His blessing never ends.

SPIN VALVE SENSOR ARRAYS FOR MAGNETIC BIO-LABEL DETECTION

An Abstract

of a

Dissertation

Presented to

the Faculty of the Department of Chemical and Biomolecular Engineering

University of Houston

in Partial Fulfillment

of the Requirements for the Degree

Doctor of Philosophy

in Chemical Engineering

by

Yu-Chi Liang

May 2014

Abstract

A spin-valve based biosensor array designed for the detection of magnetic bio-labels has been developed. A Co/Cu/Co/NiFe spin-valve design with a bottom Co layer pinned by a Co/Ru/Co synthetic antiferromagnetic tri-layer was employed. The Ta/Ru/Co/Ru/Co/Cu/Co/ $Ni_{81}Fe_{19}$ /Ta multilayer stack was deposited using UHV magnetron sputtering system. An external magnetic biasing field was applied during deposition to magnetically bias $Ni_{81}Fe_{19}$ layer to further control magnetization orientation of the free (top) Co layer. The deposition conditions and thickness of individual layers were carefully optimized to maximize the GMR ratio to 13% in unpatterned films.

In order to fabricate nano-scale GMR based biosensors from multi-layer stack, new processes including optical and e-beam lithography were designed and conducted. The use of a new electron beam bilayer resists comprised of poly-(4-hydroxystyrene) (PHOST) as the top layer and poly-(dimethylglutarimide) (PMGI) as the bottom layer is demonstrated. Twelve 400nm × 400nm sensors on a chip were built. GMR peaks corresponding to antiparallel magnetization configuration over a base line corresponding to parallel magnetization configuration of the Co layer in the spin-valve stack was observed. Several sizes and numbers of Fe_3O_4 nanoparticles attaching over sensor surface resulted in a significant change of the GMR peak profile.

Micro-magnetic simulation was also conducted in attempt to explain magnetic behavior of particle-sensor interaction. The trend effect of a magnetic particle on sensor GMR profile was confirmed. The simulation results were strongly consistent with those from experiments.

Table of Contents

List of Figures

List of Tables

Chapter 1. Introduction

GMR-based spin-valve (SV) devices have been intensely and widely developed for different varieties of applications, including read/write heads in hard disk drives, and magnetic random access memories (MRAM). In recent years, a novel application of GMR-based spin-valve sensors on biomolecular detection and biomedical diagnosis has been increasingly received much attention and studied [1-3] .

In the magnetic bio-detection scheme, the GMR-based spin-valve sensor for biomolecular detection involves magnetic micro- or nano-scale particles as labels on which biomolecules attach with specific binding. The area above the spin-valve is defined as the biological sensing area on which specific biomolecules are usually deposited. This creates the ability to recognize specific biomolecules on the magnetic particle surface. Numbers of design and approaches for sensing biomolecules, such as proteins [4, 5], peptides [6] and DNA [7, 8] have already been well established. Figure 1.1 is an example showing how a GMR based sensor detects streptavidin-binding magnetic particles. When those magnetic particles with a streptavidin surface bind with biotins on the sensor surface, the magnetic fringing field from the attached magnetic particles would lead to the resistance signal change of the sensor under a given external field. Those particles which do not bind on the sensor can be either pulled off by a vertical external magnetic field or screened out by other approaches. Allowing only a few or single particles attaching on the sensor surface reduces influence of background particles; therefore, it improves resistance change signal. A magnetic based biosensor is sometimes embedded with a micro-fluidic delivery system which is able to carry a few or

single bio-label magnetic particles to the designated sensing area [9].

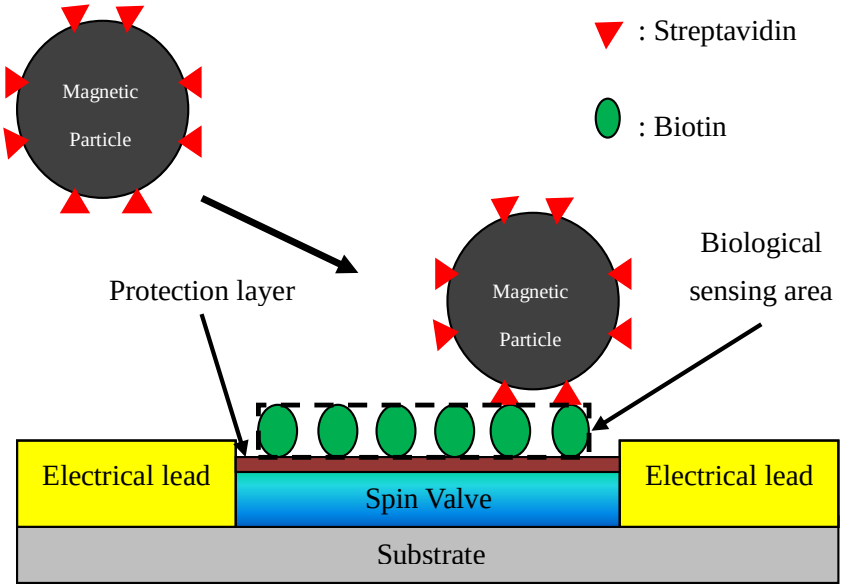

Figure 1.1: The schematic illustration of magnetoresistance-based biosensor detection.

Three major parts in magnetic biosensor development need to be studied: magnetic multi-layer preparation, the sensor fabrication process, and choice of suitable magnetic particles. Spin-valves as GMR sense elements are usually composed of multi-layer thin films, commonly a ferromagnetic/non-magnetic/ferromagnetic tri-layer. Many derivatives from this tri-layer have also been studied in order to achieve a large GMR effect and high sensitivity. In addition to the fabrication processes, design and development of the robust GMR materials for low-field application is also important. Many similar structures, derived from Dieny et al. [4], of GMR multi-layers have been investigated and put into practice [10, 11]. For this project, we deposited our GMR multi-layer stack incorporated with a synthetic antiferromagnetic (SAF) tri-layer. SAF usually consists of two ferromagnetic layers separated by a thin Ru layer such as Co/Ru/Co [12]. The three layers

are strongly and periodically antiferromagnetic coupled as the Ru layer thickness is thinner than 1 nm [13]. The reasons for employing a SAF tri-layer are that many studies have proved theoretically and experimentally that synthetic antiferromagnetism (SAF) has a higher magnetic and thermal stability than antiferromagnetic (AF) materials. In other words, SAF is able to enhance the sensor's overall stability and performance [14-16]. In addition, since the sensor is designed for low-field application, a permalloy layer was added as part of the free layer. By doing this, the coercivity of the overall GMR multi-layer stack can be lowered.

The dimension of the sensor should be designed to compromise between the signal-to-noise and biological sensing area. Since sensor resistance increases with the increasing length-to-width ratio of the sensor dimension, the sensor length cannot be too long as the sensor width is fixed. High resistance would lower the GMR ratio and make the sensor hard to measure. On the other hand, if the sensor length is too short, there is not enough area to detect bio-magnetic particles, leading to a low sensing capability.

In previous studies, sensors were made with a relatively large sensor-to-nanoparticle-size ratio. Those sensors had low sensitivity and difficulty sensing such particles whose size are 500 nm or less in diameter. In this research, our goal is to build a magnetic sensor which is able to conduct single magnetic nanoparticle detection. Sensors with high sensitivity have to be developed in order to be capable of detecting those magnetic nanoparticles which have smaller magnetic moments than micro-scale magnetic particles. To achieve this, it requires a new design and approach to achieve higher sensor sensitivity with a smaller sensing area, specifically for a sensing single magnetic nanoparticle. In order to achieve high sensitivity of bio-recognition, the dimension of the

spin-valve sensing area should also be scaled down to several hundred nanometer by several hundred nanometers. However, due to the limit of present lithography processes, the size of existing spin-valve biosensors is too large for sensing nanoparticles. In order to fabricate a sensor whose size is relatively comparable to a nanoparticle, a fabrication process based on a self-aligned lithography method which has been widely adopted in the semiconductor industry is introduced in this article [17, 18]. Haifang Yang et al. [19] illustrated a method using the bilayer resist system for the negative tone lift-off process to generate a 200 nm thin-line pattern with undercut profile. Based on their case, a metal layer as a contact layer can be deposited on the whole substrate except on the patterned portion. This achievement sheds light on the issue of self- aligned contact connected to the nano-scale sensing area. To fabricate a less than 1 μm^2 sensing area, a novel and complex sensor fabrication process is designed and built. In our sensor fabrication processes, nano-scale GMR-based biosensors were fabricated using a combination of optical and e-beam lithography (EBL). Negative tone bi-layer resist was used here for EBL in order to define the sensing area and obtain self-aligned contacts. There are two main advantages to using the negative tone bi-layer resist system to fabricate GMR-based spin-valve biosensor. First, fabricating self-aligned contacts with the negative tone bi-layer system avoids a very long waiting time for conducting the e-beam exposure of a large defined electric contact area on the positive tone bilayer resist system. Second, by using the negative tone bi-layer resist system, the sensing area can be defined after sputter depositing the GMR multi-layer stack, allowing one to obtain better controlled magnetic characteristics of the patterned GMR multi-layer stack, compared to using the positive tone bi-layer resist system.

Some studies have developed using hydrogen silsesquioxane (HSQ) resist in their negative tone bilayer system [20, 21]. However, HSQ has a serious aging effect and scum problems which require optimizing processing conditions frequently [22]. Therefore, in our study, an alternative bilayer resist system without using HSQ has been developed.

A new negative tone bilayer resist system comprised of poly(4-hydroxystyrene) PHOST as a top layer and poly(methylglutarimide) (PMGI) as a bottom layer was developed for self-aligned contacts fabrication. PHOST developed by IBM [23, 24] has long been used as a good photoresist in 248 nm UV lithography because of its stability and low cost. It was also found that PHOST was a potential negative electron beam resist [25]. The bottom layer, PMGI , which has usually been used as an efficient lift-off resist incorporating with PMMA, LOR [26], was deployed here for undercut configuration. Although PMGI as an underlayer may generate over-cut profiles which cause destruction of the bilayer system, our fabrication procedure successfully overcame this problem. The detailed processes of using this bilayer resist system to fabricate self-aligned contacts connecting on defined metallic patterns will be demonstrated in this thesis. By using this newly developed bilayer system, we can successfully define and scale down the magnetic spin-valve biosensor dimension to 400 nm × 400 nm, which is an ideal dimension for nano-scale magnetic particle detection.

A biosensor is required to be designed to protect against damage or corrosion when any measurement is conducted. Phosphate buffered saline (PBS) solution is commonly used for bio-storage or a biological buffer solution [27]. Bio-conjugated magnetic particles are designed to be carried in the PBS fluid to the sensing area. This salted solution may conduct electrolysis and further cause serious damage to the sensor due to

the strong acid/base ions in the local area nearby the electrodes when current is applied on the sensor during the GMR measurement. Therefore, the sensor corrosion effect of the phosphate buffered saline (PBS) solution has also been investigated. A passivation layer, Al_2O_3, was employed and investigated to protect the sensor from corrosion.

Magnetic particles used as labels can be classified by size. The larger ones, in micro-scale, have been widely used nowadays [28]. They can be made in a consistent shape and size which allow easy quantitating of the relationship between the signal of resistance change and the number of particles detected upon a defined sensing active area. In addition, those micro-scale particles, in comparison to nano-scale particles, have a higher magnetic moment per label which produces a stronger fringing field. A stronger fringing field, theoretically, is able to express more resistance change signals which can be more easily detected by the sensor. However, with their inherited large size, they obstruct intense density receptor-ligand binding across the sensing area. The smaller magnetic particles, in nano-scale, can avoid this problem. Nevertheless, at this writing, due to fabrication difficulties, most commercial magnetic nano-particles are not consistent in size and shape. Besides, due to their high magnetization and anisotropy per unit volume, they easily aggregate with each other, leading to difficulty of dispersion on the sensor surface.

The magnitude of the magnetic resistance (MR) profile change of the sensor would be limited not only by sensor capability but also by the magnetic moment of the particle. A magnetic particle with high magnetic moment and single domain is a good candidate for single magnetic particle detection. Several types of magnetic nanoparticles and robust particle synthesis approaches have been published [29-32]. By considering the size of

general biomolecules such as fragments of DNA, RNA, and several sequence of amino acids, nano-scale magnetic particles instead of micro- ones are more size-suitable for those biomolecules [33]. More accurate quantitative analysis of binding biomolecules can be obtained by reducing non-specific particle binding and improving dispersion of the magnetic particles on sensor surface during the detection

Not only are the experimental results of the GMR profile change of single Fe_3O_4 magnetic nanoparticles attaching onto the sensor presented in this thesis, but also micro-magnetic simulation data was recorded. Micromagnetic simulation is able to explain the magnetic behavior of either a sensor or a magnetic particle in a micro-scale perspective and the tendency of the particle detection. Several magnetic parameters of a sensor and a particle were tested and optimized in this thesis. Particle-sensor models describing the effect of micro-magnetic behavior between a particle and a sensor on the GMR profile were investigated. The strong consistency between simulation data and experimental results is also presented in this thesis.

Chapter 2. Background Review

2.1 Giant Magnetoresistance (GMR)

The giant magnetoresistance (GMR) effect is the phenomenon resulting from a large change in electrical resistance induced by an external magnetic field. Materials exhibiting GMR effect are usually thin films composed of different ferromagnetic and nonmagnetic layers. The resistance change is related to the field-induced alignment of the magnetization orientation of the magnetic layers. Different magnetization orientations are derived from the alternating spin states of the electrons, which leads to the change of the electrical conductivity in ferromagnetic materials. The GMR was discovered in 1988 by Albert Fert [34] on Fe/Cr (001) multi-layers. In the first study of GMR, the film was composed of layers of Fe (ferromagnetic) and Cr (nonmagnetic) with typical thicknesses of a few nm, and the current was applied to the in-plane direction of the film, as shown in Figure 2.1. Their research also interpreted the GMR effect in terms of spin dependent scattering. Peter Grünberg [35] also found GMR on Fe/Cr/Fe (001) tri-layers during the same period. Several years before GMR was found, scattering experiments conducted by Grünberg's group [36] had already proven that two Fe layers separated by a less than 1nm thick Cr layer were anti-ferromagnetically coupled. Figure 2.1 C) illustrates the mechanism of the GMR effect. In the parallel magnetic configuration, free electrons in one type of the spin states is able to pass easily through all the layers, causing a short circuit in this channel. The mean free path of such free electrons is long, leading to low resistance. On the other hand, in the anti-parallel configuration, free electrons in both spin

states are hindered and transmitted slowly. The mean free path of all free electrons is short, causing the high resistance [37].

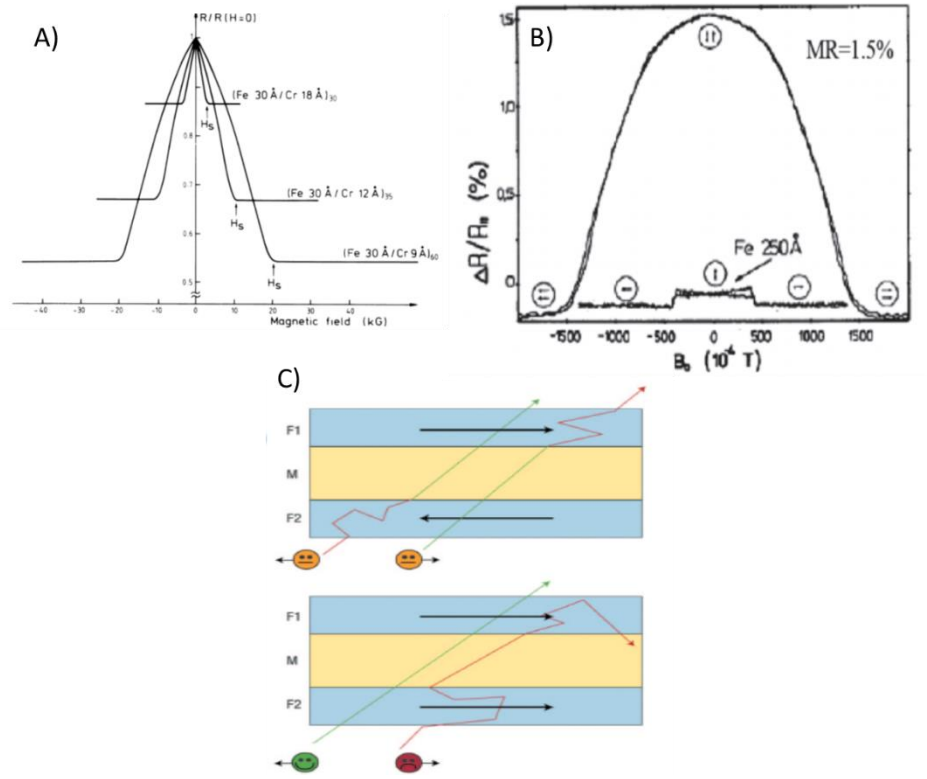

Figure 2.1: The discovery of giant magnetoresistance from two independent groups: A) On Fe/Cr (001) multi-layers [34]. B) On Fe/Cr/Fe tri-layers [35]. C) Schematic illustration of the mechanism of the GMR. [37].

After the discovery of GMR, attention was quickly drawn to it because of the many possibilities of applications and interests of the fundamental. In 1990, Parkin's group [13] presented the existence of GMR in multi-layers (Fe/Cr, Co/Ru and Co/Cr). They also found the variation of the magnetoresistance attributed to the oscillations of the interlayer exchange coupling as a function of the spacer layer thickness. GMR effect vanishes when the coupling is ferromagnetic, and reappears in the thickness ranges where the coupling is antiferromagnetic (AF), as shown in Figure 2.2. This oscillation behavior is only valid

when the thickness of the spacer layer is only a few nm, where the exchange coupling is stronger than the coercivity of the multi-layers. Another important result, as shown in Figure 2.2 B), was the discovery of the behavior of large oscillations on the GMR effect in Co/Cu multi-layers, which gradually becomes basic GMR components. Last but not least, the highest GMR ratio, 220%, was obtained by Schad et al. [38] from investigating Fe/Cr multi-layers.

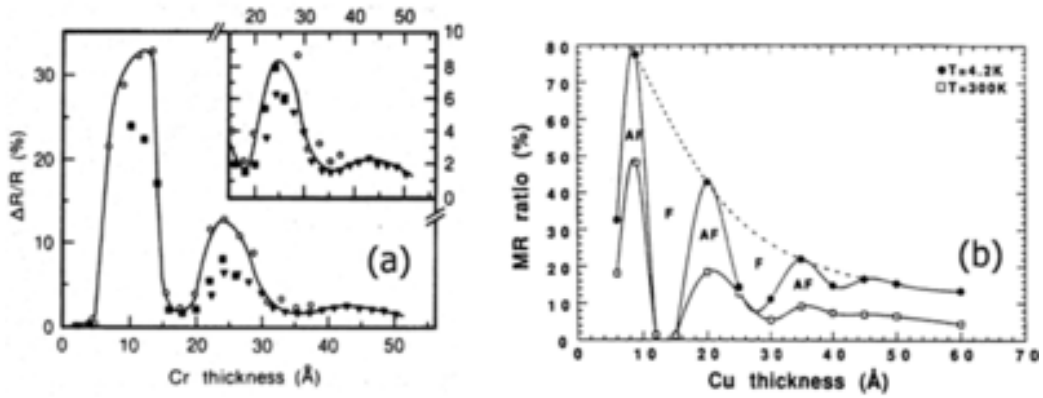

Figure 2.2: The variation of the oscillation of the GMR ratio as a function of the nonmagnetic layers thickness in A) Fe/Cr [24] and B) Co/Cu multi-layers [39].

2.2 Spin-Valve

A spin-valve (SV) device is generally composed of two ferromagnetic layers separated by a non-magnetic spacer layer, in which the GMR effect presents. Typical multi-layer structures used in a spin-valve device include $Co_{90}Fe_{10}/Cu/Co_{90}Fe_{10}$ [40], $[Co/Cu/Co]_n$ [41-43], and $[Ni_{80}Fe_{20}\,(Py)/Cu/Co]_n$ [44] . The GMR effect in the spin-valve is based on the fact that a parallel configuration of the magnetizations in the multi-layers can be switched into an anti- parallel one by applying an external magnetic field. One of the spin-valve types includes multi-layers combining hard and soft magnetic layers. The

GMR effect can be observed by solely switching the soft layer [45, 46]. Another spin-valve type in which an extra antiferromagnetic layer is added was also developed [47]. With the addition of an antiferromagnetic layer, the magnetization of one of the magnetic layers is pinned by interaction with an antiferromagnetic layer. As a result, the GMR effect can be enhanced.

Two major designs of the spin-valve device are current perpendicular-to-plane (CPP) and current in-plane (CIP), as shown in Figure 2.3. The CPP component is usually designed as an important element of the read/write head of hard disk drives [48-50]. On the other hand, GMR effects can also be obtained with the current in-plane to the layers. The CIP design is broadly adapted for fabricating magnetic sensors, including the one developed in this thesis [51, 52].

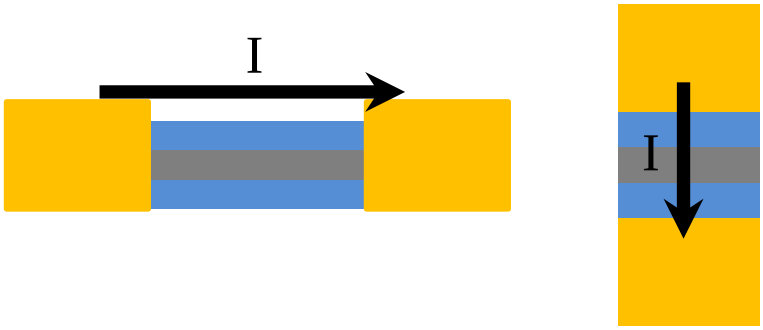

Figure 2.3: The example of A) CIP B) CPP design for GMR device.

2.3 Synthetic Anti-ferromagnetism

Materials which exhibit antiferromagnetism have electron spins aligning in one orientation with neighboring electron spins aligning in the opposite one, constructing a repeating pattern, as shown in Figure 2.4. Materials such as FeMn, IrMn, and NiMn are common antiferromagnets [53]. Although a high exchange bias can be observed by

depositing those antiferromagnets in SV device at room temperature, a blocking temperature above which the pinning field decreases drastically and magnetic property becomes unstable is relatively low [54]. Furthermore, when the thickness of the SV is in the sub-micrometer

range, the presence of the demagnetizing field can cause the loss of the pinning ability which can no longer completely fix the pinned layer [55].

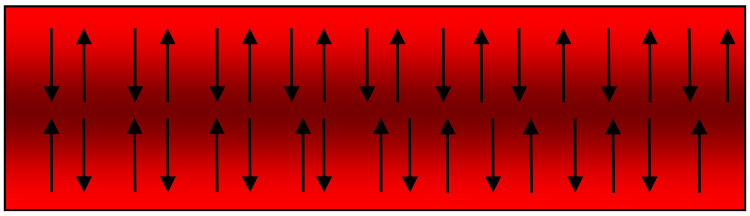

Figure 2.4: Schematic diagram of spin alignment in antiferromagnet.

Due to these drawbacks, a new approach for expressing antiferromagnetic characteristics is to develop a synthetic component called synthetic antiferromagnet (SAF). The configuration of SAF, usually a tri-layer structure, is predicted by the RKKY theory [13, 56, 57]. The RKKY theory illustrates interlayer coupling within multi-layers of magnetic layers separated by a non-magnetic spacer layer, a Ru layer. The magnetic characteristics were found to oscillate between antiferromagnetic and ferromagnetic as a function of the thickness of Ru layer, as shown in Figure 2.5. With higher thermal and magnetic stability, SAF is a promising antiferromagnetic material to be applied to magnetic-based sensor fabrication [12]. In this research work, interlayer exchange coupling in a synthetic antiferromagnet, Co/Ru/Co, depending on the thickness of the Ru layer was investigated. The magnetic characteristics when applying such tri-layer structure to the multi-layer SV films was also investigated.

2.4 Biomolecular Detection Scheme

The idea of magnetoresistance-based sensors applied in the biomolecular recognition field was first proposed by Shieh and Ackley in 1997 [58]. In 1998, the Baselt group [59] demonstrated the prototype of a giant magnetoresistance based biosensor. In their bio-detection scheme, magnetic micro-particles were used as labels for biomolecules and were detected by 80 μm × 5 μm magnetoresistive transducers in which the sensing element was composed of GMR multi-layer sandwich film developed by Dieny et al. [60] in 1994.

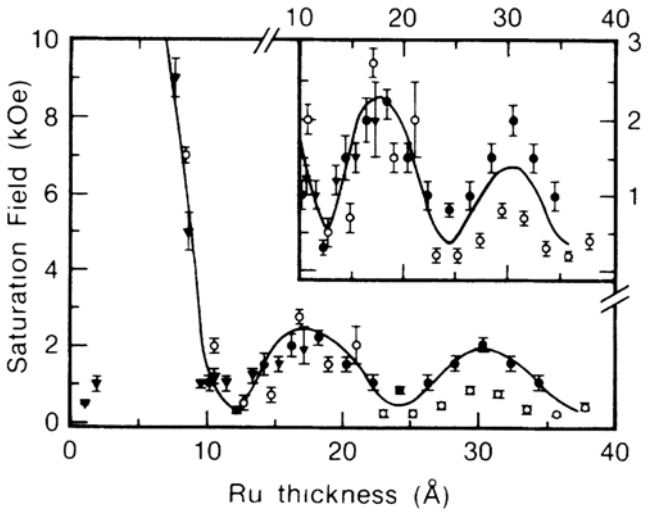

Figure 2.5: The illustration of RKKY oscillatory variation as a function of Ru thickness [24].

In the past several years, Wang's group from Stanford University has achieved a series of significant breakthroughs related to sensing a large number of bio-conjugated magnetic nanoparticles using GMR sensors [3, 61-64]. The result showed that bio-sensing was achieved by using an array of 32 pairs of GMR sensors. Each sensor consists of 32 sensing strips with a dimension of a 93 μm × 1.5 μm active area. Their research has established the latest prototype of the magnetic biosensor and has provided great

contributions to magnetic bio-sensing.

2.5 Magnetic characteristics

2.5.1 Hysteresis loop

Hysteresis loops, also known as magnetization curves, have been used widely to illustrate the magnetic characteristic of a specific material. The shape of the hysteresis loop describes the characteristics of the magnetic properties of a magnetic material and illustrates the reluctance with which it is magnetized as well as the ability to retain magnetization. A hysteresis loop can be determined from the measurement using instruments like MOKE, VSM, or AGFM, etc.

From a hysteresis loop, one can tell the change of magnetization, M, depending on applied field strength, H. Figure 2.6 shows a typical hysteresis loop corresponding to several key magnetic states with magnetic domain motion in a ferromagnetic material [65].

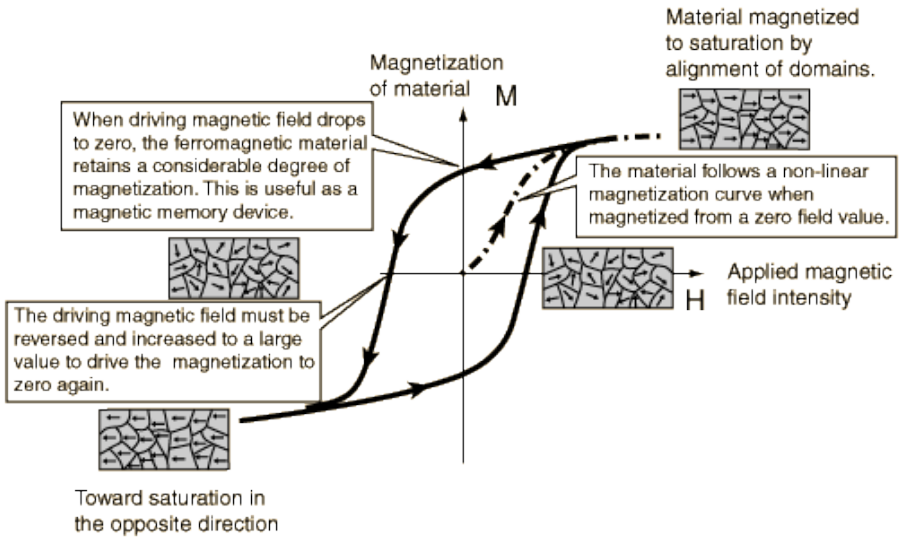

Figure 2.6: The hysteresis loop and corresponding magnetic domain motions at certain states of a ferromagnetic material [65].

There are several important magnetic properties that can be obtained from a hysteresis loop:

- Coercivity (H_c): Strength of the reverse magnetic field required as the magnetization of the material returns to zero. In other words, coercivity represents the resistance of a ferromagnetic material tending to be demagnetized.
- Remanence (H_r): Strength of magnetization remaining in a ferromagnetic material as an applied magnetic field is zero. In this state, a considerable degree of magnetic domains remain along the orientation of the saturation magnetization. It is a magnetic property specific to ferro- or ferri- magnetic materials.
- Saturation magnetization (M_s): A state above which the magnetization of the material is not able to increase further even as higher external magnetic field applies. At this state, the all magnetic domains align along the same orientation.
- Squareness ratio (SQR): Ratio of Mr and Ms. It is essentially a degree of how square the hysteresis loop is. Generally speaking, materials considered to be good recording medium have large squareness values.
- Permeability (μ): Ratio of the magnetic flux B and the applied field H. It illustrates a relative increase in the magnetization inside a material compared with the applied field in which the given material is placed.

One can also differentiate the magnetic types of a material from the shape of the curve. In addition to the ferromagnetic hysteresis loop shown in Figure 2.6, the other typical hysteresis loops of diamagnetic, anti-ferromagnetic, and paramagnetic materials are shown in Figure 2.7.

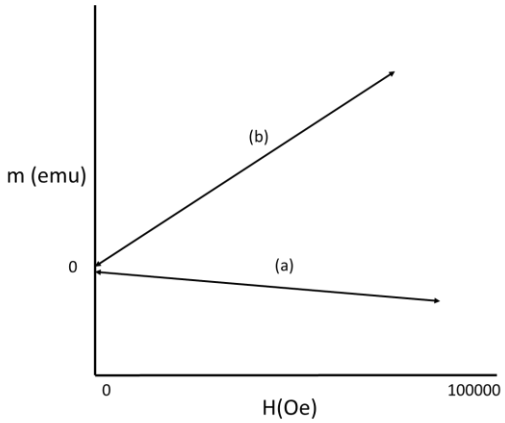

Figure 2.7: The hysteresis loop of a A) diamagnetic and B) paramagnetic or anti-ferromagnetic material.

2.5.2 Magnetoresistive curve

A magnetoresistive (MR) curve, as shown in Figure 2.8, illustrates the change of the electrical conductivity of a material under the appearance of various external magnetic fields by plotting the resistance versus the alternating external field. Some special magnetic components such as spin-valve or Fr/Cr multi-layer show a larger MR than other common magnetic materials. This large MR is called giant magnetoresistance (GMR). In a spin-valve device, starting from a certain high external field, the magnetization of two ferromagnetic layers are both saturated along the same direction, expressing a low resistance state. As the field decreases to zero, hysteretic behavior causing magnetoresistance remains at a low state. However, as the applied field increases toward to the direction opposite the previous saturation field, two ferromagnetic layers flip non-concurrently, which generates a higher resistance state. To quantify the GMR effect, the resistance change can be written as

$$\text{GMR Ratio} = \frac{R_{ap} - R_p}{R_p}, \qquad \text{(Eq. 2-1)}$$

where R_{ap} and R_p are the resistance of the antiparallel and parallel magnetization configuration, respectively [66].

The ratio of resistance change and the required coercive field depends on metal types and interlayer exchange coupling. In a spin-valve structure, adding an anti-ferromagnetic layer allows for a pinning field to be generated within the spin-valve structure. Such pinning field generates an antiferromagnetic exchange coupling with the proximity to the ferromagnetic layer, called the pinned layer. As the magnetization orientation of the pinned layer is fixed, the other ferromagnetic layer called a free layer, usually separated by a spacer layer, is able to flip freely under the given external magnetic field. Many studies has been verified that by adding a antiferromagnetic layer to the spin-valve structure, a significant increase of the GMR effect, compared with the spin-valve structure without any antiferromagnetic layer, can be obtained [67-69].

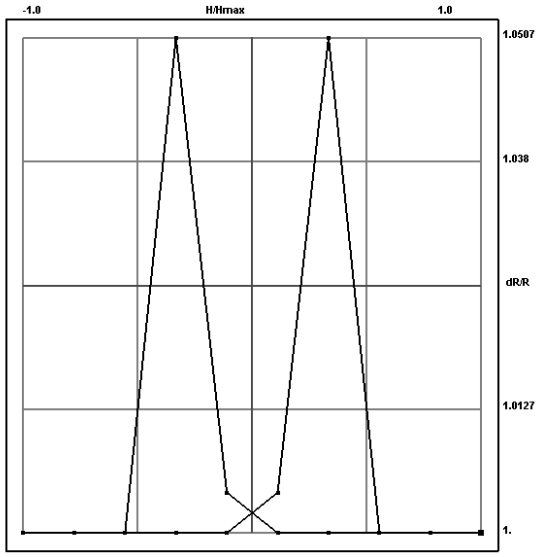

Figure 2.8: Simulated GMR curve corresponding to applied field.

A GMR curve usually has symmetry about the vertical axis, indicating that the positive and negative cases are identical and have nothing to do with the resistance change. The half-width of the peak represents the coercivity of the material. A position shift of the peak along the horizontal coordinate or the width of the peak change in the GMR curve implies the change of the pinning field within the spin-valve structure.

2.6 Fabrication

2.6.1 Resists

The function of resists is to form a patterned surface with designed textures. The resist material, usually a polymer, is chemically changed after exposure under an energy source, leading to alteration of composition and solubility.

Based on the energy sources for the exposure, resists can be classified into two major distinctive groups: photoresists, and e-beam resists. Photoresists are light-sensitive and have been widely used in both industrial and lab processes, particularly in the semiconductor industry. The light source used for photolithography includes UV (405 nm or 365 nm wavelength), DUV (248 nm, or 193 nm wavelength), or EUV(less than 193 nm wavelength) [70]. Table 2.1 summarizes several common photoresists and their operational exposure wavelength [23, 71-74].

Table 2.1: Several common photoresists.

Photoresist	Manufacturer	Tone	Exposure wavelength(in nm)
AZ-1512	AZ	Positive	350-450
SU-8	MicroChem	Negative	350-400
PMMA	MicroChem	Positive	193-248
PHOST	Sigma-Aldrich	Negative	193-248
LOR	MicroChem	Positive	240-290

Electron beam (e-beam) resists, instead of being exposed under an energy source from light, are defined when the exposure process uses an e-beam as an energy carrier. The mechanism of e-beam resist exposure is similar to UV exposure. However the major difference is that electrons carry their energy gradually into the resist, and scatter within the molecules in the resist during exposure, while photons are absorbed by the resist, depositing all their energy at once. Table 2.2 summarizes several important e-beam resists, their tones, and required doses.

Table 2.2: Several common e-beam resists.

E-beam resist	Manufacturer	Tone	Required dose (in $\mu C/cm^2$)
PMMA	MicroChem	Positive	500
		Negative	>10000
PMGI	MicroChem	Positive	1000
PHOST	Sigma-Aldrich	Negative	8500
ZEP	Zeon Chemicals	Positive	30

Some photoresists can also be exposed by the e-beam, leading to the same result as exposure under light. PMMA and PHOST are two of those that can form a patterned surface by either light or e-beam [25,75].

The exposure process alters the chemistry of the resist and changes its solubility relative to the unexposed resist. Based on this solubility change, resists can also be categorized into two distinctive types: negative tone and positive tone, as shown in Figure 2.9.

When a positive resist is exposed to an energy source, the energy breaks specific bonds in the long-chain polymers of the resist, causing them to be cut into shorter fragments and thus more soluble than unexposed areas. As a result, exposed areas are easily dissolved

and washed away by using a proper developer, leaving behind a positive image of the mask pattern. On the contrary, when a negative resist is exposed to an energy source, it causes cross-linking between the resist polymers, leading to more bond bindings in the resist and thus making the exposed areas less soluble than unexposed areas. As a result, exposed areas remain on the substrate, leaving behind a negative image of the mask after unexposed areas are dissolved and washed away by using a proper solvent or developer. Several resists such as PMMA can be either positive or negative tone depending on the applied dose or light intensity. For example, PMMA as an e-beam resist can be positive tone while the applied dose is around 500 $\mu C/cm^2$, and turn to negative tone when the applied dose increases to 10000 $\mu C/cm^2$ [76].

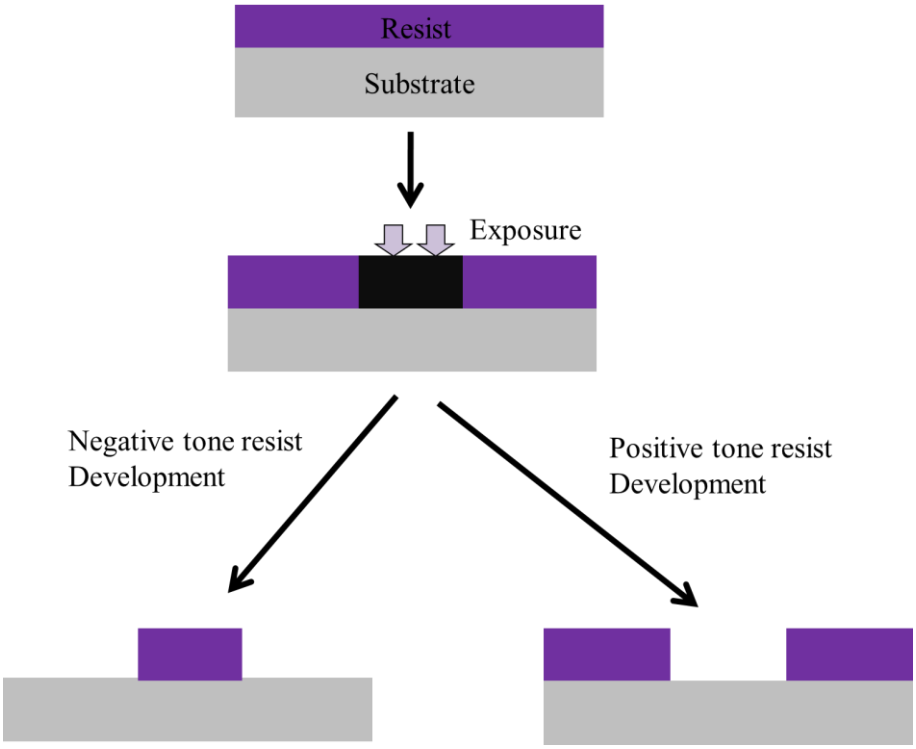

Figure 2.9: Schematic diagram of negative tone (left) and positive tone (right) resist development.

2.6.2 Lithography

The lithographic process is a method used to create micro- or nano- structures by the formation of a pattern on a substrate via the proper resist coated on the substrate surface. Based on the types of lithographic energy sources employed, a lithographic technique can be termed UV, e-beam, X-rays or ion lithography. The first two are the most common lithographic techniques used in industry and research labs. In photolithography, a uniform layer of photoresist is applied to a surface to be patterned. Ultraviolet (UV) light is shown on a mask mounted above the surface. Some regions of the mask are transparent to the UV incident and allow exposure of the photoresist below while other regions are opaque and block the UV exposure.

The major advantage of photolithography is the capability of generating mass throughput. In other words, it is able to fabricate many devices with complex circuits at once in a short time. However, a fundamental restraint of photolithography is light diffraction, which limits the size of the patterned features that can only be fabricated to approximately the wavelength of the light source.

In electron beam lithography (EBL), electrons, instead of light, are radiated to the specimen. EBL does not require a physical mask to create designed patterns. This type of mask-free lithography is capable of writing patterns down to sub-10 nm [77] and has been widely used for low-volume production of semiconductor components and UV photomask fabrication [78].

The advantage of electron beam lithography is that it is one of the ways to break through the diffraction limit of UV photolithography and fabricate features in a nano-scale region. The major disadvantage of electron beam lithography is small throughput,

which means it takes a very long time to expose a large area of a substrate. A long exposure time leaves the user vulnerable to beam drift or instability that may occur during the exposure. In addition, proximity effect has to be considered while EBL is conducted. Proximity effect attributes to the fact that electrons undergo multiple inelastic and elastic scattering collisions once in the substrate. Some of energy is transmitted to the proximity of the desired area, leading to unwanted features generated after development. Proximity effect can be reduced by using higher acceleration voltages, applying smaller spot size or specific EBL settings [79].

2.6.3 Etching methods

Etching is a process used in micro- or nano- fabrication to physically or chemically remove specific layers, usually resists, from a substrate. In lithography, the etching process plays an important role in which part of the substrate is protected against the etchant by a masking material which resists etching whereas the unmasked part is etched thoroughly. Sometimes an etchant can etch two or more layers on one substrate at different etching rate depending on the material types in order to accomplish specific features. Etching methods can be categorized into two groups: wet etching and dry etching depending on etchant phases [80]. In wet etching, materials that are not protected by the mask are etched away by liquid chemicals. The wet etching method involves several chemical reactions and can be explained by three major mechanisms. First, the liquid etchant molecules diffuse to the layer that is prepared to be removed. Second, the reaction between the material being etched away and the liquid etchant undergoes and is accompanied by a further reduction-oxidation reaction. This is the reason that most of the liquid chemical etchants are acid or base solutions. Third, the byproducts from previous

reactions are generated and usually washed away. Wet etching is generally an isotropic process except for etching different crystalline structures. Low cost, good selectivity for most materials, easy conductions, and a high etching rate are the advantages of the wet etching method. Whereas sample contamination of byproducts and difficulty in defining small dimensions are the reasons that wet etching is not adapted.

In dry etching, the materials with a higher etching rate are etched away by plasmas or etchant gasses. The principle of the dry etching can be chemical, physical or a combination of both. [81] Theoretically, dry etching allows for etching with a higher aspect ratio and higher resolution than wet etching.

In chemical dry etching, instead of using liquid chemicals, etchants mostly are gases. The process involves a chemical reaction between the material being etched away and the etchant gases. Common ion gases used for chemical dry etching are chlorine gas (Cl_2), fluorine (F_2), sulfur hexafluoride (SF_6), and tetrafluoromethane (CH_4) [82]. In physical dry etching, high energy kinetic energy carriers such as ions or electrons are needed to bombard the substrate surface. There is no chemical reaction taking place during the bombardment process. As the high energy particles collide with the substrate atoms and make them from the substrate surface, the material evaporates and only the material that is able to resist the bombardment survives on the surface. The common physical etching processes include Ar ion milling and plasma sputtering. A method called reactive ion etching (RIE) is based on both physical and chemical principles to achieve the etching process. The process is one of the most diverse and most widely used processes in industry and research because it possess both physical and chemical etching advantages. The high energy carriers trigger the ionization of etchant molecules and accelerate the

etchant molecules to react with substrate material. Besides, since the substrate material is reacted chemically in the RIE process, the etching process has high selectivity [80].

2.7 Alumina as an Anti-corrosion Layer

Al_2O_3 is a good electrical insulator and also possesses a relatively high thermal conductivity (30 $Wm^{-1}K^{-1}$) [83]. Aluminum oxide is completely insoluble in water. There are several commonly occurring crystalline forms, γ-, δ-, η-, θ-, and χ-Al_2O_3. Aluminum oxide is used for the resistance of metallic aluminum oxidation and corrosion. Metallic aluminum is very reactive with atmospheric oxygen, but a thin Al_2O_3 layer is able to be a passivation layer on any exposed aluminum surface. This layer protects the other metal layers from further oxidation and corrosion. The related approaches for deposition and coating of a thin Al_2O_3 layer using the sputtering system has been studied and investigated [84]. These approaches can generate the high rate deposition of pinhole-free, and fully dense oxidized coatings. Al_2O_3 layer has been verified as a good corrosion protection layer on the GMR biosensor [85].

2.8 Landau–Lifshitz–Gilbert (LLG) Equation

The Landau-Liftshitz equation, used to solve time-dependent micro-magnetic problems, was first proposed by Landau and Lifshitz as follows [86]

$$\frac{\partial \mathrm{M}}{\partial \mathrm{t}} = -\gamma \mathrm{M} \times \mathrm{H}_{\mathrm{eff}} - \frac{\gamma\alpha}{\mathrm{M_s}} \mathrm{M} \times (\mathrm{M} \times \mathrm{H}_{\mathrm{eff}}). \qquad \text{(Eq. 2-2)}$$

The equation can be described along with a different approach proposed by Gilbert [87], which is referred to as the Landau-Lifshitz-Gilbert equation:

$$\frac{\partial \mathrm{M}}{\partial \mathrm{t}} = -\frac{\gamma}{1+\alpha^2} \mathrm{M} \times \mathrm{H}_{\mathrm{eff}} - \frac{\gamma\alpha}{(1+\alpha^2)\mathrm{M_s}} \mathrm{M} \times (\mathrm{M} \times \mathrm{H}_{\mathrm{eff}}), \qquad \text{(Eq. 2-3)}$$

where M is magnetization, t is the given time, γ is the electron gyro-magnetic ratio, M_s is

saturation magnetization, α is the Gilbert damping constant depending on the type of materials, and H_{eff} is a magnetic field comprised of the external magnetic field, the demagnetizing field, and quantum mechanical effects.

The Laudau–Lifshitz–Gilbert (LLG) equation is most commonly used to express the detailed interlayer magnetic switching status and compare the switching speed within magnetic thin films. Switching field dependence on the angle of the external field can also be calculated using the LLG equation. LLG is widely applied to calculate various perpendicular media and the component of a read head in a hard disk drive [88]. In addition to the practice of the LLG equation for calculating switching field and magnetic moment changing over time in magnetic thin films, the LLG equation is also used to analyze the magnetic behavior of a magnetic particle [89].

Chapter 3. Experimental Method

3.1 Preparation of GMR Multi-layer Stack

The AJA -2200 UHV magnetron sputtering system was used to fabricate multi-layer thin films. Employing an in-plane magnetic bias field underneath the targets can confine electrons, avoiding recombination of Ar ions and hence increasing deposition rates. The base vacuum was below 1×10^{-8} torr. During the operation, ultrapure Ar gas was injected into the main chamber and working pressure was approximately 2.5×10^{-3} torr with the condition of 100 Watt DC power.

The entire GMR spin-valve structure was deposited from bottom to top as Ta(2.5 nm)/Ru(5 nm)/Co(5 nm)/Ru(0.8 nm)/Co(10 nm)/Cu(4 nm)/Co(3 nm)/$Ni_{80}Fe_{20}$(10 nm)/Ta(5 nm). The deposition rate of each layer was calculated by sputter depositing each layer for six minutes and then dividing the thickness of each layer by six minutes. The deposition rates of Ta, $Ni_{80}Fe_{20}$, Co, Ru, and Cu were 0.1 nm/s, 0.06 nm/s, 0.1 nm/s, 0.07 nm/s, and 0.15 nm/s, respectively. A silicon dioxide wafer was first cleaned in a piranha solution followed by a 2.5 nm thick Ta layer deposition as an adhesive layer. The Ta layer reduces the roughness of the substrate, increasing the uniformity of further layer depositions. It was also deposited on the top of all samples as a capping layer because its oxidized state has intense density, protecting underneath metals from oxidation. A magnetic bias was applied on substrates during the deposition of magnetic layers in order to improve uniaxial anisotropy of ferromagnetic layer growth. When depositing the Co, permalloy, and SAF layers, substrates were fixed at a certain direction and were not allowed to rotate horizontally. The direction and angle were defined as shown in Figure

3.1. Consequently, uniaxial anisotropy was amplified. On the other hand, when depositing non-magnetic layers, substrates rotated horizontally in order to achieve flat and smooth layers. $Ni_{80}Fe_{20}$, also known as permalloy (Py) was the subsidiary layer coupled ferromagnetically to the adjacent Co free layer. The low coercivity of the subsidiary layer in an external magnetic field is able to induce the reversion of the magnetization in an adjacent Co layer, reducing the coercivity so that the orientation of the free layer could flip more easily. Cu was an ideal material for the spacer layer because of its nonmagnetic, high interfacial spin-dependent scattering and high conductivity properties. Ru, with its strong antiferromagnetic coupling effect, was an ideal interlayer for synthetic pinned layers. 5 nm thick Ru was also employed under the bottom Co layer to improve the Co crystal-lattice alignment.

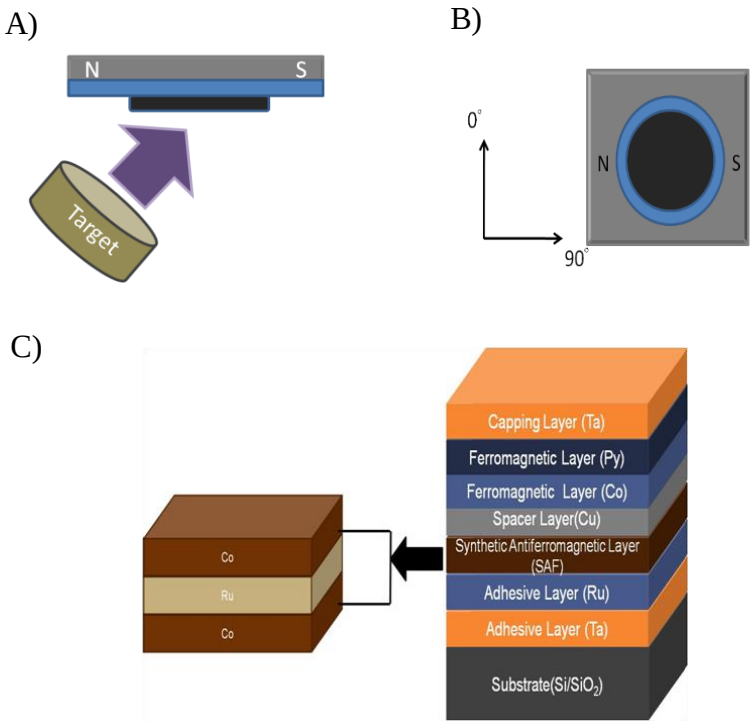

Figure 3.1: A) The illustration of target metal deposition with bias field applied on sample holder. B) The easy axis of GMR spin-valve multi-layer was assigned along 0°. C) The component of GMR spin-valve multi-layer.

3.2 Chip Design

The illustration of sensors and corresponding contacts is shown in Figure 3.2. The sensor was 400 nm × 400 nm, connected by two 60 μm long Cu contacts at both ends. A second set of Cu contacts with 50 μm linewidth was designed to attach and overlay at both ends of the first set of Cu contacts, separated by a 50 μm wide space, as shown in Figure 3.2 B). A 2 mm×4 mm Cu pad was designed and fabricated for 4-point probes measurement device. The extension from the pad was 500 μm in width as shown in Figure 3.2 C). Figure 3.3 illustrates the whole design of the 12 sensors with corresponding circuits on a chip.

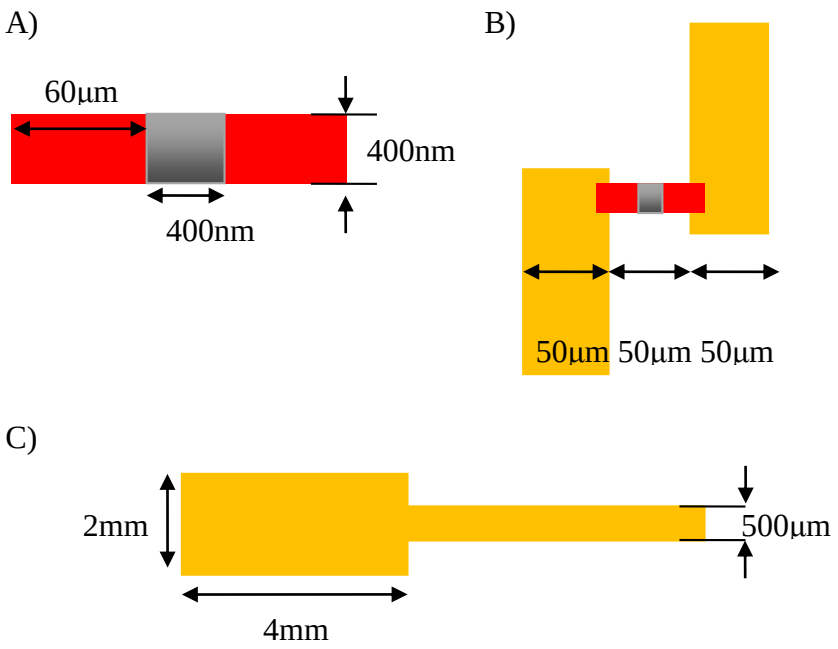

Figure 3.2: The dimension of the sensor and its paired contacts: A) sensor (gray area) with its first set contacts (red area), B) second set contacts, C) lead end and contact pads.

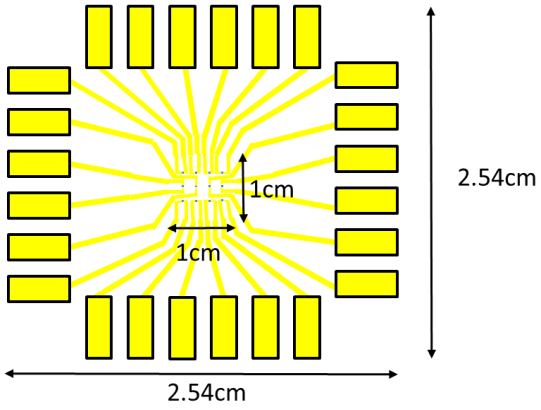

Figure 3.3: The schematic illustration of a GMR sensor chip.

3.3 Sensor Fabrication

Nano-scale magnetic sensors were fabricated on a GMR multi-layer stack using a combination of optical and e-beam lithography (EBL). Wet and dry etching were also involved. The overall process is illustrated in Figure 3.4.

3.3.1 Fabrication processes of self-aligned contact surface

PMGI (from MicroChem) was first spin-coated onto GMR layers at 3400 rpm for one minute and baked at 180 ℃ for 90 seconds. PHOST (from Aldrich-Sigma) was found to be delaminated easily on a raw PMGI surface; therefore a one minute UV-Ozone treatment was conducted after the PMGI was spin-coated in order to reduce hydrophobicity and further enhance PHOST adhesion. PHOST was then spin-coated, at 1000 rpm for one minute, onto a UV-Ozone modified PMGI surface and baked at 130℃ for 60 seconds.

To investigate required exposure doses, the contrast curve of PHOST/PMGI with 100 nm, 200 nm and 400 nm linewidth, respectively, was built with various bilayer thicknesses at an e-beam working dose ranging from 100 to 13500 μC/cm^2. The thickness

of PHOST/PMGI was determined by the profilometer. In our experiment, e-beam lithography was performed using JEOL JBX-5500FS to write four 1 μm×400 nm line patterns on the PHOST resist. 8500 μC/cm^2 was applied on the bi-layer to form a cross-link PHOST structure. The bi-layer was then developed in propylene glycol monomethyl ether acetate (PGMEA) (from Aldrich-Sigma) for 30 seconds, followed by a 0.88% tetramethyl ammonium hydroxide (TMAH) (from Shipley MF-319) treatment on samples for 50 seconds to etch through the PMGI layer and generate an undercut configuration.

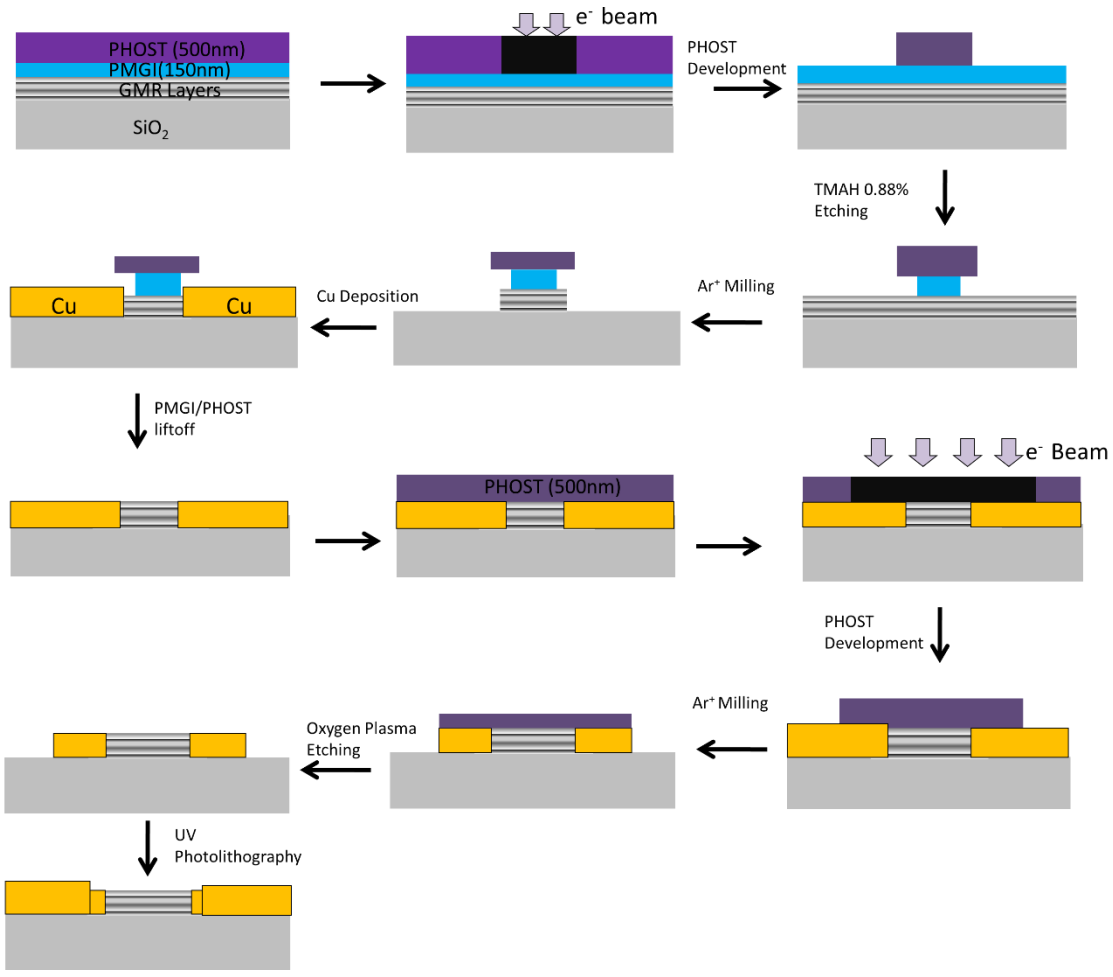

Figure 3.4: Sensor fabrication processes using combination of electron-beam and UV optical lithography.

The undercut configuration was formed for the lift-off process and also for generating an opening at both lateral ends of the line patterns. A further Cu layer could be deposited and partially overlapped with the GMR multi-layer stack in those openings. The average 110 nm undercut length was precisely controlled by the PMGI etch time. Afterwards, samples were ion milled in Ar gas at 500V, 34mA for 80 seconds to remove unmasked GMR layers. After Ar ion milling, samples were loaded into a UHV sputtering system to deposit the Cu layer with an optimized thickness of 70 nm. The lift-off process was then conducted. Samples were immersed in 3% TMAH solution for 5 to 10 minutes, followed by a five minute ultrasonic agitation after which GMR line patterns and the Cu layer were successfully transferred to the substrate.

3.3.2 Fabrication of first set of sensor contact wires

In order to define 120 μm × 400 nm Cu contact wires, an EBL including alignment process was conducted. PHOST was spin-coated on the substrate. The substrate was then aligned vertically to overlay with the previous line patterns in the center, generating a cross configuration by e-beam at a dose of 8500 $\mu C/cm^2$, 50kV. The patterns were developed using a PGMEA solution, follow by Ar ion milling for 180 seconds at 500V, 34 mA to wipe out unmasked metal layers. The PHOST was then removed using oxygen plasma etching with the given etching condition of 150 W, 50 sccm oxygen flow rate and under 40 mtorr operating pressure for three minutes. The reason for using oxygen plasma etching to remove PHOST is based on its high selectivity of PHOST etching over GMR and Cu layers. Thus, the damage to GMR layers underneath PHOST could be minimized.

3.3.3 Fabrication of second sets of contact wires and pads

The second set of copper contact wires and pads were patterned using the UV

photolithography technique. PMGI was first spin-coated onto the substrate and baked at 180 ℃ for 90 seconds, followed by the spin-coat of AZ-1512 photoresist and baked at 90 ℃ for 90 seconds. Twelve pairs of contacts were aligned and printed through the ABM 365 nm UV mask aligner after which samples were conducted post-baked at 120℃ for 90 seconds. Since TMAH can be used as both AZ-1512 developer and PMGI etchant, the development and etching processes were performed together by immersing the substrate in 3% TMAH solution for 30 seconds. A 500 nm thick Cu layer was then sputter deposited on the substrate. For the lift-off process, the substrate was immersed in 3% TMAH for 30 seconds and then in acetone for five minutes with ultrasonic agitation. As a result, a completed GMR chip comprised of twelve sensors, their pair contacts, and pads was fabricated.

3.4 Instruments and Metrology

3.4.1 Scanning electron microscope (SEM)

The scanning electron microscope (SEM) uses high-energy electrons to generate a variety of signals at the surface of solid and conductive specimens. The signals derived from electron-sample interactions provide information on the specimen including surface morphology, chemical composition, and crystalline structure and orientation of materials. In most applications, signals are collected over a selected area of the specimen surface, and a 3-dimensional image is generated which displays spatial variations in these properties. The principle of how the SEM works is illustrated as follows:

The electron is emitted from an electric field generated by a tungsten tip in the electron gun. The image brightness, the ß value, is an important parameter depending on the electron gun. The value of ß is a function of the operating temperature, filament type, and

operating voltage. Electromagnetic lenses are used here to adjust focus. The focal length depends on two factors: the quantity of the current through the coil which determines the flux density, B, and the gun voltage which determines the electron velocity, v. Therefore, the operator controls the focal lengths of the lenses by adjusting the currents applied to them. Increasing the radial force by increasing the current reduces the focal length. The scanning electron microscope allows the electron beam to scan the sample surface. There are two sets of scan coils in which one is for raster and the other is for deflection. The emission of the beam is deflected by the Lorentz force derived from the magnetic fields of such pair coils in a double-deflection system. These coils cause the beam to scan over a square area on the specimen surface. The scan generator controls line times and the frame as well as the raster size. Higher magnification can be obtained by reducing the raster size over the specimen. As electrons interact with the surface material, several signals would be generated from the specimen. These signals generally can be in forms of backscattered electrons (BSE), secondary electrons (SE), diffracted backscattered electrons, heat, and photons (X-Ray). Secondary electrons and backscattered electrons are two most commonly used for imaging samples. Secondary electrons are most suitable for showing morphology and topography on samples. On the other hand, backscattered electrons are most capable of illustrating contrasts in composition in multiphase samples. Since SEM analysis is considered to be non-destructive except for those electron-sensitive materials such as e-beam resists, it is possible to analyze the same specimen repeatedly.

FEI XL-30FEG SEM was used for inspecting the nano-scale surface in this research. The geometry of the sensor was examined and verified through scanning electric

microscopy (SEM). The high-resolution field-emission SEM has an optimum morphology and pattern image resolution using secondary electrons, and is controlled completely by a computer terminal. The microscope can be operated both at low accelerating voltage (5kV) and high accelerating voltage (30kV), depending on the thickness and conductivity of the surface material of the specimen. The ultra-high resolution (UHR) mode is able to improve the resolution to 20 nm.

3.4.2 Focused ion beam

The focused ion beam (FIB) system uses a Ga^+ ion beam to raster over the specimen surface similar to the way the electron beam does in SEM. Images of the surface of the sample result from the generated secondary electrons (or ions). The focused ion beam is also capable of generating the milling of many kinds of nano-scale geometry patterns on the sample at well-designated locations. Therefore, cross-sectional images of the specimen structure can be obtained or 3-dimensional local modifications in the structures can be fabricated.

FEI 235 dual-beam focused ion beam is used in this research, primarily for cross-sectional inspection of undercut configuration on PMGI. This FIB system is controlled by a Windows NT terminal. Gallium liquid metal is used for the focused ion beam operated at 5 to 30 kV in a current range of 30 pA to 500 pA. The sample stage has to be tilted at a 52°-tilt angle to make the ion beam perpendicular to the specimen for further cross-sectional milling. 3D imaging of the cross section cut by the ion beam can be carried out by using equipped SEM at 15kV. This FIB system is able to reach as high as 3 nm spatial resolution.

3.4.3 Profilometer

Profilometer is a thickness measuring apparatus used to determine the surface's profile. A 12.5 μm stylus is vertically in contact with the substrate and can scan horizontally across the substrate for a 400 nm to 1000 nm distance. The height position of the stylus generates a vibrating signal which is then converted into a digital signal output. The horizontal resolution is controlled by the data signal sampling rate and the scanning speed.

In our work a Tencor alpha-step 200 profilometer was used to measure the thickness of metal and polymer layers. The thickness measurements further determined spin-coated rates, multi-layers deposition rates, and etch rates.

3.4.4 Electron beam writer

An e-beam writer is an important tool particularly in micro-electronics, which require extremely precise placement of nano-scale circuit elements. Basically, an e-beam writer is operated to emit a concentrated beam of electrons precisely onto a designated resist coated substrate. High energy electrons can induce either the deposition of substances onto a surface, or etch away at the surface. One using an e-beam writer is capable of designing and writing elements on a smaller scale than using photolithography tools. However, components can only be fabricated very slowly, largely increasing the cost and time. In addition, an e-beam writer is necessary to be operated in a vacuum environment, further tightening the required process and equipment. Therefore, it is only suitable for a small amount of production.

JEOL JBX 5500FS, as shown in Figure 3.5, is primarily used to write the sensor patterns and the first set of contact wires in our sensor fabrication processes. The amount of the exposure dose is primarily determined by the types of e-beam resists, pattern

dimensions, and the limit of proximity effect. Optimum calibration, mask design, and exposure setup are conducted using an embedded program before pattern writing. The writing process was carried out at 50 kV, 10 nA in a high vacuum environment below 10^{-4} Pa.

Figure 3.5: JEOL JBX-5500 electron beam writer.

3.4.5 Reactive ion etching (RIE)

The RIE system is basically comprised of a cylindrical vacuum chamber, with a non-conductive sample platter positioned at the bottom of the chamber. The sample platter is electrically isolated for generating a high voltage difference as the RIE occurs. Etching gas is injected through small inlets in the top of the chamber, and exits from the vacuum pump system through the bottom. The flow rate of the etching gas is precisely controlled.

Types and amount of gas used vary depending on the substrate type and etching process. Gas pressure typically remains in a range between a few mtorr and a few hundred mtorr by adjusting gas flow rates and the degree of the valve opening of the exhaust. Since RIE systems can be easily fitted in a low cost laboratory development, it has been widely used in organic electronics research or semiconductor industry.

Oxford Instruments Plasmalab 80 Plus has been performed for the reaction ion etching process in this study. In the reactive ion etching process, oxygen was used as etching gas here because of its very high selectivity between PHOST and the Cu underlayer. The 500 nm thick PHOST can be etched thoroughly using O_2 RIE with the given conditions of 150W, 200V DC bias, 50 sccm oxygen flow rate and under 40 mtorr operating pressure for three minutes.

3.4.6 Argon ion milling

Unlike oxygen RIE based on chemical etching, Ar ion milling is a physical milling process in which Ar ions bombard the specimen surface, causing atoms from the specimen to eject from the surface. Ar ion milling is a non-selective anisotropy process. The milling rate depends on the types of milled materials.

A Veeco customized Ar ion milling system has been used in this experiment to mill thoroughly unmasked metal layers. Samples were ion milled in Ar gas at 500V, 34mA under working pressure 10^{-4} torr. The advantage of using such high energy Ar ion milling system is that it takes less time than using the RIE system to mill a large area of specimen.

3.4.7 UV mask aligner

A UV mask aligner is an exposure systems typically producing an image on the wafer

using a photomask. The UV light sifts through the photomask, which prevents the light from reaching some regions but allows the light to pass on some other regions on a wafer at the same time.

The ABM mask aligner, as shown in Figure 3.6, has been used in this research to define and fabricate the electric circuit which consists of the second set of electric wires and corresponding pads for the sensor arrays. The UV lamp is able to generate a 365 nm wavelength at the intensity of 20mW/cm^2. The chromium-on- glass photomask was designed and used in direct contact with the substrate and exposed it to a uniform UV light. A microscope equipped on the system can help one to conduct the alignment and overlay process. It took four seconds to expose a 0.5μm thick AZ-1512, a positive-tone photoresist, under the condition of 20 mW/cm^2 light intensity at room temperature.

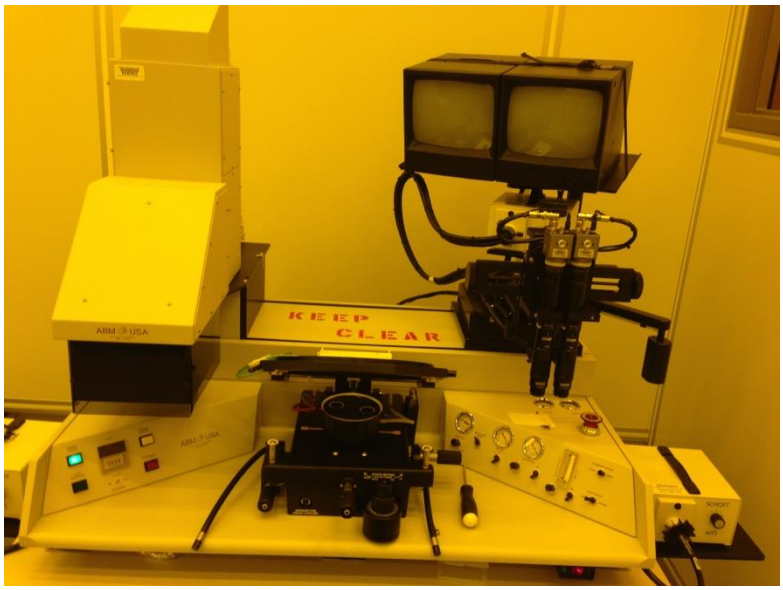

Figure 3.6: ABM mask alignment system.

3.4.8 Vibrating sample magnetometer (VSM)

A VSM instrument is the most commonly used magnetometer for the characterization

of magnetic materials. The critical sensitivity can reach up to 10^{-6} emu, and the field resolution can be as small as 10^{-3} Oe. VSM is widely used to obtain magnetic properties including magnetic moment, Hc, Ms, and hysteresis loop. The principle of a VSM is based on Faraday's law of induction,

$$V(t) = C\frac{d\Phi}{dt}, \qquad \text{(Eq. 3-1)}$$

where $\frac{d\Phi}{dt}$ stands for the change of magnetic flux over time, C is the proportionality constant, and V(t) is the induction voltage. The schematic structure of a VSM instrument is shown in Figure 3.7. In a VSM measurement a sample, usually smaller than $1cm^2$ placed in the optimum position, is vibrated perpendicularly to the applied field in the vicinity of a set of pick-up coils. The magnetic flux change caused by the vibrating magnetic sample generates an induction voltage across pick-up coils that is proportional to the magnetization of the sample. A known magnetic sample, usually Ni, is required to be measured for the calibration process prior to the measurement of an unknown magnetic sample. The output voltage from the pick-up coils is the signal of the magnetic moment of the sample, and the detection signal from the embedded Hall probe is the strength and orientation of the magnetic field.

A VSM instrument is particularly useful for measuring GMR, tunneling magnetoresistive (TMR) films, AF system, and spin-valve. In addition to the GMR thin films, magnetic characterizations of several types of magnetic particles were measured by VSM in this research. The measuring processes of magnetic particles are similar to the measuring processes of GMR thin films. However, the major difference is that the standard sample used for the calibration of magnetic nanoparticles is a spherical Co sample instead of the square Co thin film used for the calibration of GMR thin films. In

this project, the magnetic moment as a function of switching external fields on different components and orientations of GMR layers was measured by VSM. Full hysteresis loops were obtained for investigating the magnetic behavior of GMR layers and magnetic nanoparticles.

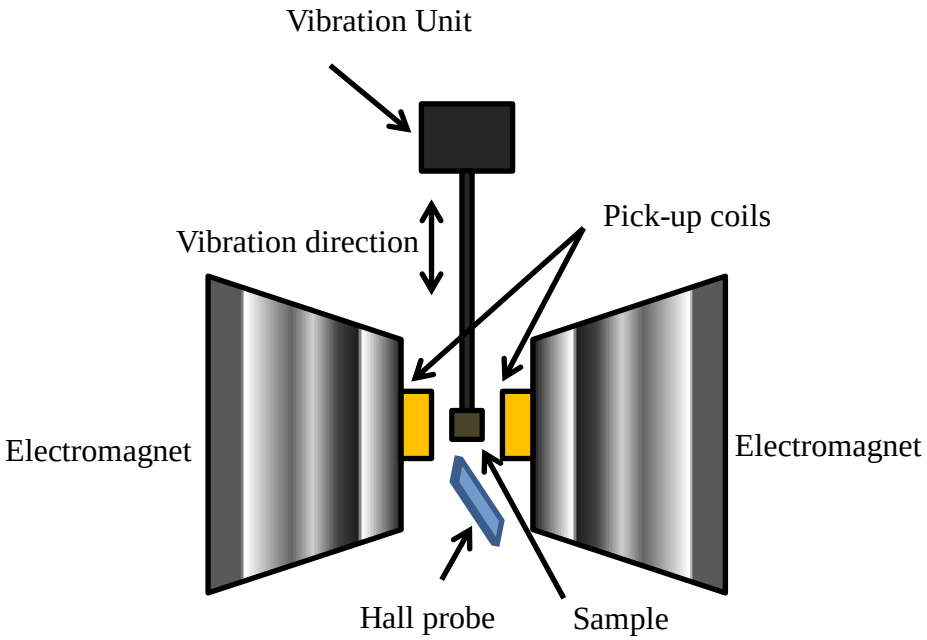

Figure 3.7: The schematic diagram of a VSM.

3.4.9 4-point probes measurement

A 4-point probes instrument is broadly used for the non-destructive measurement of sheet resistance or magnetoresistance. A set of four probes is usually aligned linearly and landed on a flat conductive surface with a fixed separation distances. A constant current source is applied through the two outermost probes, and the potential change of the sample is measured through the inner pair of probes. The advantage of using 4-point probes over 2-point probes is that the 4-point probes measurement excludes the influence

of resistance from those connecting wires.

In order to measure the GMR effect of our sensor, the 4-point probes system was designed as shown in Figure 3.8. In this system, a power supply drove the electromagnet to produce the magnetic field which was measured by the Hall probe. A Lakeshore model 450 gauss meter could convert the Hall probe signal to digital output. The current sensing and voltage signals were obtained by the Keithley sourcemeter and converted to digital output through a data acquisition (DAQ) card manufactured by National Instruments. The whole process of resistance measurement under varying external fields was controlled by Labview ® in a computer terminal.

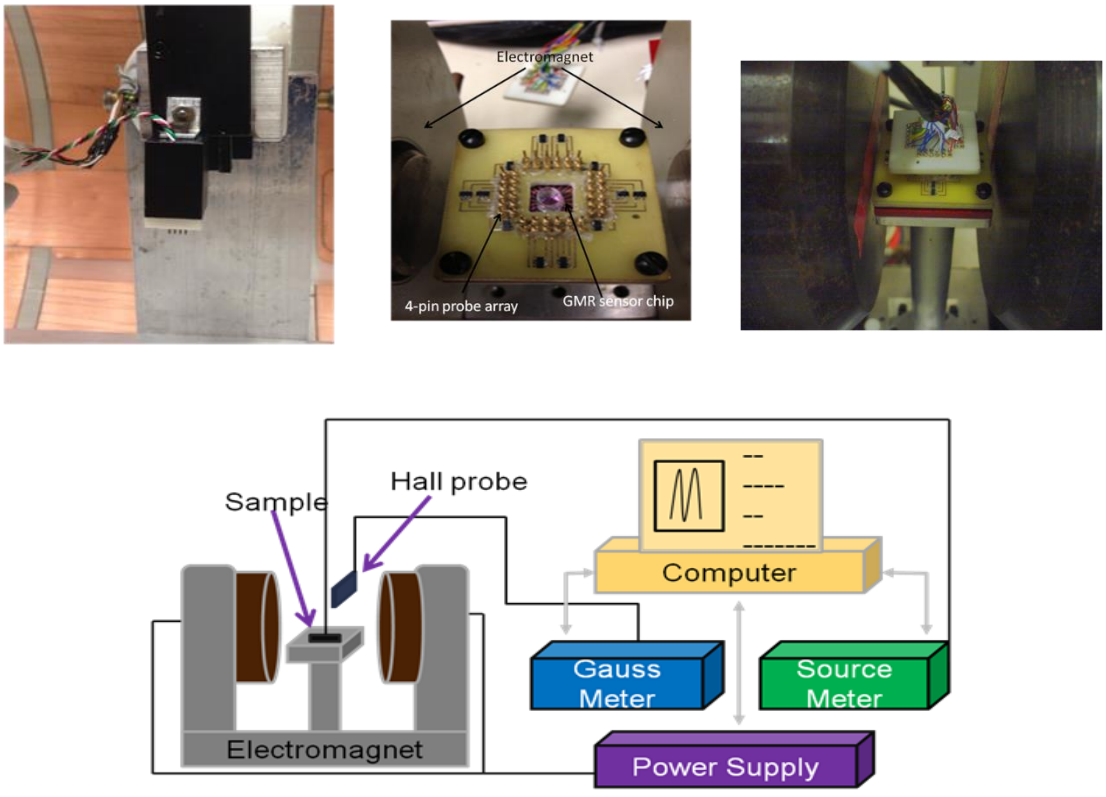

Figure 3.8: The schematic illustration of 4-point probes setup for GMR measurement.

The 4-point probes measurement was used to measure both sheet samples and biosensor array chips in this research. For sheet sample measurements, the sheet sample was placed in the middle of the electromagnet and a sensing head manufactured by Cascade Microtech with a set of four parallel probes was applied and perpendicularly landed on the sheet sample surface. Each probe was separated at fixed 1.55mm distance with one another. A bipolar power supply generated cyclical voltage to the electromagnet from 10V to -10V and back again, which triggered the magnetic field ramped up to 800 Oe at the beginning, then ramped down within several steps to -800 Oe, and finally back again to 800 Oe to complete the loop. The power change frequency was optimized to 0.1 Hz and the sensing current was 0.2 mA. For measurements of biosensor array chips, a 5 cm $\times$ 5 cm customized sample holder was designed to load the chip. An acrylic board mounted with 48 spring-loaded pins was fabricated and screwed tightly to the sample holder in order to connect the copper wires and sensor chip. The pins were aligned as 24 pairs and landed on 24 contact pads on the chip correspondingly, as shown in Figure 3.8. The sample was then placed in the middle of the electromagnet and capped by a lid on which twelve channels of 4-point probes were installed. A Keithley switch system was installed for facilitating measurements for twelve sensors on a chip at once. For the sensor-particle resistance measurement, a plastic, corrosion-free tube with two openings at the top and bottom ends was glued on the chip by vacuum gel. For dry magnetic particle detection, the 50 nm Fe_3O_4 nanoparticles were directly dropped on the sensor surface with an external field of zero. GMR measurements were conducted before and after particles dropped. Another method of the particle distribution was conducted. Magnetic particles first stored in ethanol solution were dropped from the top of the chip

to sensing areas before the lid was capped. The volume of the particle solution dropped on the sensing areas was from 40μl to 100μl depending on the particle concentration in order to make sure that there was appropriate probability that nanoparticles were attaching onto the sensing area. However, at the same time, there was relatively low probability for the formation of particles aggregation. GMR measurements had been carried out every 60 to 100 seconds for at least 18 hours.

3.5 Corrosion Test

An ultra-high vacuum sputtering system was used to deposit amorphous alumina on top of the sensor as the anti-corrosion layer. The processes and conditions for depositing approximately 30 nm thick alumina were presented as follows: 4 nm thick aluminum metal was first sputtered at 100 Watt DC power for 5 seconds as a seed layer after which the oxidation process was warmed up by introducing a 30 Watt DC bias on the substrate for 30 seconds and then performing aluminum oxidation with a 15 Watt bias plasma for 35 seconds. During the alumina deposition process, aluminum was sputtered with 100 Watt DC power at 45 degree angle to the substrate surface with the presence of a mixture of gas comprised of Ar with a 35 sccm flow rate and O_2 with a 6 sccm flow rate. The deposition rate of alumina was averaged 0.8 Å /s. In order to avoid unnecessary alumina coverage, the sensor chip was fully covered by aluminum foil, but a 1 cm × 1 cm area was left hollow in the sensor chip center before the alumina deposition process was carried out, as shown in Figure 3.9.

The valid protection ability of the alumina anti-corrosion layer against a PBS solution with different concentrations was tested. 0.1M and 0.01M PBS solutions were prepared by mixing PBS powder bought from Sigma (P5368) with 100 ml and 1000 ml DI water,

respectively. All PBS solutions were maintained at pH 7.4.

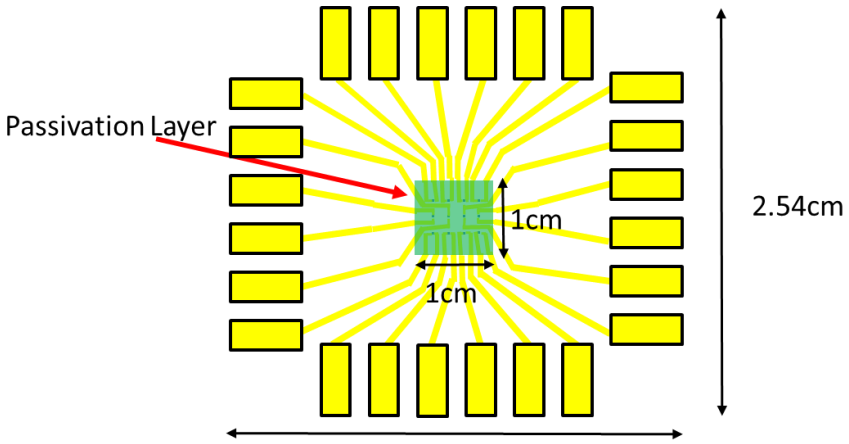

Figure 3.9: The schematic diagram of sensor arrays protected by Al_2O_3 passivation layer.

3.6 LLG Simulation Method

The software used for the GMR sensor and magnetic particle simulation is LLG Micromagnetics Simulator™ [90]. It is 3-D simulation package software with integrated graphics based on numerical methods used to solve Landau-Lifshitz-Gilbert-Langevin equations, as shown in Figure 3.10. By using this program, micromagnetic structure and dynamic behavior in thin films, magnetic devices or materials can be simulated and characterized.

For characterizing micromagnetic behaviors of the GMR sensor, simulations were conducted in a 400 nm × 400 nm × 30 nm cubic with 30 × 30 × 50 discrete points. From bottom to top, Co (12 nm)/Cu (6 nm)/Co (3 nm)/Py (9 nm) layers were constructed. Standard parameters were used to characterize the properties of Co, Cu, and Py are as follows.

- Co: Resistivity= 4.8 μΩ-cm, M_s= 1400 emu/cc, and uniaxial anisotropy constant K_u=

4×10^6 erg/cc.

- Permalloy: Resistivity =5.6 μΩ-cm, M_s=800 emu/cc, and K_u=1000 erg/cc.
- Cu: Resistivity=2 μΩ-cm, K_u=0, and M_s=0.

Exchange stiffness is 3.05 μerg/cm for Co and 2.1 μerg/cm for permalloy. In addition, 0.2 mA time-independent current was applied along the x-axis direction, which is the same direction as the easy axis of the cobalt layer, and permalloy. Various strengths of the external field were also applied along ±x-direction.

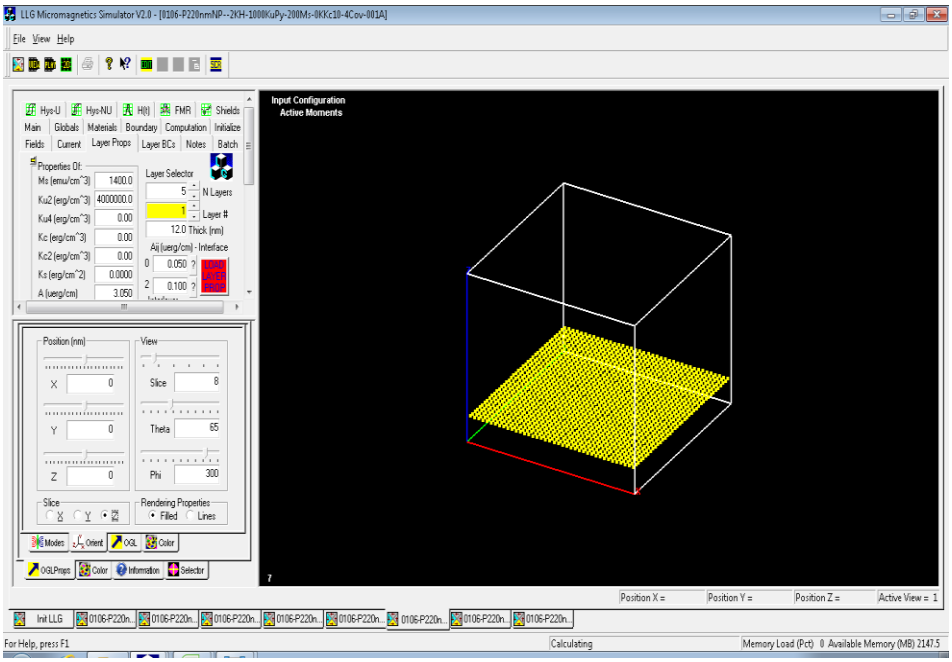

Figure 3.10: The magnetic simulation environment of LLG Micromagnetics Simulator™.

Furthermore, to study intra magnetism of a single magnetic particle and further interaction between a single particle and a GMR sensor, two different sizes, 100 nm and 200 nm Fe_3O_4 nanoparticles were also built. Each particle was built in a 400 nm × 400 nm × 300 nm cubic with 30 × 30× 50 discrete points. For 100 nm and 200 nm particle models, Fe_3O_4 particle parameters were assigned as K_c= 2×10^5 erg/cc, M_s= 280 emu/cc,

exchange stiffness, A= 0.005 μerg/cm, and resistivity= 6100 μΩ-cm. The anisotropy axes of particles in the cubic lattice were set along [100] and [010]. External field parameters were assigned as switching in between 800 Oe and -800 Oe at pitch 25 Oe. Time integration is computed using the rotation matrices approach with 0.1 ps time steps. All the calculation were set to be completed when the convergence was as small as 10^{-4}.

Chapter 4. Results

4.1 Optimization of GMR Multi-layer Thin Films

4.1.1 Sputter deposition rate and thin film uniformity

The DC magnetron sputter deposition rate of each metal layer was investigated in advance of depositing specific thicknesses of each layer in the GMR multi-layer stack. In addition, since the chamber pressure and DC power were fixed at 2.5 mtorr and 100W, respectively, the uniformity of deposited layers on a three-inch wafer was varied depending on the distance between the sputter target and the area on the wafer.

For investigating the uniformity of each metal layer deposition, a wafer map separated into 24 divisions for each metal layer was constructed. Each wafer map demonstrated the deposition rate of each metal layer, as shown in Figure 4.1. Generally, the average deposition rate of copper is the highest among the five metals, whereas the deposition rate of Py is the lowest. Besides, no matter what kind of metal the layer was, the deposition rate of the center divisions within the radius of one-inch demonstrated good uniformity. Since the center divisions were also large enough for fabricating sensor arrays, a multi-layer stack was prepared and deposited in this range of the area at the deposition rate of 1 Å/s, 1.7 Å/s, 0.75 Å/s, 1.05 Å/s, and 1 Å/s for Co, Cu, Py, Ru, and Ta, respectively.

4.1.2 Magnetic characterization of essential magnetic layers

In order to achieve a high GMR ratio, the consistency of anisotropic directions of the permalloy layer was investigated. In Figure 4.2, a 50 nm thick permalloy was measured using VSM. The external field was applied between 20 to -20 Oe, along the sample in-

plane direction. The sample was rotated horizontally and measured from 90° to -90° at 5° intervals.

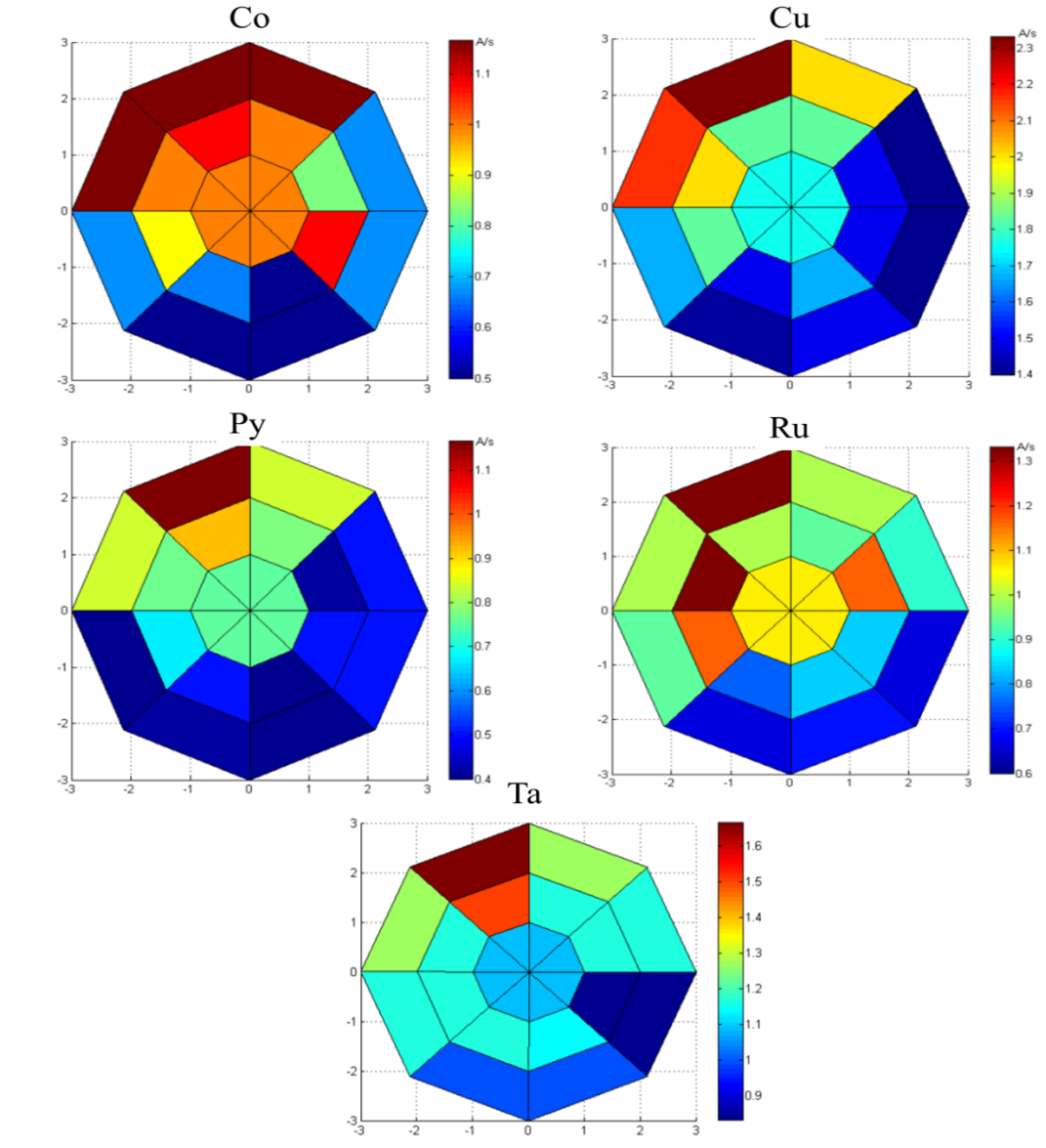

Figure 4.1: The illustration of deposition rates distributed on a 3" wafer for Co, Cu, Py, Ru, and Ta using DC magnetron sputtering system at 2.5 mtorr, and 100W operating conditions.

The magnetization curves of Py dropped smoothly as the external field was applied in

the range between 5 Oe and -5 Oe, indicating that the magnetic domains in the layer were randomly aligned. That is, no specific easy axis orientation was observed for the whole Py layer. Ideally, for a high GMR ratio, magnetic domains in the Py layer are designed to show uniaxial anisotropy along one particular direction.

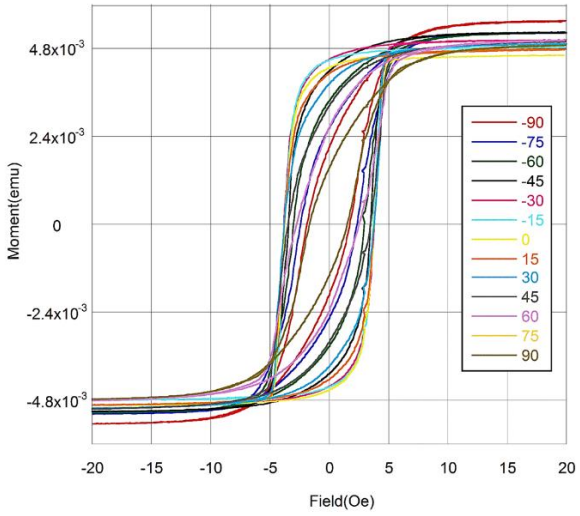

Figure 4.2: The hysteresis loops of a 50 nm thick permalloy layer at various angles without magnetic bias applied.

To improve uniaxial anisotropy, an approximately 40 Oe magnetic bias was applied to the sample as sputtering deposition was conducted. Figure 4.3 illustrates the hysteresis loops of a 50 nm thick permalloy layer, measured at various measurement angles, with a 40 Oe magnetic bias applied during the sputtering deposition. Significant differences in the hysteresis loop at various measurement angles were observed. The magnetization curve was formed to a high squareness ratio loop when the measurement angle was either 90° or -90°. The magnetization changed sharply as the external field was approaching 5 Oe and -5 Oe. In addition, the coercivity was approximately 2 Oe, which was lower than 5 Oe, the coercivity of the same thickness permalloy layer without magnetic bias applied

during the sputtering deposition. Those evidences imply that the magnetic domains in the permalloy layer were aligned consistently and easy axes of every magnetic domains were nearly isotropic.

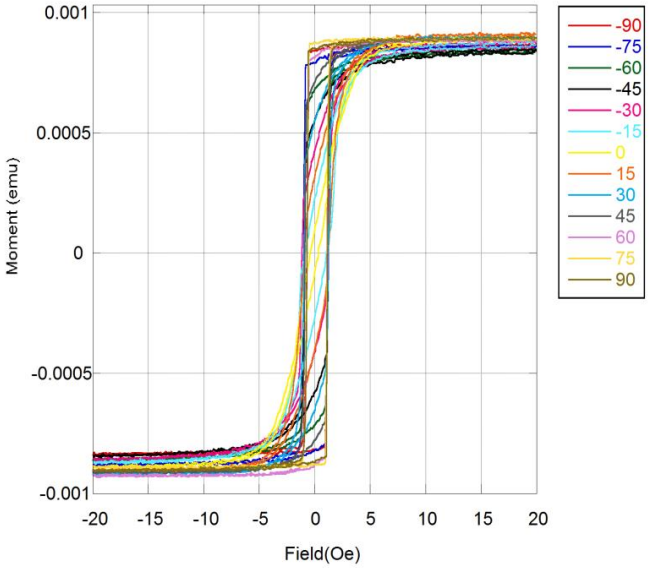

Figure 4.3: The hysteresis loops of a 50 nm thick permalloy layer at various angles with 40 Oe magnetic bias field applied.

Next, the magnetization of a 10 nm thick Co layer deposited above the Ta seed layer was investigated. The in-plane magnetization of the Co layer was measured and rotated horizontally every 15° within 180° in order to obtain the orientation of the easy axis, as shown in Figure 4.4 A). As the external field applied on the sample was aligned parallel to the sample's easy axis orientation, the highest coercivity and squareness ratio close to one was observed when the angle was ±90°, as shown in Figure 4.4 B). For the spin-valve based biosensor, the coecivity of the free layer is prefered to be below 20 Oe so that the stray field generated by the moment from the magnetic nanoparticle will be able to exhibit significant influence on the GMR profile of the sensor. By considering this

situation, permalloy is a good candiate for a free layer. On the other hand, by taking into account the mixed influence from demagnetizing, nonlocal interlayer bilinear exchange coupling, and anisotropy, a Co/Cu/Co tri-layer is a good spin-valve device. Therefore, a permalloy layer ferromagnetically exchange coupled with a thin Co layer to form a Co/Py bi-layer as the spin-valve free layer was preferred in our sensor fabrication process and suitable for our sensor application.

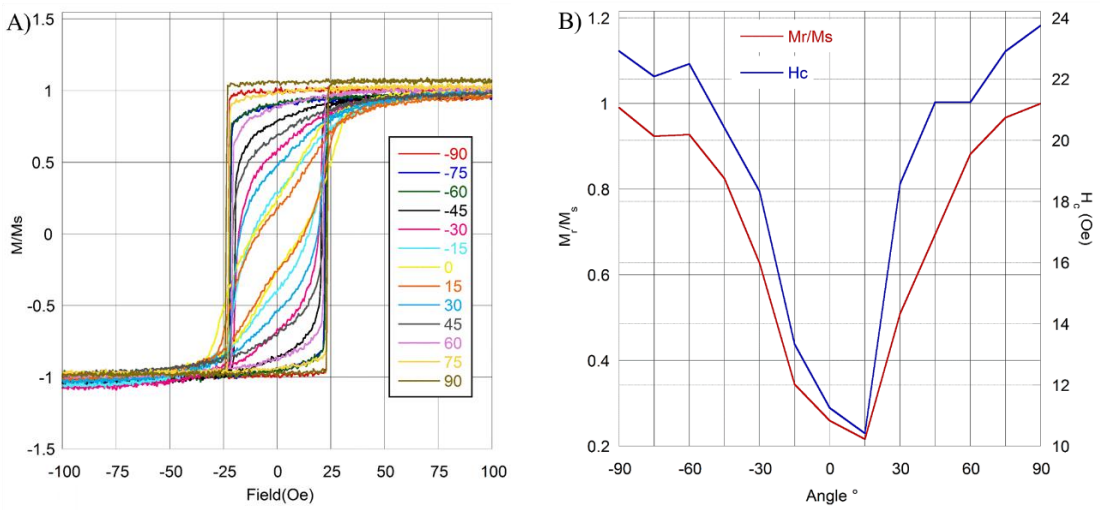

Figure 4.4: A) The hysteresis loops of a 10 nm thick cobalt layer measured at various angles. B) The coercivity and squareness ratio corresponding to different measured angles.

The magnetization of the Co/Py bi-layer was verified. In Figure 4.5, there are not any multi-steps in the hysteresis loop of the Co(3 nm)/Py(10 nm) layers, indicating that the perfect ferromagnetically exchange coupled within the bi-layer at a measured angle of 90° is observed. In addition, when the external field was applied parallel to the easy axis of the Co/Py bi-layer at ±90°, the perfect squareness loop was presented. The coercivity of the Co/Py bilayer is approximately 5 Oe, which is in between the magnitude of the

coercivity in permalloy and the cobalt individual layer.

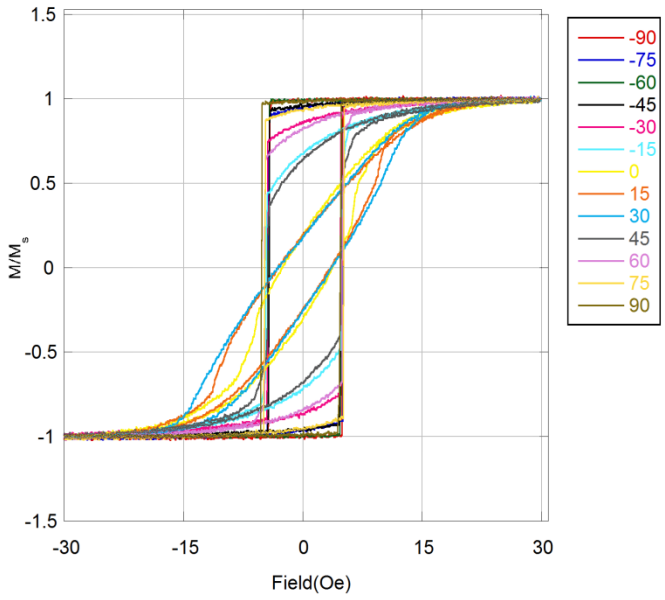

Figure 4.5: The hysteresis loops of a Co(3 nm)/Py(10 nm) bi-layer measured at various angles. At ±90°, the external field was parallel to the easy axis of the bi-layer.

For a spin-valve component, the effect of the thickness of the spacer layer deposited between two magnetic layers is critical on a GMR result. If the thickness of the spacer layer is too thin, the unpaired carrier electrons in one magnetic layer may exchange coupled with other electrons in the other magnetic layer and induce their spin alignment along same direction. Thus, the difference of the coercivity between two magnetic layers may be reduced, leading to low GMR. On the other hand, if the spacer layer is too thick, GMR may decrease due to the large current shunting in the spacer layer, also leading to low GMR. The Cu layer was used as a spacer layer in our spin-valve device. The hysteresis loop of the spin-valve multi-layer thin films, Ta(5 nm)/Co(10 nm)/Cu(x nm)/Co(3 nm)/Py(10 nm), depending on Cu thickness is shown in Figure 4.6. The Cu

thickness x was varied in order to seek the largest coercivity difference between two seperated ferromagnatic layers. Since the Cu layer was thick enough, the coercivity of the Co layer on top was reduced by its adjacent permalloy layer but the coercivity of the Co layer at the bottom remained the same due to no significant magnetic effect from the permalloy layer. Such a coercivity difference between the two Co layers attributes to electron spins in the two Co layers switching at different fields. Therefore, a sub-step in the magnetization curve might be exhibited. In our result, as the Cu layer was 4 nm thick, the largest coercivity difference was observed, implying that the top Co/Py bi-layer and thebottom Co layer aligned in an anti-parallel direction within ±10 Oe and ±20 Oe.

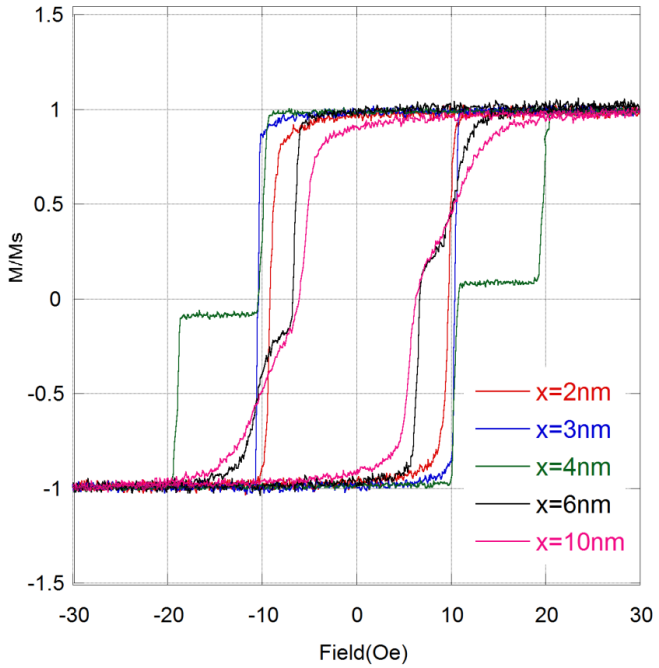

Figure 4.6: The hysteresis loop of Ta(5 nm)/Co(10 nm)/Cu(x nm)/Co(3 nm)/Py(10 nm). A significant sub-step in the loop is presented as the thickness of Cu, x is 4nm.

With the thickness of Cu layers either thinner or thicker than 4 nm, there is not clearly

a sub-step loop in these magnetization curves, implying that anti-parallel alignment did not obviously appear. When the thickness of the Cu layer decreases to 2 nm, it was not thick enough to divide the two Co layers. Therefore, ferromagnetic exchange coupling occuring between the two Co layers generated a complete square loop with all electron spins switching concurrently. As a result, no sub-step loop in the magnetization curve is presented.

In order to enhance the GMR effect, a tri-layer, Co/Ru/Co, was prepared as a synthetic antiferomagnetic pinned layer employed at the bottom of our spin-valve system. By designing the pinned layer at the bottom and the free layer on top in the spin-valve sensor, the stray field generated from the magnetic nanoparticle landing on top of the sensor can cause stronger response from the free layer than if the free layer is designed at the bottom. Thus, sensor sensitivity can be enhanced because of the shorter particle-free layer distance.

Exchange interactions within the Co/Cu/Co tri-layer can be antiferromagnetic or ferromagnetic, depending strongly on the thickness combinations of the tri-layer. Therefore, magnetization curves of Co/Ru/Co with a variety of thickness combinations were investigated prior to being employed in the spin-valve system, as illustrated in Figure 4.7. The hysteresis loop of the thickness combination, Co (5 nm)/Ru (0.8 nm)/Co (5 nm), shows antiferromagnetic coupling between the two Co layers. On the other hand, Co/Ru/Co with other thickness combinations shows ferromagnetic coupling with a different variety of coercivity.

A complete and optimized GMR multi-layer including seed layers, synthetic antiferromagnetic pinned layers, free layers, and a spacer layer was prepared before

undergoing sensor fabrication steps. Searching for a good antiparallel alignment which expresses a step-like loop in the magnetization curve is important. Therefore, the magnetization curve of the whole structure Ta(2.5 nm)/Ru(5 nm)/Co(5 nm)/Ru(0.8 nm)/Co(10 nm)/Cu(4 nm)/Co(3 nm)/Py(10 nm)/Ta(5 nm) with various measurement angles were investigated, as shown in Figure 4.8.

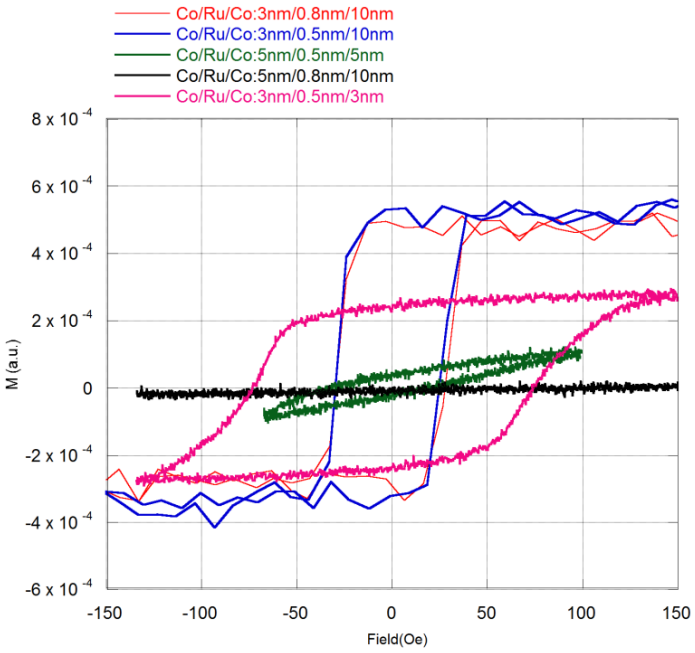

Figure 4.7: In-plane magnetization curves of Co/Ru/Co, showing the antiferromagnetic (black line) and ferromagnetic (others) coupling between two Co layers.

The characteristics of magnetization curve of the GMR multi-layer depends on the angle between the external field and overall easy axis of the multi-layer. As the angle in between ±45°, magnetization curves did not exhibit spin-valve charateristics. Sub-steps were not clearly observed in those curves, indicating there was weak to none pinning field. On the other hand, as the angle around -60°, a plateau-like sub-step in the loop exhibiting a 50 Oe pinning field and 40 Oe coercivity was observed, indicating that best

GMR phenomenon acquired among various measurement angles. The orientation of the easy-axis of the whole spin-valve thin films was recorded and the particular angle setting at which the strongest pinning field was presented was adapted for further sensor fabrication.

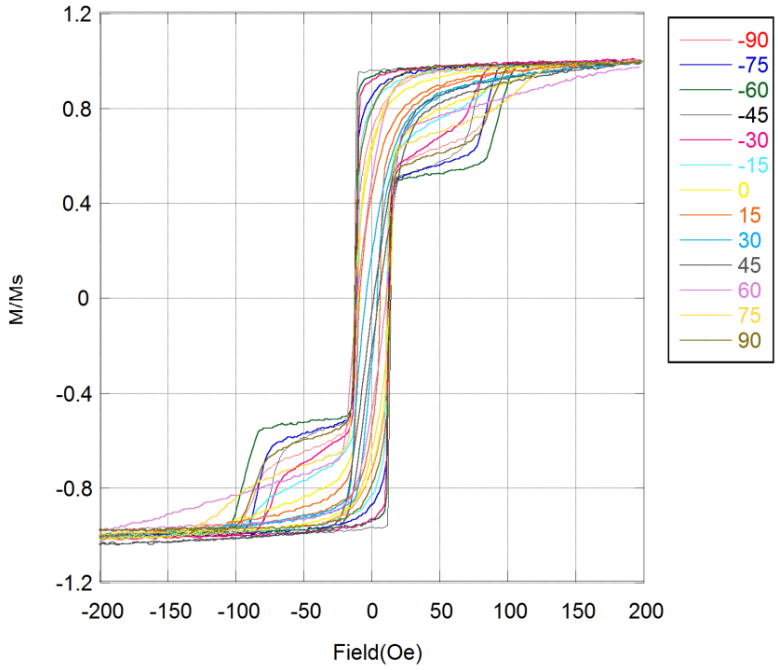

Figure 4.8: The magnetization curve of the multi-layer stack, Ta(2.5 nm)/Ru(5 nm)/Co(5 nm)/Ru(0.8 nm)/Co(10 nm)/Cu(4 nm)/Co(3 nm)/Py(10 nm)/Ta(5 nm) corresponding to various measurement angle between ±90°.

4.1.3 Characterization of the optimum GMR multi-layer stack

Two different orientations of the external field applied on the GMR multi-layer stack were examined. Figure 4.9 shows the GMR result as the external field was applied parallel to the hard-axis of the GMR multi-layer stack. High resistance fluctuations in the range between 1.04 Ohms and 1.06 Ohms were observed as the multi-layer stack was close to being saturated when the external field was larger than ±50 Oe. The cause of this

phenomenon was that magnetic domains in the GMR multi-layer stack flipped out of order as the magnitude and orientation of the external field changed. As the external field increased from 0 Oe to 50 Oe after the multi-layer was saturated, the resistance exhibited a drastic change between ±50 Oe. The pinned layer and free layer in the GMR multi-layer stack were not clearly flipped under different strengths of the external field. Therefore, it is difficult to acquire a significant GMR profile change from particle detection by applying an external field along the hard-axis orientation.

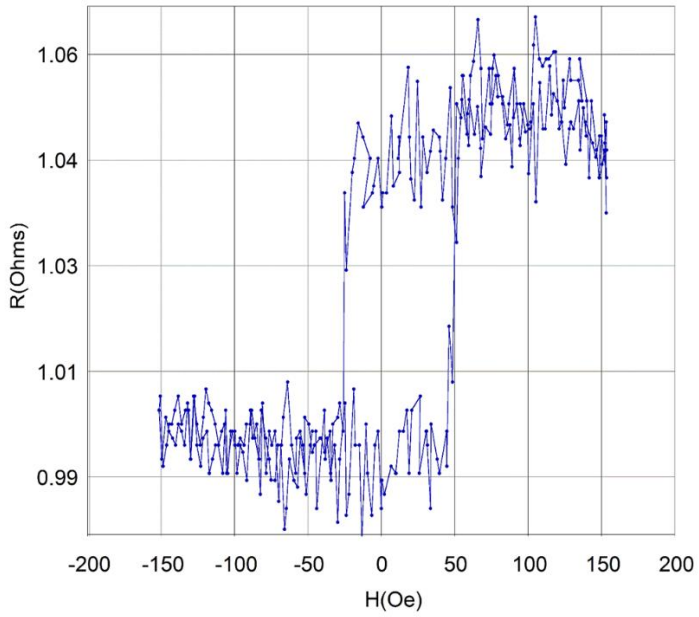

Figure 4.9: The resistance change of GMR multi-layer stack, Ta(2.5 nm)/Ru(5 nm)/Co(5 nm)/Ru(0.8 nm)/Co(10 nm)/Cu(4 nm)/Co(3 nm)/Py(10 nm)/Ta(5 nm) as external field was applied along hard-axis orientation.

Instead of applying the external field along the hard-axis orientation of the GMR multi-layer stack, the GMR sensing scheme adapted the measurement method in which the external field was applied and switched along the parallel and antiparallel orientation of the easy axis. A typical dependence of the GMR multi-layer stack resistance on the

applied external field is shown in Figure 4.10. GMR peaks corresponding to the antiparallel magnetization configuration over a base line corresponding to parallel magnetization configuration of the Co layer in the multi-layer stack can be observed.

In Figure 4.10, the GMR result shows that the two peaks appearing as the external fields were between ±15 Oe and ±75 Oe, which was closely consistent with the two steps in the magnetization curve. A 13% GMR ratio was obtained from GMR multi-layer stack measurement.

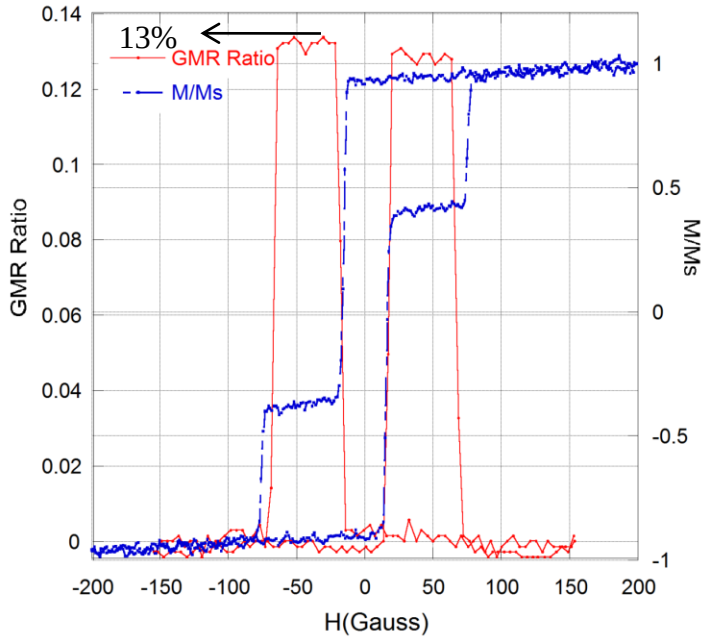

Figure 4.10: The GMR result (solid-line) and magnetization curve (dashed-line) of the GMR multi-layer stack. Two curves show consistency with each other. A 13% GMR ratio was observed.

4.2 Sensor Fabrication

4.2.1 Evaluation of electron beam dose

In order to find an appropriate dose for EBL on the PHOST/PMGI bilayer resist

system, the exposure characteristic was investigated. Figure 4.11 shows the SEM micrographs of the PHOST/PMGI bilayer with various linewidths. Wavy patterns were the result of underexposure. PHOST with a 400 nm linewidth was fully developed at a dose of 8500 μC/cm^2. However, it was necessary to apply no less than 12000 μC/cm^2 to obtain a fully developed PHOST with a 200 nm linewidth and 15000 μC/cm^2 for a fully developed PHOST with 100 nm linewidth.

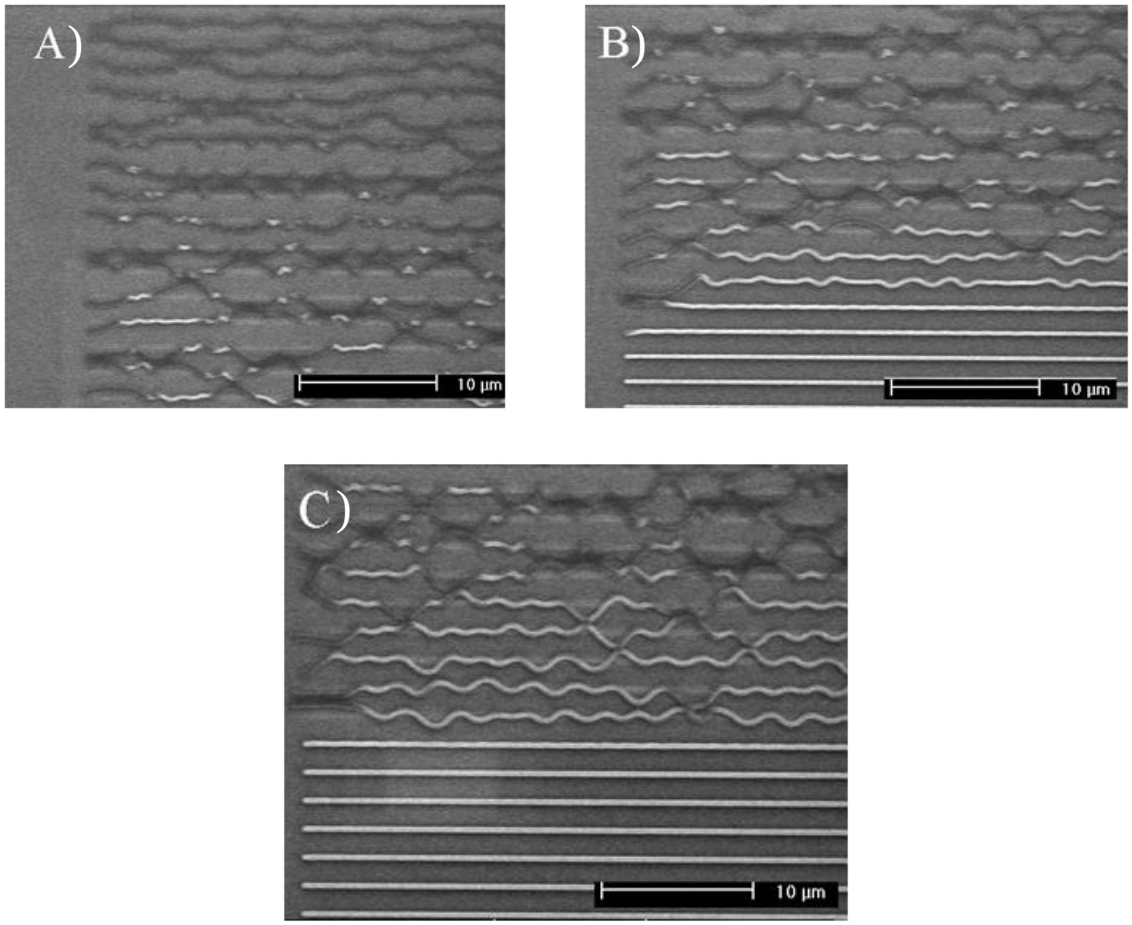

Figure 4.11: SEM image of A) 100 nm, B) 200 nm, and C) 400 nm linewidth of PHOST(500 nm) /PMGI(135 nm) patterned with conditions of EBL dose from 100 to 14000 μC/cm^2 (top to down) at 50kV.

Contrast curves of three linewidth patterns, 100 nm, 200 nm, and 400 nm, are established, as shown in Figure 4.12. The contrast γ is given by the following expression

$$\gamma = (\log \frac{D_{100}}{D_0})^{-1}, \qquad \text{(Eq. 4-1)}$$

where D_{100} represents an exposure e-beam dose for complete resist insoluble and D_0 represents a threshold exposure e-beam dose for resist insoluble.

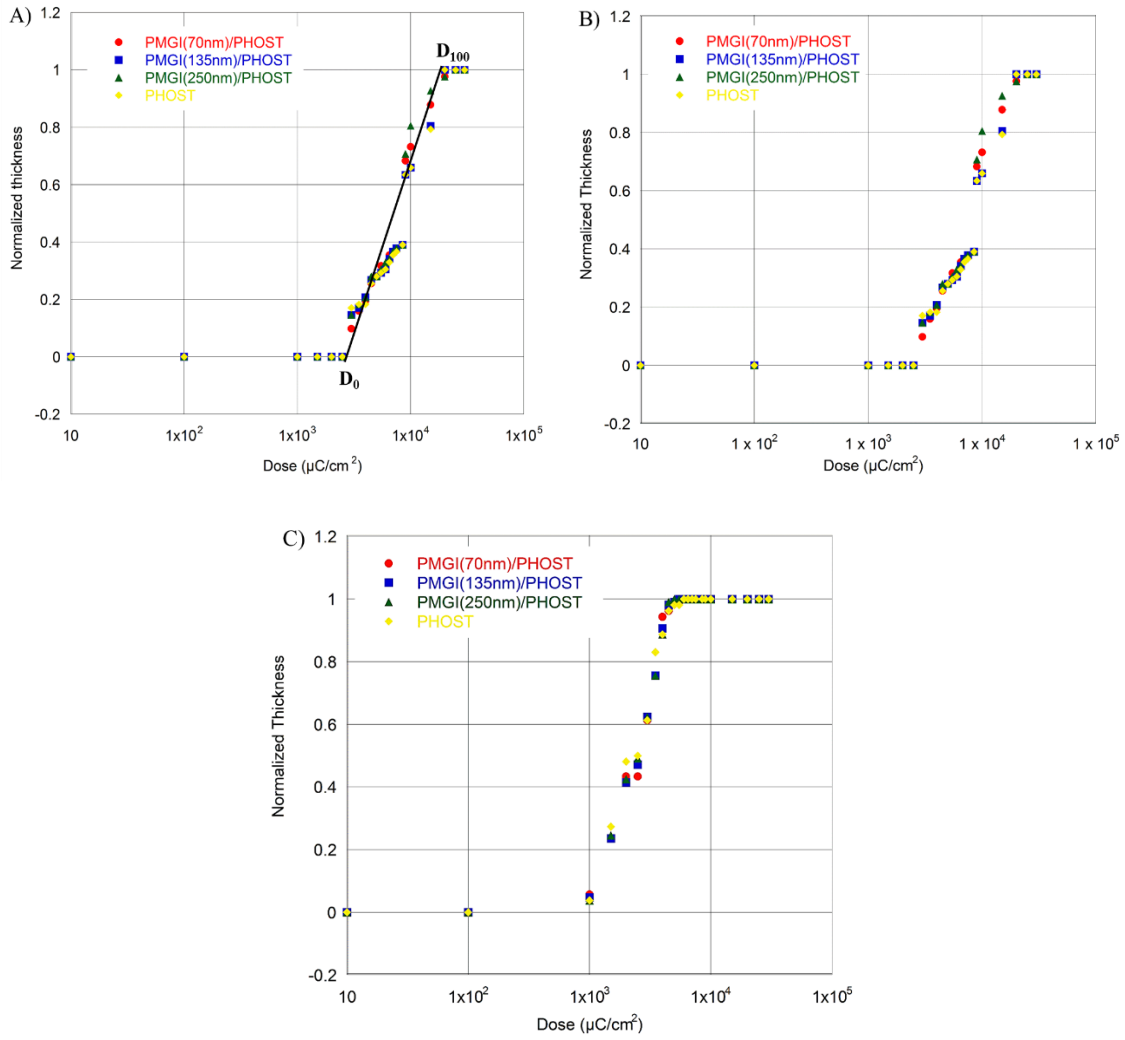

Figure 4.12: The contrast curve of A) 100 nm B) 200 nm C) 400 nm linewidth of PHOST/PMGI patterns with various thicknesses of PMGI underlayer from 0 to 250 nm.

Based on the exposure characteristic, the contrast γ of PHOST was 1.4, 1.2, and 1.0 as the linewidth was 100 nm, 200 nm, and 400 nm, respectively. The result implies good resolution for a vertical resist profile. Moreover, three different thicknesses of the PMGI underlayer, 70 nm, 135 nm, and 250 nm, were deposited in order to investigate whether various thicknesses of PMGI underneath PHOST have a significant influence on exposure characteristics of PHOST.

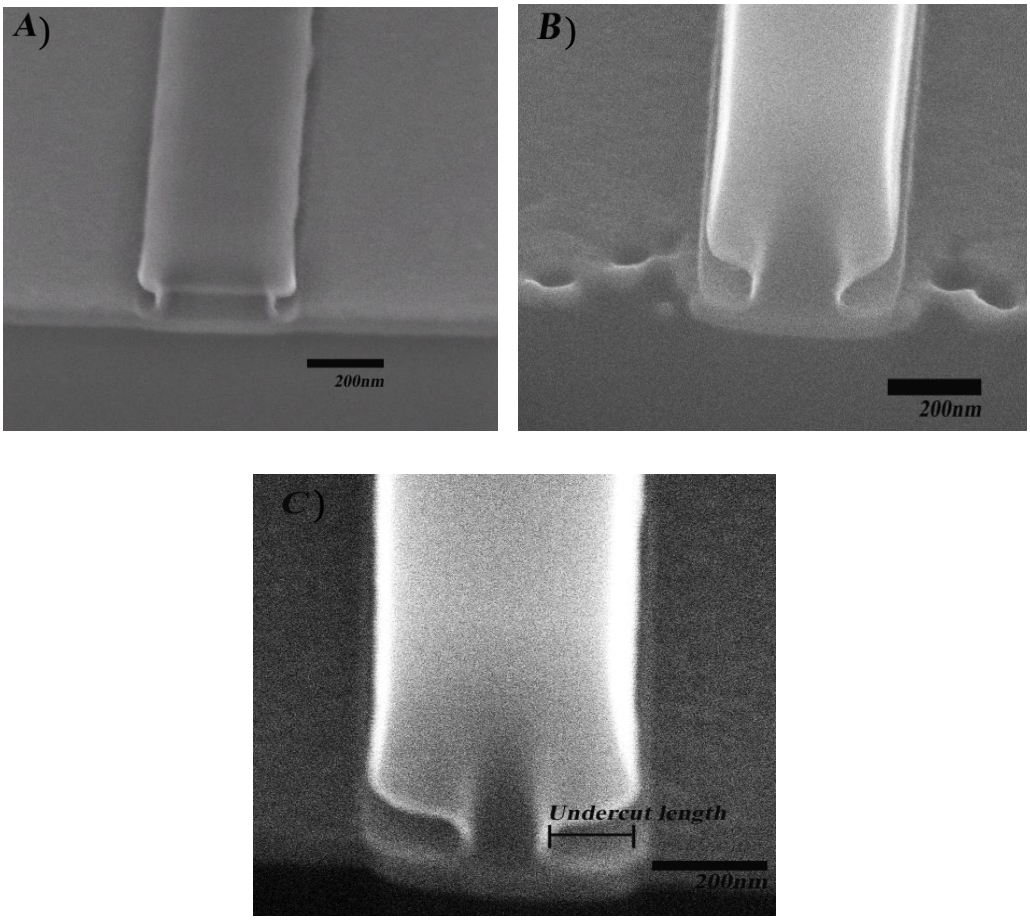

Figure 4.13: SEM image of a cross-section of the 400 nm wide PHOST/PMGI etched in TMAH aqueous solution for A) 30 seconds, B) 40seconds, and C) 50 seconds. The undercut length was 60 nm, 80 nm, and 110 nm, respectively.

According to the results of contrast curves, no significant change in the exposure characteristics of PHOST with any linewidth was found depending on thicknesses of the PMGI underlayer. Therefore, e-beam exposure on a PHOST/PMGI bilayer system can be carried out with the same dose as e-beam exposure on a single PHOST layer.

4.2.2 Undercut configuration on PMGI

In order to facilitate further lift-off processes and create an opening for further Cu layer to be deposited upon the edge of metal line patterns as contacts,an undercut profile was developed and investigated. Undercut length was first determined by etching time, as shown in Figure 4.13. 60 nm, 80 nm, and 110 nm undercut lengths were observed using 0.88% TMAH aqueous as etchant for 30, 40, and 50 seconds, respectively. The undercut rate was approximately 2.1 nm/sec. For self-aligned contact fabrication, the undercut length can not be too long, or the PHOST may collapse, nor too short, otherwise the undercut configuration may disappear shortly after the Ar ion milling process.

4.2.3 Ar ion milling rate

In order to investigate optimal conditions of the Ar ion milling process for metallic pattern transfer, milling rates from two directions, vertical and transverse, of PHOST need to be considered. The PHOST, as a good mask layer, has to survive while those regions unprotected by a patterned PHOST mask are milled thoroughly in a given etching time. In our experiment, a 40 nm thick Ta layer deposited under PHOST/PMGI was prepared for patterning. The thickness change of the GMR multi-layer and PHOST depending on etching time using Ar ion milling with conditions of 34mA, 500V and 1.2×10^{-4} torr was established, as shown in Figure 4.14 A). As an unprotected GMR multi-layer with approximately a 42 nm thickness was thoroughly removed in 75 seconds,

approximately 88% of the original thickness (500 nm) of PHOST still survived, showing that PHOST was an effective mask layer.

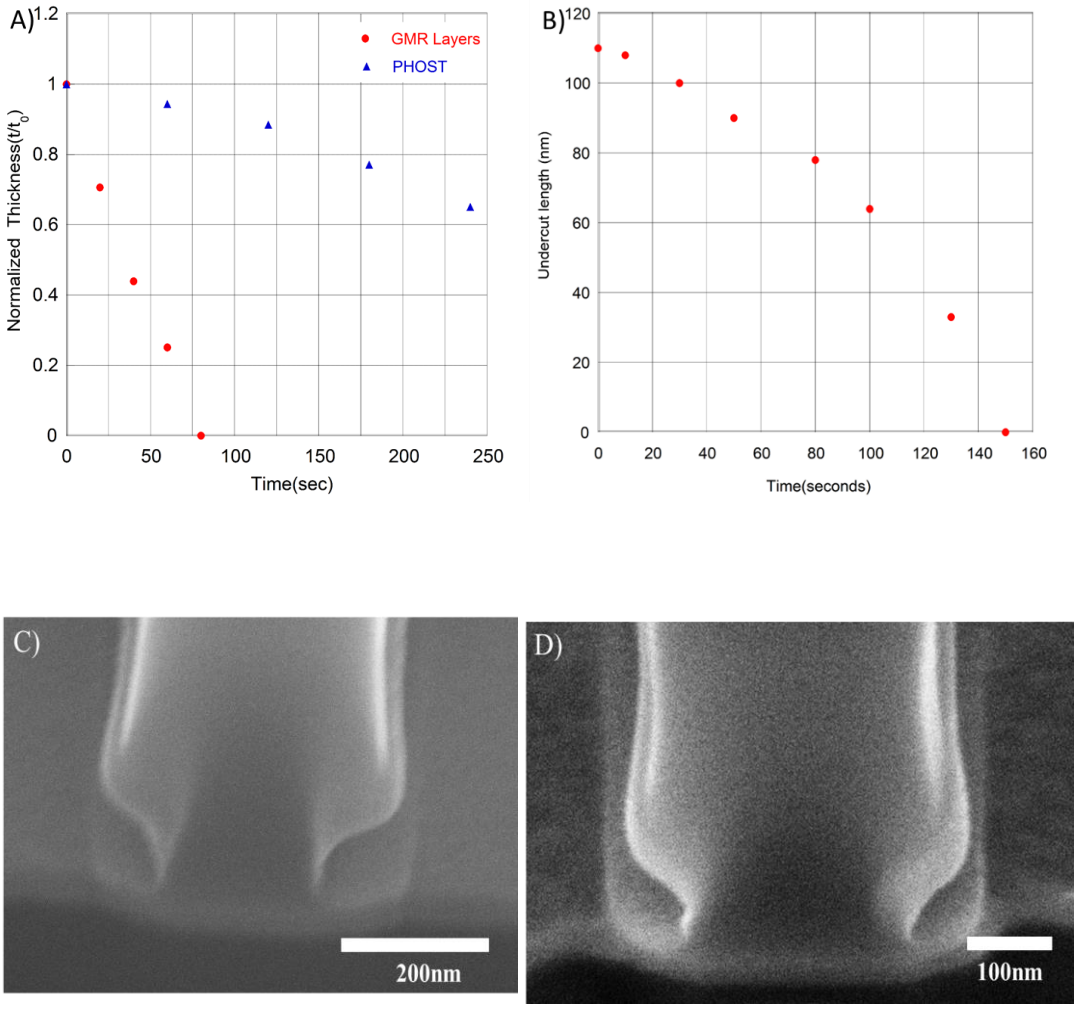

Figure 4.14: A) The normalized thicknesses of GMR and PHOST and B) the undercut length depending on Ar ion milling time. SEM image of the 400 nm wide PHOST/PMGI milled by Ar ion milling for C) 30 seconds, D) 80seconds.

In addition, as Ar ion milling was conducted, not only vertical but also transverse milling occurred. Since transverse milling inevitably damages the undercut profile, the development of the Ar ion milling process also has to be based on the premise of the undercut profile survival when the unprotected GMR multi-layer is thoroughly etched.

Therefore, the dependence of the undercut length of the PHOST/PMGI on the etching time was investigated under the same Ar ion milling conditions mentioned above, as shown in Figure 4.14 B). Figure 4.14 C) shows that the undercut length started to shorten at 30th second. Figure 4.14 D) indicates that the unprotected GMR multi-layer was thoroughly removed whereas the undercut profile survived well enough for further self-aligned Cu contact deposition at 75th second. As a result, an optimal Ar ion milling process for self-aligned contact fabrication was developed.

The limit time for transverse milling was also examined. Although the PHOST/PMGI/GMR line pattern survived after a180-seconds milling process, significant damage of the whole structure was observed. Moreover, the undercut profile completely disappeared and the whole pattern was unable to be used for further sensor fabrication processes, as shown in Figure 4.15.

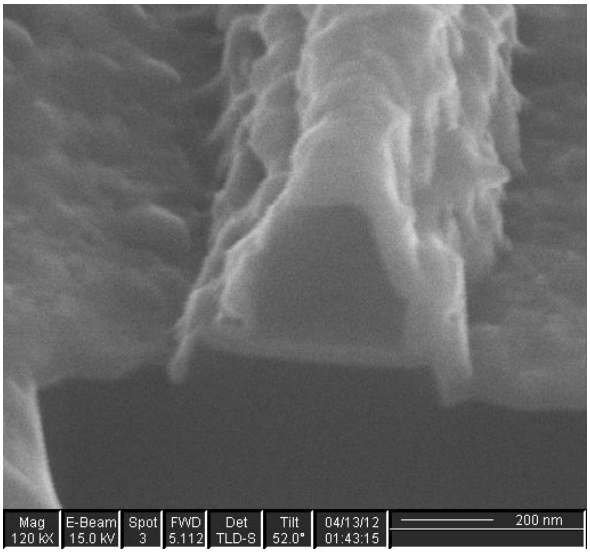

Figure 4.15: The over-etch configuration of PHOST/PMGI/GMR layers after 180 seconds of Ar ion milling process.

After an optimized Ar milling process was conducted, a 70 nm thick Cu layer was spun

deposited on the sample, followed by a lift-off process using a 2% TMAH aqueous solution. As a result, 400 nm wide PHOST/PMGI line patterns successfully transferred into the GMR multi-layer. In addition, the Cu layer was self-aligned, connecting to the GMR multi-layer line pattern, forming an electrical contact surface, as shown in Figure 4.16 A). Two grooves along both edges of the line pattern was due to the higher milling rate at the edges than on the smooth surface of the line pattern in the Ar ion milling process. Figure 4.16 B) shows a top view approximately 60 nm wide with 70nm thick Cu contacts overlapping on both the left and right edges of the 400 nm wide GMR multi-layer line pattern.

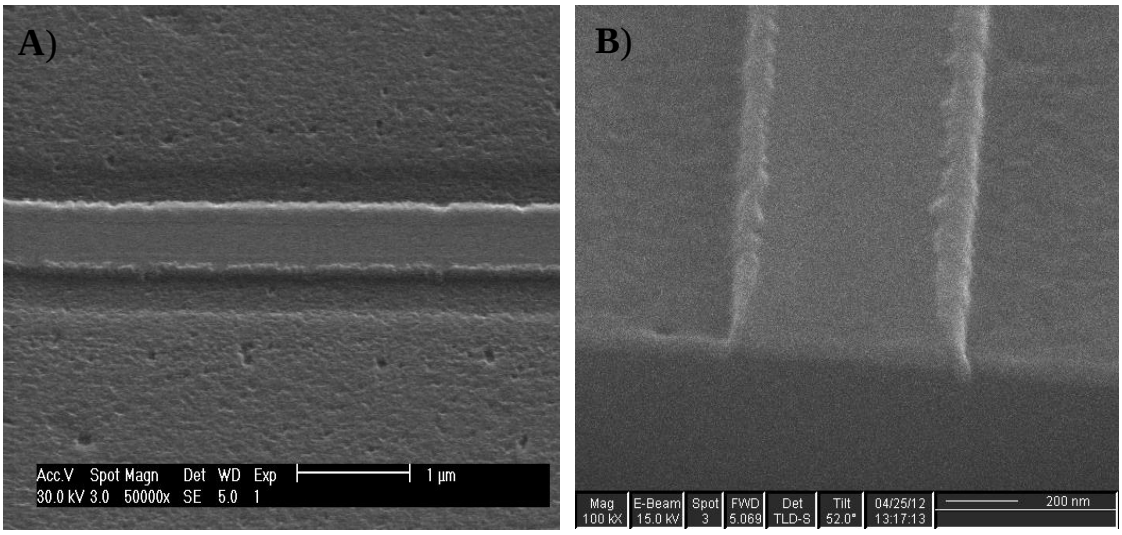

Figure 4.16: A) Tilted SEM image of Cu contact surface connecting to GMR multi-layer line pattern. B) A cross-section image of the line pattern in A). The contact surface overlapped on left and right edges of the GMR line pattern.

4.2.4 Overlay and alignment of lithographic features

After the lift-off process to transfer four 1 µm × 400 nm line patterns to the GMR multi-layer with Cu contact layers on a quarter wafer, PHOST was again spin-coated for

e-beam lithography. Three 150 μm ×400 nm line patterns were aligned and overlapped on top of each previous 1μm ×400 nm GMR multi-layer line pattern, generating a cross configuration. One of the cross configurations is shown in Figure 4.17. The PHOST lines, averaging a 500 nm thickness, were used as a mask layer for a further Ar ion milling process. After the Ar ion milling and PHOST removal process, the Cu contact surface was trimmed to be two 60 μm × 400 nm or 60 μm × 200 nm Cu contact wires, connecting the defined sensing area at both ends. The width of the GMR multi-layer line pattern and the width of the PHOST line pattern defined the sensing area dimension, 400 nm × 400 nm or 200 nm × 400 nm.

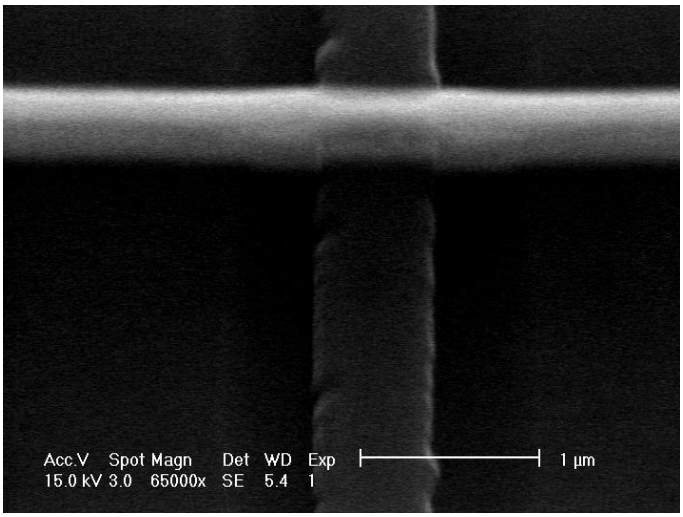

Figure 4.17: The tilted view of a150 μm × 400 nm PHOST line pattern(horizontal line) overlaying on a GMR multi-layer line pattern (vertical line). A cross configuration was generated, defining sensing area and paired Cu wires.

4.2.5 Oxygen RIE rate

The patterned PHOST molecules after e-beam exposure were cross-linked and unable to be dissolved in its solvent, PGMEA. Therefore a new process had to be conducted to

remove patterned PHOST for transferring the patterns. The oxygen reactive ion etching (O_2 RIE) was used here for patterned PHOST removal. The O_2 RIE rates of PHOST, GMR, and Cu were measured to obtain the required time and key conditions for PHOST removal, as shown in Figure 4.18. The high selectivity of PHOST etching over the GMR and Cu layers is required so that damage to Cu, and GMR layers underneath PHOST could be minimized. In Figure 4.18, a 400 nm line-width PHOST with a 500 nm thickness was etched over 200 seconds with the given conditions of 150W, 200V DC bias, 50 sccm oxygen flow rate and under 40 mtorr operating pressure. The thickness of the pattern PHOST decreased linearly till it was etched thoroughly as the etching time reached 210 seconds. The etch rate of patterned PHOST was approximately 2.3 nm/seconds. Whereas the Cu layer and GMR multi-layer both showed nearly zero etch rate under the same etching conditions.

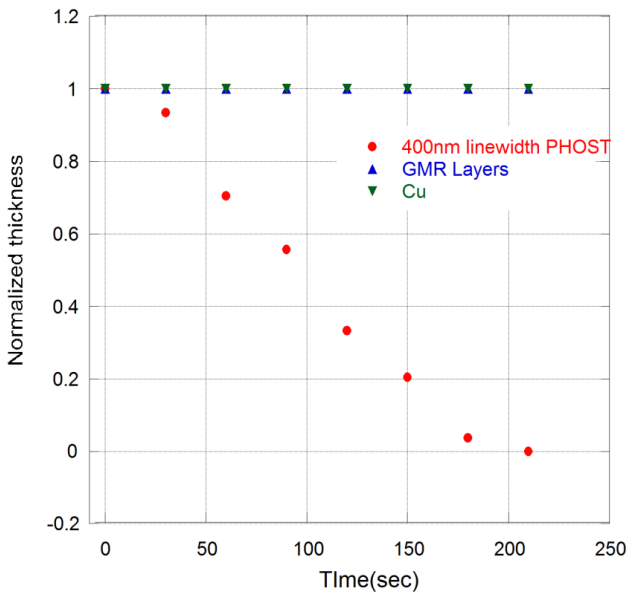

Figure 4.18: The thickness of patterned PHOST, Cu layer, and GMR multi-layer change over O_2 RIE time.

4.2.6 Sensor arrays

Twelve sensor arrays comprised of 400 nm-long sensors with the width varying between 200 nm and 400 nm were built. Those twelve sensors were assigned in a 1.5 mm × 1.5 mm region, as shown in Figure 4.19. The dimension of the first set of contact wires, which connected to the sensor directly, was 200 nm × 60 μm or 400 nm × 60 μm, depending on the desired sensor width. A 400 nm separation between two wires defined the sensor length to be 400 nm. The second set of contact wires partly overlapping on the first set of contact wires was 50 μm wide and separated by 50 μm. A 2 mm × 4 mm contact pad connecting each second set of wire at one end was fabricated to fit for touching 4-point probes.

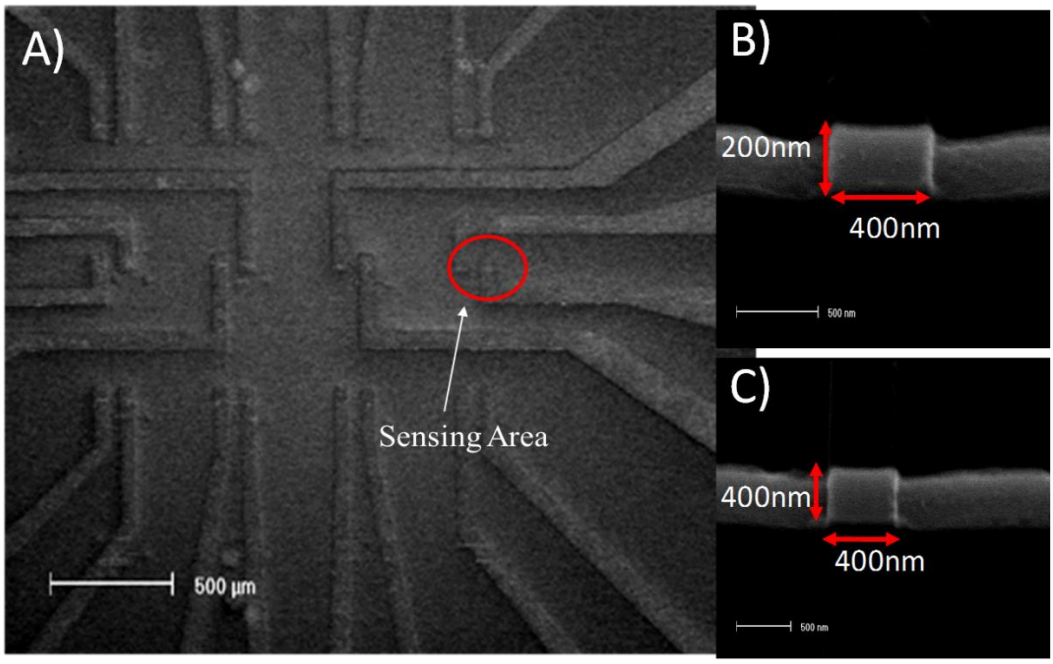

Figure 4.19: SEM micrograph of A) 12 GMR sensors on a chip with Cu contact wires. Two different dimensions of sensing area, B) 200 nm × 400 nm and C) 400 nm × 400 nm and its first set of Cu contact wires.

Based on the previous results, the GMR profiles of the unpatterned GMR multi-layer measured in a 1.5 mm × 1.5 mm region at the center of the wafer were identical, showing the same magnitude of base resistance, and highest resistance. The height and width of the GMR peaks, along with the position of peaks on the external field axis were also nearly identical. However, GMR profiles of several sensors which were fabricated in the same region showed certain levels of difference within each other, as shown in Figures 4.20 and 4.21.

Characteristics of GMR measurements on two different dimensions of the sensor are as follows: First, in 400 nm × 400 nm sensor measurements, base resistance varies in a range of 35.5 Ohms to 49.5 Ohms. In 200 nm × 400 nm measurements, base resistance varied in a range of 136.8 Ohms to 245.8 Ohms. On average the base resistance of 200 nm × 400 nm sensors was higher than the base resistance of 400 nm × 400 nm sensors. This is because the narrower contact wires connecting to the 200 nm × 400 nm sensors lead to the higher resistance. Second, in addition to the two main GMR peaks appearing in Figures 4.20 and 4.21, some GMR profiles exhibited sub-steps in GMR peaks, implying that some magnetic domains in the free layer of the sensor may not flip synchronously.

The profile difference of GMR peaks within the individual sensors with the same dimensions attributes to the edge irregularity and roughness of the sensor caused by the fabrication process. Third, the width of GMR peaks of the 200 nm × 400 nm sensors was distinguishably wider than the width of GMR peaks of the 400 nm × 400 nm sensors. Despite the difference mentioned above, one is still able to clearly recognize the GMR signal from noise in every GMR sensor measurement.

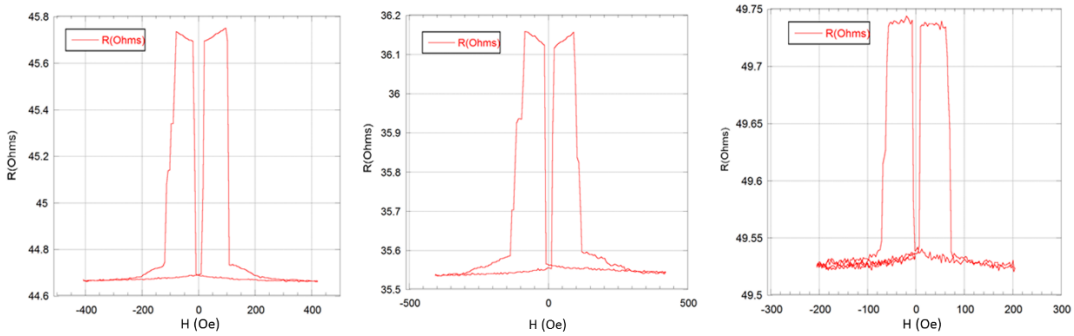

Figure 4.20: Several GMR results of different 400 nm × 400 nm sensors fabricated on a sensor chip.

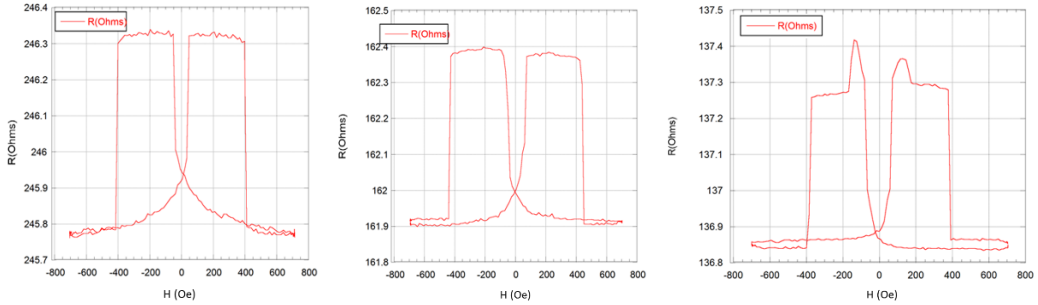

Figure 4.21: Several GMR results of different 200 nm × 400 nm sensors fabricated on a sensor chip.

4.3 Magnetic Particle Detection

4.3.1 50 nm Fe_3O_4 nanoparticles

The magnetization of magnetic particles was investigated prior to the particle detection test by a GMR sensor. The magnetization curve of 50 nm Fe_3O_4 nanoparticles with various weights was obtained using VSM, as shown in Figure 4.22 A).

From the magnetization curve, Fe_3O_4 nanoparticles exhibited ferrimagnetic behavior. The saturation field of 9 mg, 15mg, and 42 mg 50 nm Fe_3O_4 nanoparticles was about 500Oe, 700Oe, and 2000Oe, respectively. Figure 4.22 B) shows that the saturation moment linearly increased with increasing weights of 50 nm Fe_3O_4 nanoparticles. In

addition to the magnetic characteristics investigation, the geometry of 50 nm Fe_3O_4 nanoparticles is obtained. In Figure 4.22 C), irregular, rounded shape nanoparticles are observed.

Two types of preparation of 50 nm Fe_3O_4 nanoparticles were used in the particle detection experiment. The first type is dry-powder nanoparticles. A single layer of dry-powder 50 nm Fe_3O_4 nanoparticles was directly distributed onto the sensor. A GMR profile of the sensor was influenced by these high magnetic moment nanoparticles, as shown in Figure 4.23.

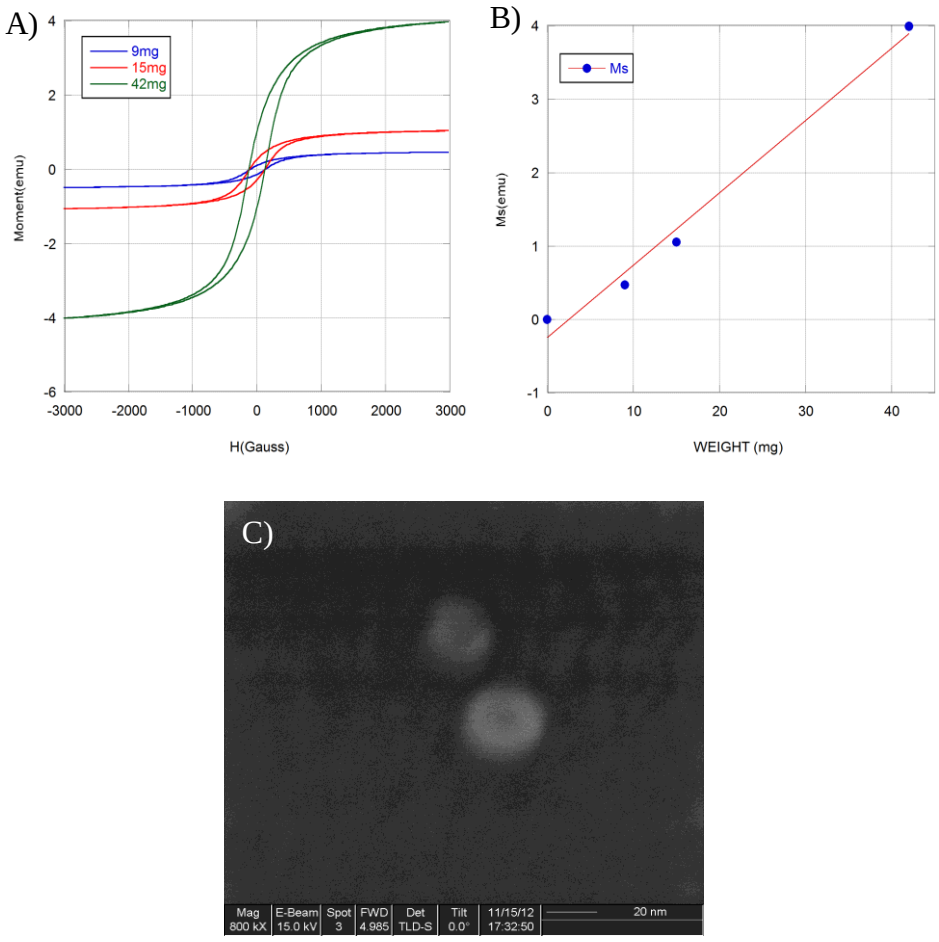

Figure 4.22: A) The magnetization curves of 50 nm Fe_3O_4 particles with 3 different weights. B) The linear relationship between saturation magnetization and the weight of the particles. C) SEM micrograph of 50 nm Fe_3O_4 nanoparticles.

The black solid-line represents the GMR as the sensor was tested without particle coverage whereas the red dashed-line represents the GMR when particles covered on a 400 nm × 400 nm sensor. Both plots are bilaterally symmetric, implying that the GMR results were not influenced by the direction of the external fields. The external field first increased to approximately 280 Oe to make sure the GMR sensor was fully saturated. In the solid-line plot, the resistance started to increase sharply from 79 Ohms as the external field was switched from 280 Oe to -10 Oe and remained at 80 Ohms, the highest resistance in the measurement. As the external field increased to -40 Oe, the sensor resistance dropped sharply back to 79 Ohms, exhibiting approximately 15 Oe coercivity.

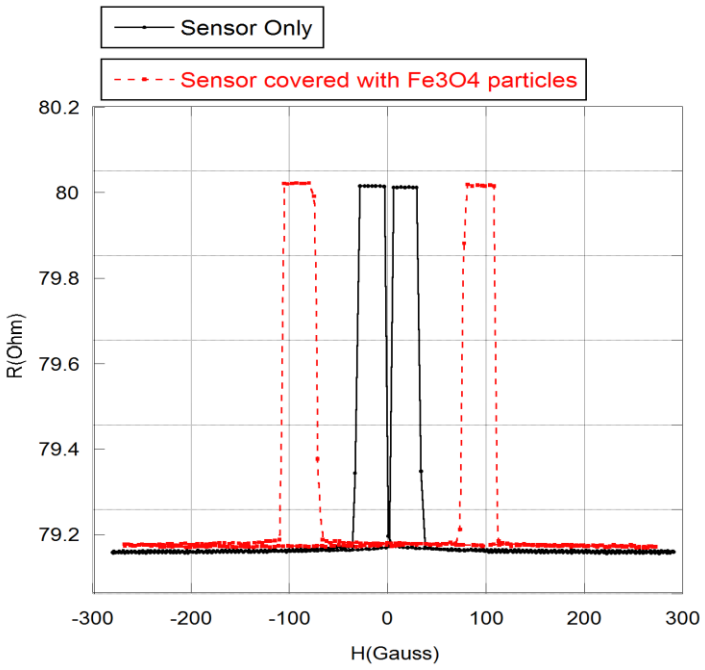

Figure 4.23: The change of GMR peaks of a 400 nm × 400 nm sensor with and without a single layer of dry 50 nm Fe_3O_4 particles coverage.

The dashed-line plot represents the single layer of dry-powder 50 nm Fe_3O_4 particles distributed on the sensor. The resistance did not have significant increase until the

external field reached -80 Oe after applying the saturated field 280 Oe onto the sensor, indicating an extra 70 Oe external field required to flip the free layer of the sensor. Compared to the GMR result of the sensor without particle coverage, two GMR peaks separated more as the sensor was covered by dry 50 nm Fe_3O_4 particles. Thus, particle coverage on the sensor increased the overall pinning field applied on the sensor. However the width of the GMR peaks remained the same, showing that the coercivity of the sensor was not affected by the particles. Although the capability of this sensing system was successfully verified, the method of particle distribution still needed to be improved in order to achieve a single particle detection scheme.

In order to enhance particle attachment and dispersion on top of the sensing area, the second type of particle preparation was used. 50nm Fe_3O_4 particles were stored and dispersed in ethanol solution at a 0.066 mg/ml concentration. 100 μl of the particle solution was dropped from the top of the sensor chip center and constrained in a 25 mm^2 circular area to reduce the particles landing on a non-sensing area. The GMR result had been tested as the external field swept in between 400 Oe to -400 Oe in 30 seconds. Each GMR result was recorded at five-minute intervals for 20 hours. Figure 4.24 shows the GMR profile change as particles fell down to the sensor surface starting from 0 hours to the 20th hour. The base resistance increased over time due to the damage of the sensor and sensor contact wires caused by the particle solution. More and more particles falling to the sensor surface and sticking on either the sensing area or part of sensor wires during the measurement time might also cause an increase of the base resistance. Although the Figure 4.24 shows the peak shape was also affected by such damage, the resistance change attributing to the GMR phenomenon still can be observed and recognized from

noise over time.

Figure 4.25 shows the 2-dimentional R-H plots extracted from Figure 4.24 in a time interval between the 600th and 825th minute. Two GMR peaks, starting from the 660th minute, gradually separate further apart. At the 765th minute, the two peaks exhibited the largest separation. In the positive field region, a sudden increase of the resistance occurred as the external field reached 80 Oe at the 645th minute but shifted to 150 Oe at the 765th minute. A similar transition occurred in the negative field region.

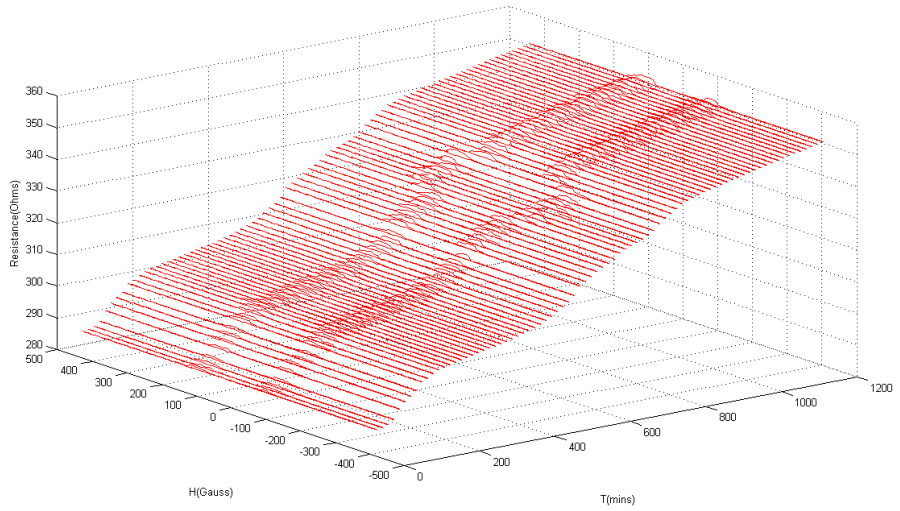

Figure 4.24: 3-dimension plot of resistance change of a 400 nm × 400 nm sensor influenced by particles over time.

In addition, the GMR peaks, though they vary irregularly, tended to be wider from the 600th to the 765th minute, implying that the coercivity of the sensor was also influenced by the attachment of 50 nm Fe_3O_4 particles. After the 765th minute, it was observed that the characteristic of GMR peaks turned back to those before the 600th minute. Even though the magnetic characteristic returned to the initial state, the overall resistance still

went higher with increasing time. The explanation of this phenomenon is that as more and more magnetic nanoparticles landed on the sensing area, the dipole-dipole moments and the magnetic exchange coupling within magnetic particles diminished the stray field applied on the sensing area, leading to insignificant magnetic characteristic change. Besides, if particles aggregate together and form a sheet configuration on the sensor surface, the distance from the dipole of the sheet configuration would be very far to the sensing area, leading to a very low stray field sensed by the sensor. At the same time, more and more particles accumulating on the sensor contributed to higher and higher sensor resistance.

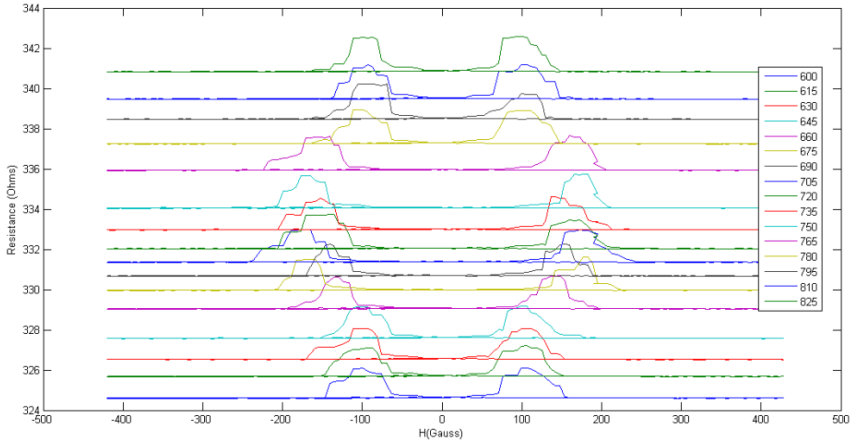

Figure 4.25: The GMR profiles from 600th minute to 825th minute at 15 minutes interval.

4.3.2 100 nm Fe_3O_4 nanoparticles

In addition to the 50 nm Fe_3O_4 nanoparticles detection test, 100 nm Fe_3O_4 nanoparticles stored in ethanol solution were also prepared for detection by a 400 nm × 400 nm GMR sensor. The magnetization of 100 nm Fe_3O_4 nanoparticles was first

investigated, as shown in Figure 4.26. In Figure 4.26 A), the particles were fully saturated, showing approximately a 1000 Oe anisotropy field. The magnetization curve is consistent with ferrimagnetic behavior. In Figure 4.26 B), the particles were magnetized by the external field sweeping between 500 Oe and -500 Oe, close to the external field applied on the sensor when the detection measurement was conducted. To calculate a single particle moment, the density of Fe_3O_4 particles is introduced and known as 5 g/ml. The moment per gram of the measured Fe_3O_4 particles was approximately 5.4 emu/g as the external field was zero and 19.5 emu/g as the external field was 200 Oe. Therefore, by calculation, each 100 nm Fe_3O_4 particle was able to give approximately 14 femu magnetic moment when the external field was zero and approximately 51 femu when the external field was 200 Oe.

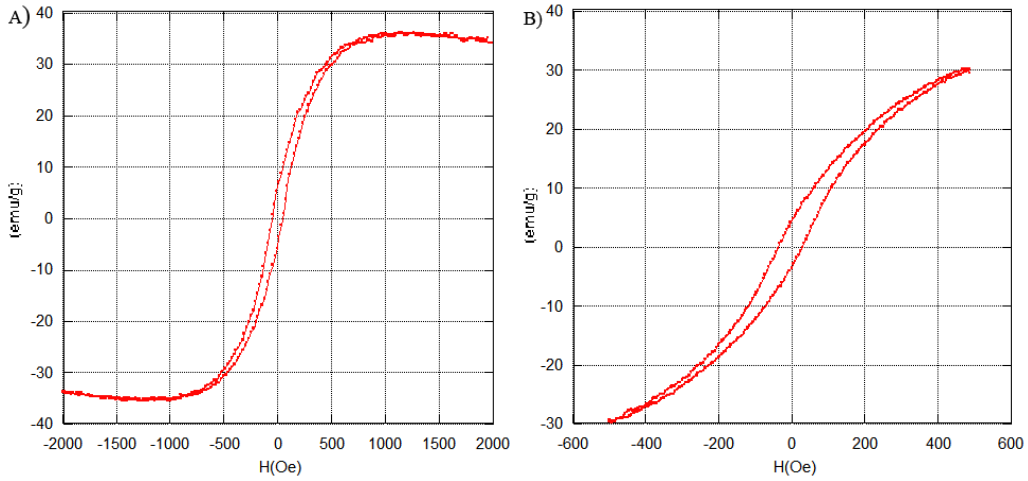

Figure 4.26: The magnetization curve of 100 nm Fe_3O_4 particles, A) which were fully saturated and B) measured in a range of external field sweeping between 500 Oe and -500 Oe.

To conduct 100 nm Fe_3O_4 particle detection tests, the particles were first disolved in

ethanol solution. The concentration allowed the particles to land on the sensing area with the highest probability while avoiding a large amount of particle aggregation. The 100μl particle solution was dropped onto the surface of the sensor array area. The particles fell from the top and precipitated gradually onto the sensing surface over a period of time. In Figure 4.27, the SEM micrograph shows approximately ten 100 nm Fe_3O_4 nanoparticles attached to the top of the sensing area and several others attached to the top of the adjacent Cu wires.

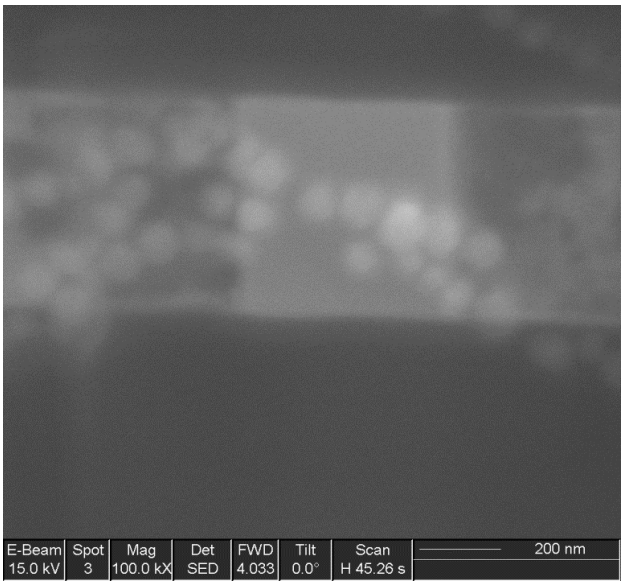

Figure 4.27: The SEM micrograph of several 100nm Fe_3O_4 particles attaching on the sensing area and paired Cu wires.

The profile of GMR peaks before and after several 100 nm Fe_3O_4 nanoparticles landed on a 400 nm × 400 nm sensor is shown in Figure 4.28. As particles landed on the sensing area, the width of GMR peaks were wider than those as particles did not land. As a result, the coercivity of the sensor was influenced by those particles landing on the sensing area and increased by approximately 20 Oe. In addition, the resistance difference, ΔR, which

only depends on free- and pinned- layer relative orientation, did not increase with the increased overall resistance. Hence, a decrease in the GMR ratio was observed.

The GMR of the sensor was measured again after the attached particles were washed away by using an ethanol solution with ultrasonic agitation for 10 minutes. The sensors were verified through SEM to confirm there were no particles left on the sensing area. In Figure 4.28, the sensor after particles were removed exhibited the same GMR profile as the sensor before particles were introduced.

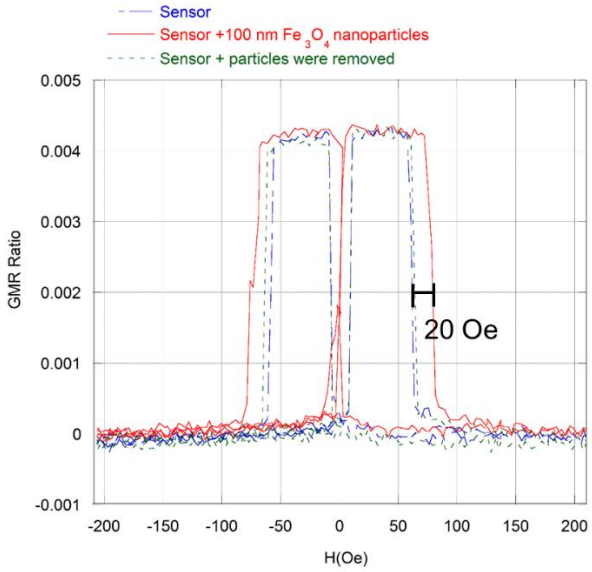

Figure 4.28: The GMR profile change of a 400 nm × 400 nm depending on whether several 100 nm Fe_3O_4 nanoparticles landing on the sensing area.

4.3.3 225 nm Fe_3O_4 nanoparticles

100 µl of 225 nm Fe_3O_4 nanoparticles dissolved in ethanol at a concentration of 0.18 mg/ml was dropped on the top of the sensor arrays, a similar process used for 100 nm Fe_3O_4 nanoparticles measurement. The saturation magnetization curve of the particles measured by VSM is shown in Figure 4.29 A). The highest magnetic moment was 58 emu/g when the saturation field was around 1000 Oe. The ferrimagnetic behavior was

verified from the magnetization curve. In Figure 4.29 B), the particles were magnetized by the external field sweeping between 500 Oe and -500 Oe, similar to the external field applied on the sensor as the particle detection was conducted. Although the M_r here was 4 emu/g, smaller than the M_r of the 100 nm Fe_3O_4 nanoparticle, the magnetic moment of a single 225 nm Fe_3O_4 particle had a higher strength than the magnetic moment of a single 100 nm Fe_3O_4 particle. The moment per gram of the measured Fe_3O_4 particles was approximately 1.5 emu/g when the external field was zero and 15 emu/g when the external field was 200 Oe. Therefore, by calculation, each 225 nm Fe_3O_4 particle was able to give an approximately 45 femu magnetic moment when external field was zero and increase to approximately 450 femu when the external field increased to 200 Oe.

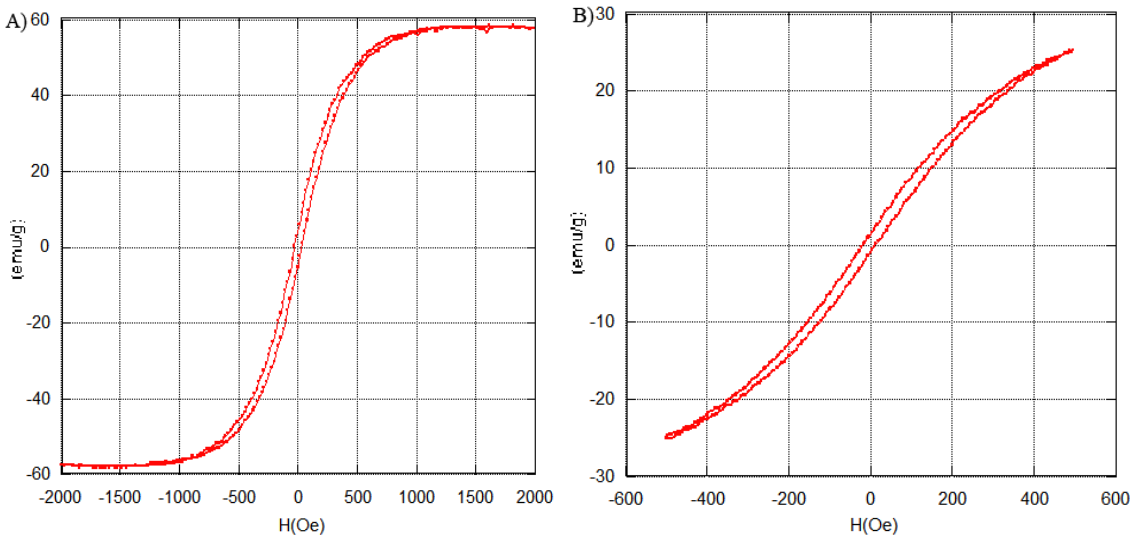

Figure 4.29: The magnetization curve of 225 nm Fe_3O_4 particles, A) which are fully saturated and B) measured in a range of external field sweeping between 500 Oe and -500 Oe.

An SEM micrograph of a single 225 nm Fe_3O_4 nanoparticle landing on the top of the 400 nm × 400 nm sensor confirmed the single particle detection in GMR measurement,

as shown in Figure 4.30. The change of the GMR profile before and after a single particle attached to the sensing area is shown in Figure 4.31. When a single nanoparticle was detected, the GMR peak on the positive external field region was 24 Oe wider than the one corresponding to the sensor without the appearance of any particles. The GMR peak on the negative external field region was not as wide as the one on the positive external field region and was approximately 20 Oe wider than the one corresponding to the sensor without the appearance of any particles. This result demonstrates that the largest sensor coercivity increase was from 48 Oe to 60 Oe as well as successfully presenting the capability of our GMR spin-valve based sensor to detect a single magnetic bio-label.

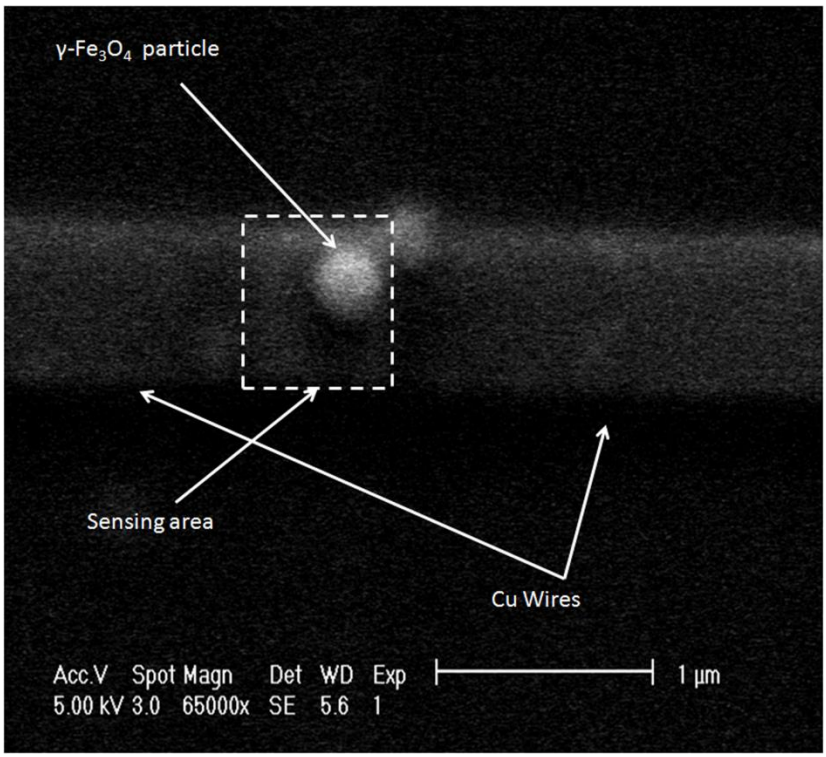

Figure 4.30: A single 225 nm Fe_3O_4 nanoparticle landed on the 400 nm × 400 nm sensing area.

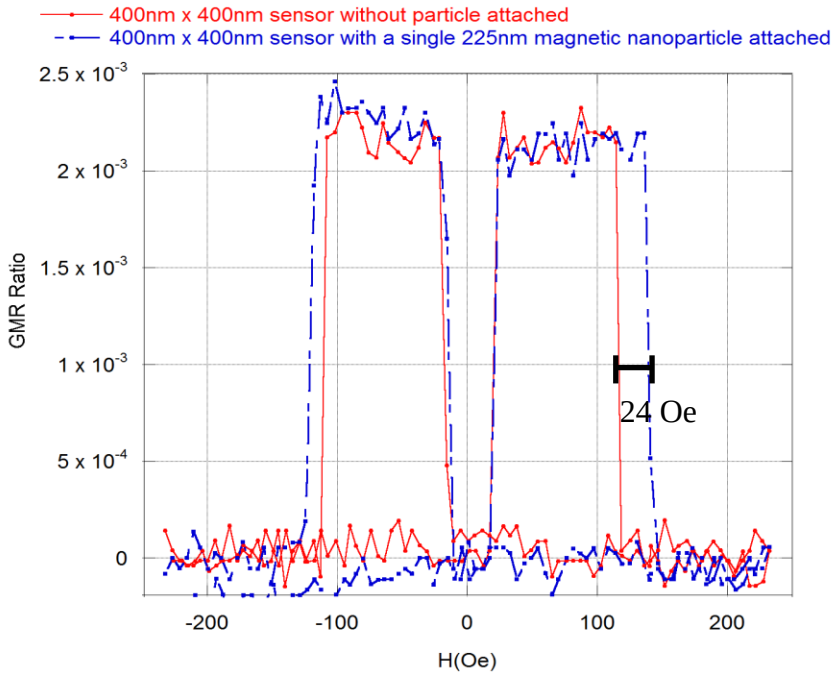

Figure 4.31: The profile change of GMR peaks before and after a single 225 nm Fe_3O_4 particle attaching on 400 nm × 400 nm sensing area.

4.4 Corrosion Test

To evaluate corrosion resistivity of the Al_2O_3-coated sensor, the influence of the deposition of a 25 nm thick Al_2O_3 passivation layer on the GMR was first examined. In Figure 4.32, the GMR of a sensor exhibited a similar profile whether a 25nm thick Al_2O_3 passivation layer was deposited or not. Neither a resistance increase nor a magnetization change was observed. Thus, the influence of the passivation layer on the sensor GMR can be regarded as negligible.

Next, a 100 μl 0.1M PBS solution containing 225nm Fe_3O_4 nanoparticles was prepared and dropped onto the sensing area. After five hours, the sensing area without 25nm thick Al_2O_3 layer coated was completely damaged; on the other hand, no significant corrosion

was observed on the surface of the sensing area covered by a 25nm thick Al_2O_3 layer, as shown in Figure 4.33.

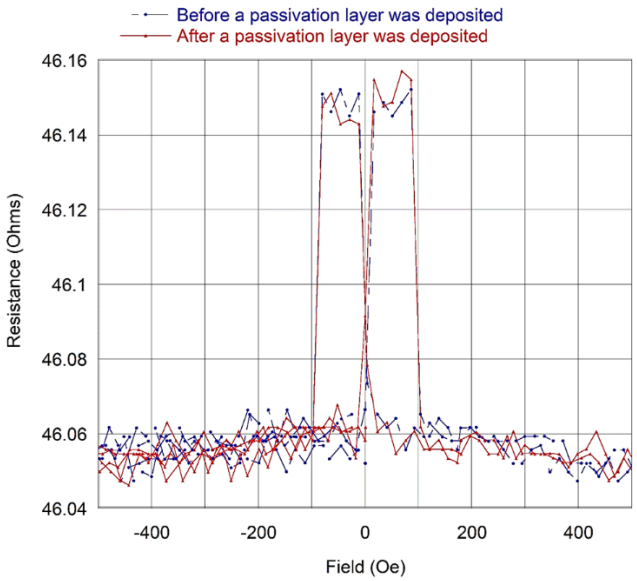

Figure 4.32: The GMR profile of a sensor before and after covered by a passivation layer.

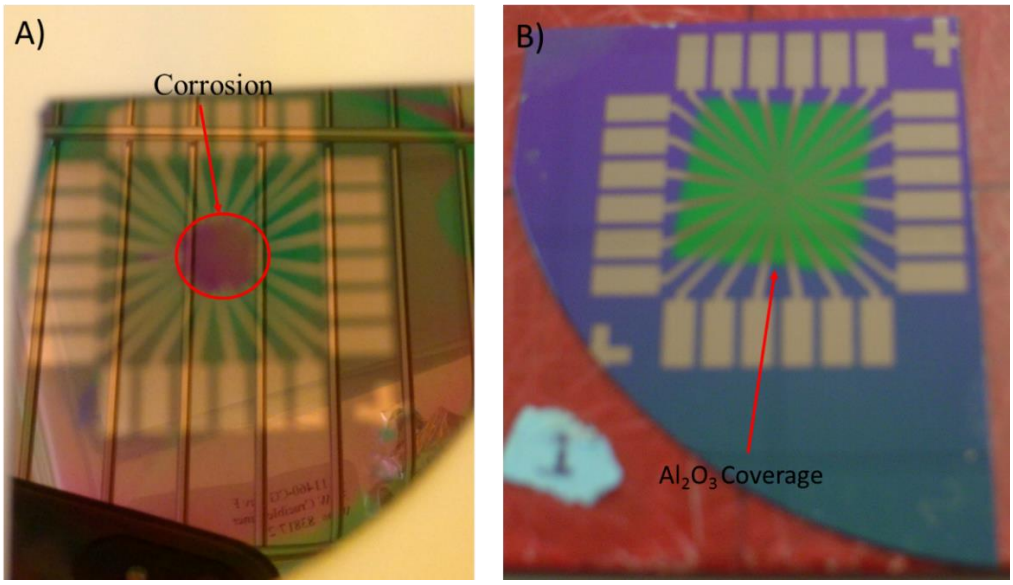

Figure 4.33: Corrosion tests on the GMR sensor A) without a 25nm thick Al_2O_3 layer coverage on the sensing area and B) with a 25nm thick Al_2O_3 layer protection on the sensing area for 5 hours.

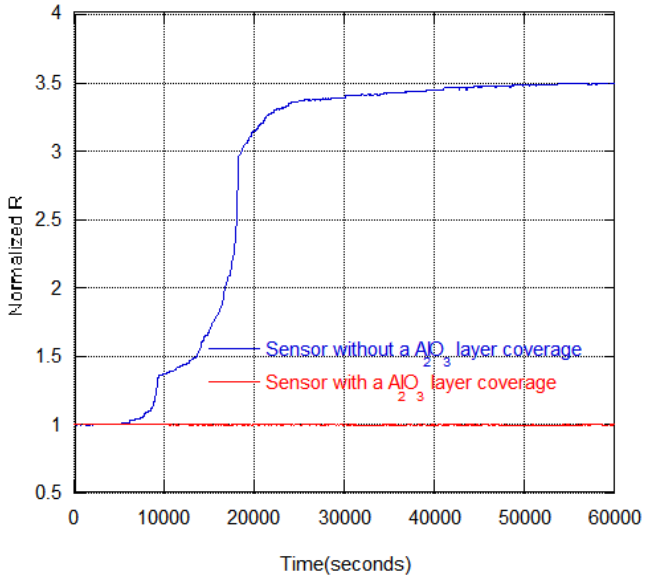

Figure 4.34: The resistance change of a GMR sensor with and without Al_2O_3 layer coverage over time.

Tests of sensor corrosion resistivity were also performed by introducing diluted a PBS solution. A 100 µl 0.01M PBS solution containing 225nm Fe_3O_4 nanoparticles was prepared and dipped onto the sensing area. The resistance change of the sensor was recorded every five minutes for 16.5 hours, as shown in Figure 4.34. The red plot stands for the normalized resistance change of the sensor covered by a 25 nm thick passivation Al_2O_3 layer and the blue plot stands for the result of the sensor without a passivation layer on top. Normalized resistance is defined as the ratio of each measured resistance to the initial resistance at time zero. Although no significant corrosion was found by direct observation of the sensor chip, the resistance test showed different consequences from the sensor with and without the passivation layer coverage. Compared to the resistance of the sensor with a passivation layer protection, the sensor without a passivation layer coverage exhibited a significant resistance increase over time. The unprotected sensor suffered continuous damage caused by the electrolysis process till the solution was completely

dried out. After 16.5 hours, the resistance was approximately 3.5 times larger than the initial state.

4.5 Simulation Results of Particle Sensing

4.5.1 Sensor models

The micro-magnetic behavior of the GMR sensor was first investigated. A 3-dimensional GMR sensor model comprised of a 400 nm × 400 nm GMR-based sensor on an x-y plane with the structure of Co(9 nm)/Cu(6 nm)/Co(3 nm)/Py(9 nm) was built. The thickness of each layer was set to parallel the z-direction. A 0.2 mA time-independent current was applied on the sensor model. In order to create a GMR sensor model which exhibits the result similar to the experimental data, the finite parameters of the GMR sensor were assumed and adapted in reasonable criteria. The assumption has been made that the bottom Co layer was pinned by its antiferromagnetic exchange stiffness, A_{sp}, with the spacer layer.

Various strengths of A_{sp}, from 0 to -0.1 μerg/cm, were examined. A comparison of the hysteresis loop of the sensor with varying A_{sp} is shown in Figure 4.35. When A_{sp} was zero, the loop did not exhibit any sub-steps, implying the pinning field applied to the bottom Co layer was zero. An antiferromagntic exchange coupling between the bottom Co layer and the spacer layer increased with increasing A_{sp}. The magnetization curve of the GMR sensor clearly shows two flat sub-steps in the loop as A_{sp} was approximately -0.1 μerg/cm. In this case, the anti-parallel configuration of two ferromagnetic layers sandwiched by the Cu layer sustained in a certain range of the external field, which was similar to the experimental observation.

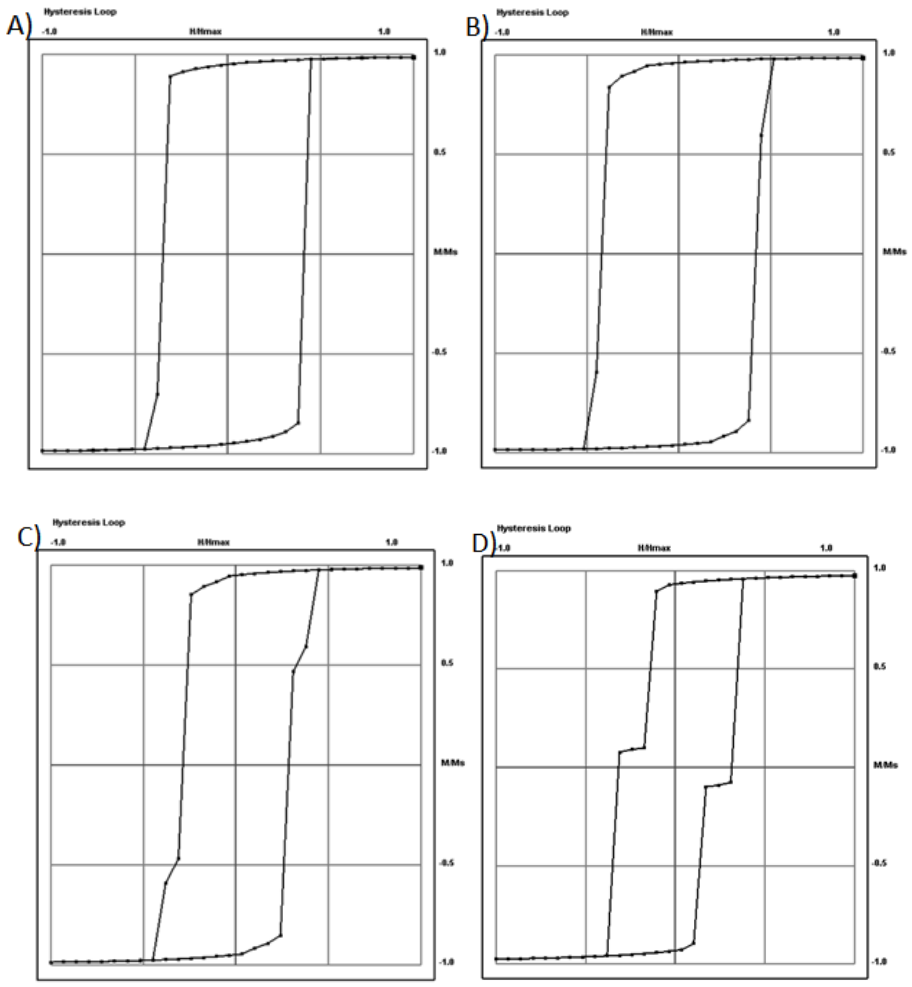

Figure 4.35: Comparison of the magnetization curve of the 400 nm × 400 nm GMR sensor comprised of Co (9 nm)/Cu (6 nm)/Co (3 nm)/Py (9 nm) with various of A_{sp}: A) 0 B) -0.025 C) -0.05 D) -0.1 μerg/cm.

GMR peaks corresponding to the antiparallel magnetization configuration over a base line corresponding to the parallel magnetization configuration of the two Co layers in the sensor was also observed, as shown in Figure 4.36. The resistance change of the GMR sensor was measured and affected by local resistivity which depends on the magnetization alignment of the micro-magnetic domains of the free and the pinned layer. The GMR result exhibited approximately a 4% GMR ratio, 100 Oe pinning field and 70 Oe coercivity.

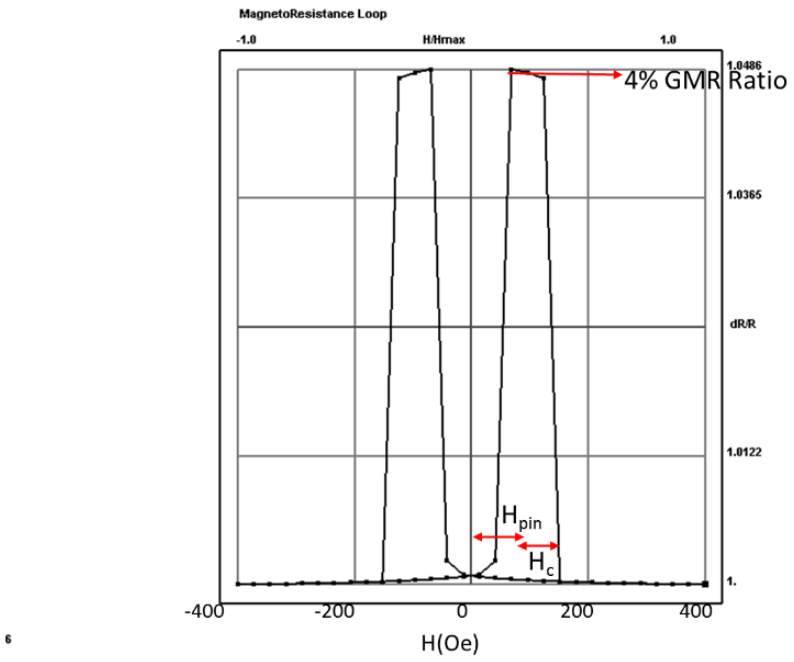

Figure 4.36: The GMR profile of the simulated 400 nm × 400 nm sensor.

4.5.2 Effect of particle properties on GMR

How an additional magnetic nanoparticle affecting the sensor GMR profile with different particle magnetic conditions is illustrated. Several simulations calculated by the LLG equation were conducted as follows.

To understand the effect of K_c and M_s of a particle on the GMR simulation, a model comprised of a 100nm sphere magnetic particle attaching to a 400 nm × 400 nm GMR sensor was simulated. In Figure 4.37, a 100nm particle with M_s = 280 emu/cc and K_c= 2.0×10^5 erg/cc was built on top of the GMR sensor model. First, all magnetic domains in the particle and the sensor were fully saturated along the +x-direction under a given external field, as shown in Figure 4.37 A). Next, the free layer and pinned layer exhibited an anti-parallel configuration when the external field increased from zero along –x-direction, as shown in Figure 4.37 B). All magnetic domains in the particle also flipped to

the –x-direction under certain strengths of the external field. Neither inconsistent magnetic domains in each magnetic layer nor domain walls were observed. When the external field was more than -200 Oe, the particle and the sensor were fully saturated and magnetization was along the –x-direction, as shown in Figure 4.37 C). Similar processes shown in Figure 4.37 B) to C) were observed as the external field increased from zero and was applied along the +x-direction. The magnetic domains flipped synchronously in either the free or the pinned layer, as shown in Figure 4.37 D). The free layer flipped to the +x-direction while the pinned layer remained in the opposite one, generating an anti-parallel configuration again. As the external field exceeded 200 Oe, as shown in Figure 4.37 E), magnetization of all magnetic domains in either the particle or the sensor flipped back to the +x-direction. Figure 4.37 F) shows the GMR profile of this particle-sensor model. Because of the appearance of exchange bias from the particle, the GMR peaks were wider than those in Figure 4.36. However, the significant influences on the GMR ratio and resistance were not observed due to the appearance of the particle.

Next, Figure 4.38 shows particle-sensor model behavior and the GMR profile under different strengths and orientations of the external field when M_s and K_c of the particle was 280 emu/cc and 2.8×10^5 erg/cc. First, all magnetic domains in the particle and the sensor were fully saturated along the +x-direction under a given external field, as shown in Figure 4.38 A). Next, two magnetic layers exhibited an anti-parallel configuration when the external field increased from zero along the –x-direction, as shown in Figure 4.38 B). Neither inconsistent magnetic domains in each magnetic layer nor domain walls were observed. When the external field was more than -200 Oe, the particle and the sensor were fully saturated and magnetization was along the –x-direction, as shown in

Figure 4.38 C). On the other hand, as the external field increased from zero and was applied along the +x-direction, the magnetic domains did not behave synchronously in either the free or the pinned layer, as shown in Figure 4.38 D). Half of the free layer flipped to one direction and the other half, separated by a domain wall, did not flip and remained in the opposite direction until the external field exceeded 200 Oe, as shown in Figure 4.38 E). Thus, two GMR peaks showed no identical profile as indicated in Figure 4.38 F).

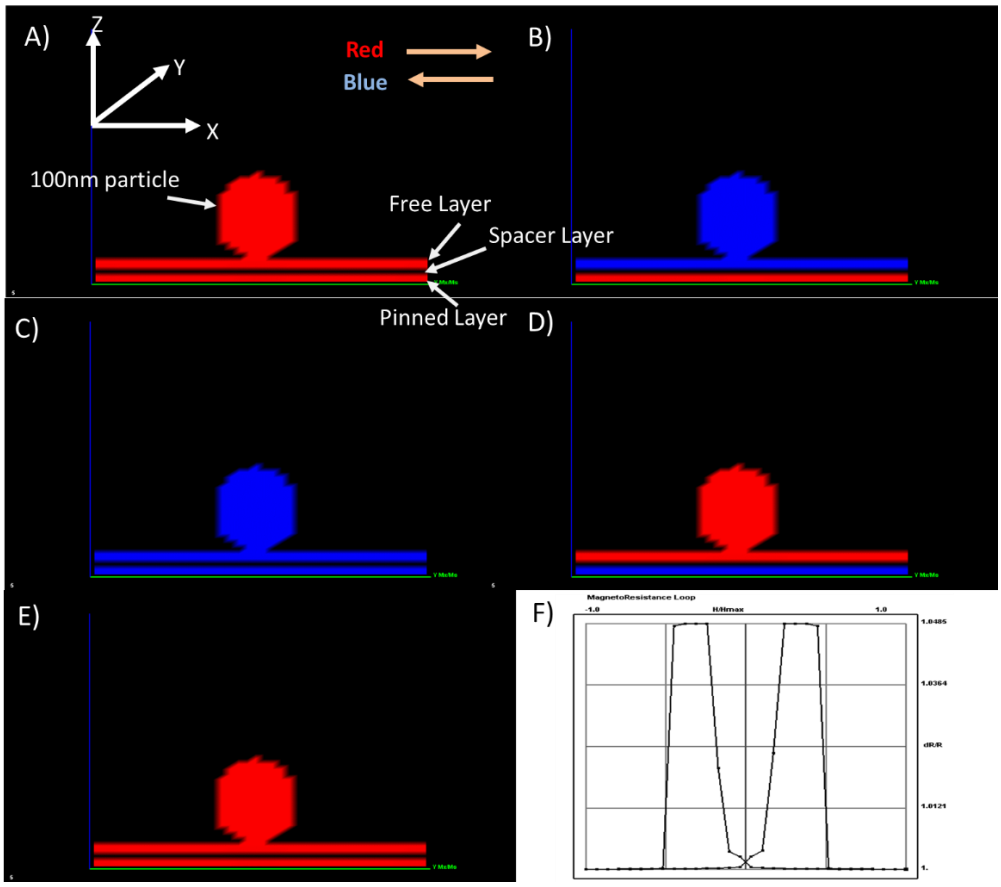

Figure 4.37: The magnetic orientation of sensor-particle model varied at five continuous states, starting from A) to E). F) The GMR profile of sensor-particle model. M_s and K_c of the 100nm particle were 280 emu/cc and 2.0×10^5 erg/cc, respectively.

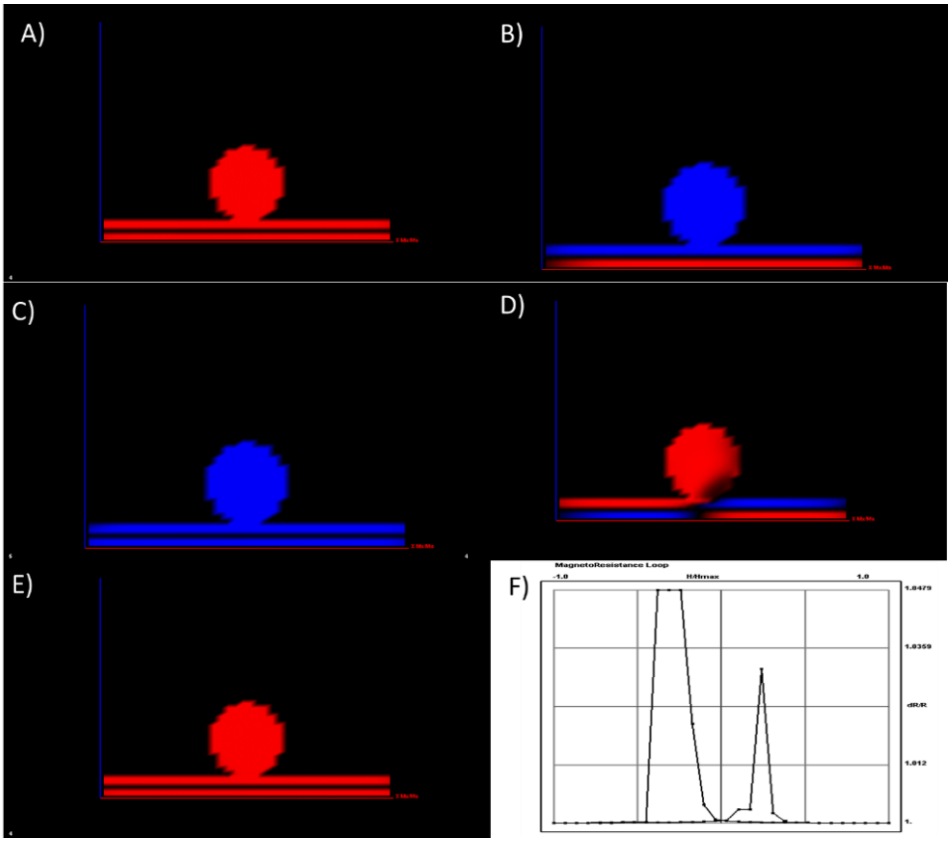

Figure 4.38: The magnetic orientation of sensor-particle model varied at five continuous states, starting from A) to E). F) The GMR profile of sensor-particle model. M_s and K_c of the 100nm particle was 280 emu/cc and 2.8×10^5 erg/cc, respectively.

Magnetic behavior was also investigated as the particle magnetic parameters M_s increased to 350 emu/cc and K_c remained at 2.0×10^5 erg/cc, as shown in Figure 4.39. Figure 4.39 A) shows the magnetization of the magnetic domains in the particle and the sensor were all saturated along the +x-direction. Magnetic domain walls appeared in both the free layer and the pinned layer as a certain strength of the external field was applied in either the +x- or –x-direction, as shown in Figure 4.39 B) and D). Besides, because of the increasing M_s, the demagnetizing field also increased, causing the reduction of the

required external field for flipping sensor layers. Though the magnetic domains in the sensor were fully saturated as the external field exceeded -200 Oe, the magnetic domains in the particle were not fully saturated especially those at the edge close to the sensor, as shown in Figure 4.39 C). Figure 4.39 E) illustrates the GMR profile of the particle-sensor model as the demagnetizing field dominated.

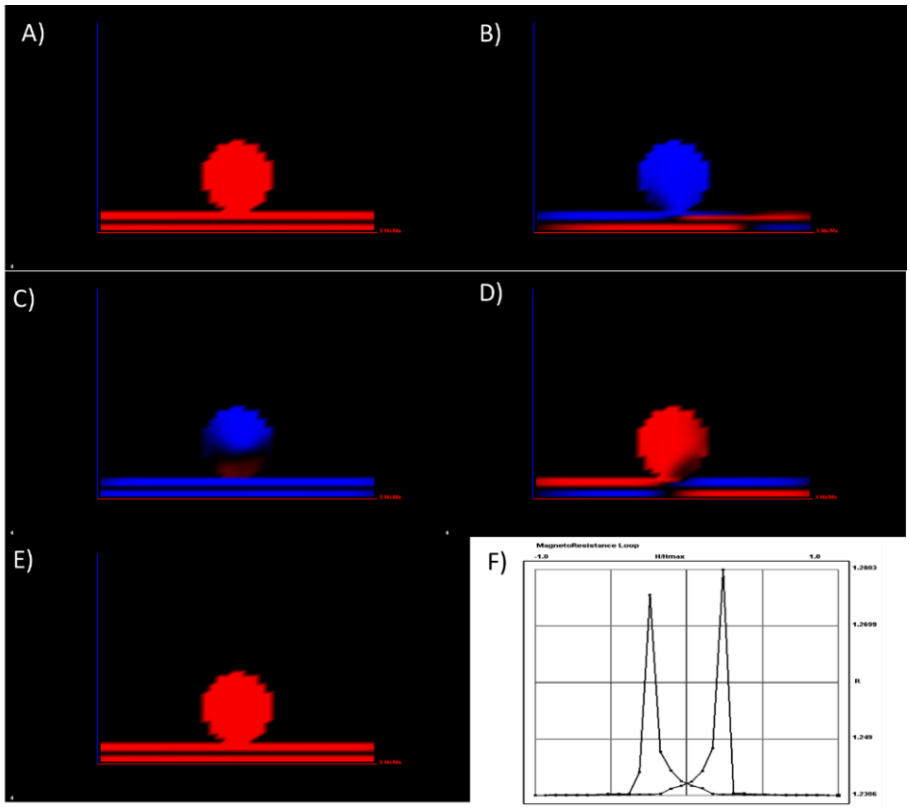

Figure 4.39: The magnetic orientation of sensor-particle model varied at five continuous states, starting from A) to E). F) The GMR profile of sensor-particle model. M_s and K_c of the 100nm particle was 350 emu/cc and 2.0×10^5 erg/cc, respectively.

From previous simulation examples, one could realize the additional interaction between the sensor and the particle increased the required external field to flip the bottom pinned layer to generate parallel orientation with the free layer, causing the significant

width increase of GMR peaks. One could also find that as domain walls appeared in the sensor, the width of GMR peaks was decreased, implying that the coercivity of the sensor was reduced. Such interaction canceled the pinning field in the pinned layer and increased the required field to flip the whole free layer. Different magnetic behaviors of the magnetic domains in the sensor were affected by exchange coupling with their neighbor domains including those in the particle.

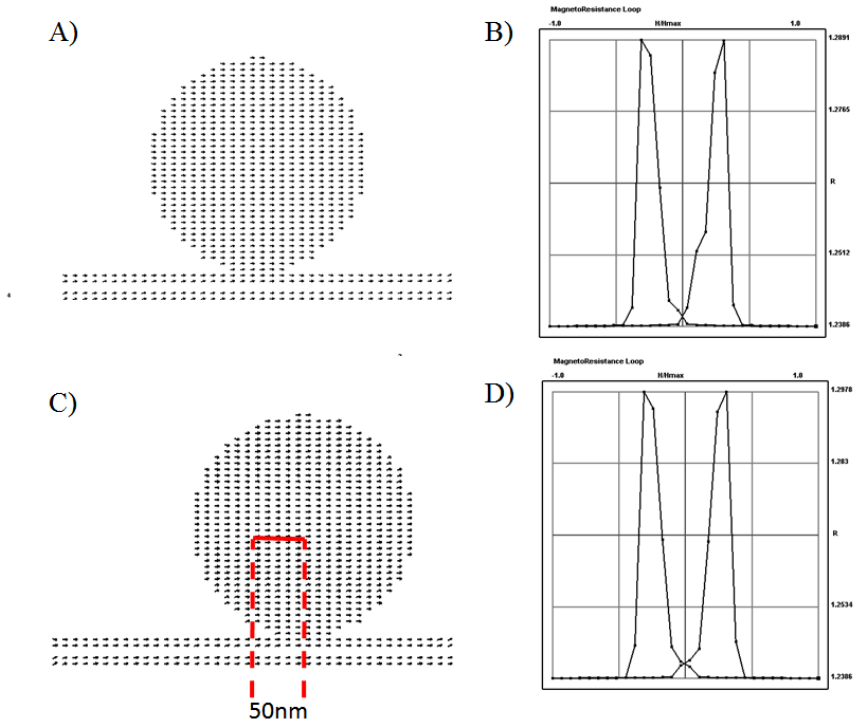

Figure 4.40: A) A 225nm particle at the center of the sensor surface. B) The GMR profile of the model in A). C) A 225nm particle locating at 50nm displacement from the center of the sensor surface. D) The GMR profile of the model in C).

To investigate the effect of various locations of the particle on top of the sensor, a 225 nm particle was created to be placed at the center of the sensor surface as well as a 50 nm displacement along the x-direction from the center. In Figure 4.40, the cross-section view

of the particle-sensor configuration at two different locations on top of the sensor and its corresponding GMR profile were illustrated. Comparing Figure 4.40 B) and D), the width and height of GMR peaks showed little difference. The only difference was no bump was presented in the peak as the field increased from zero to 30 Oe along the +x-direction.

4.5.3 Comparison of simulation result with experimental data

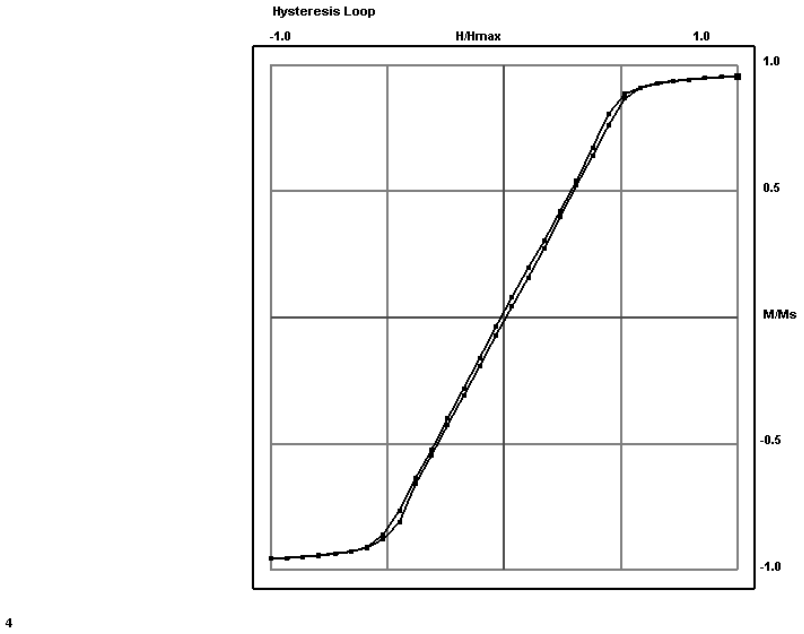

Figure 4.41: The simulated magnetization curve of the elliptical particle with M_s = 280 emu/cc and $K_c = 2.0 \times 10^5$ erg/cc.

Micro-magnetic behavior of the GMR-based sensor has been investigated and compared with experimental data in an attempt to explain the differences that occur before and after a single particle appearance. As shown in Figure 4.41, an ellipsoidal particle with a 220 nm long major axis and two 200 nm long minor axes was found to exhibit similar magnetic characteristics to those from the experimental data in Figure 4.29. The particle shape and size, H_c and M_r from the simulation result were similar to

those from the experimental data. Though the magnetization configuration above the 200 Oe external field exhibited some differences between the experimental data and the simulation result, it had little influence on particle detection scheme because the detection result was focused on the range of the external field between ±200 Oe. This particle configuration was suitable to be used in the detection model in order to verify the experimental data and explain the GMR profile change, as shown in Figure 4.42.

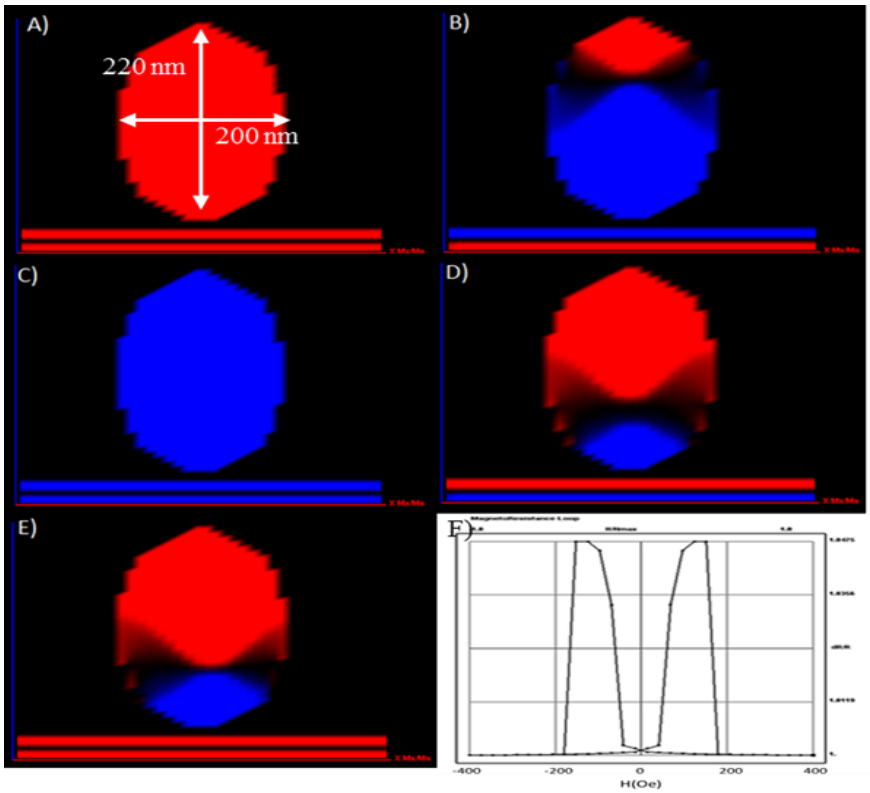

Figure 4.42: The magnetic orientation of the elliptical particle on top of the sensor at five continuous states, starting from A) to E). F) The GMR profile of the sensor-particle model. M_s and K_c of the elliptical particle was 280 emu/cc and 2.0×10^5 erg/cc, respectively.

In the GMR simulation result, approximately 170 Oe external field was required to flip the bottom Co layer to opposite direction in absence of the elliptical particle model and

190 Oe as the particle appeared on top of the sensor, as shown in Figure 4.42 E). Thus, approximately a 20 Oe increase in the external field was required to flip the pinned layer of the sensor along the external field direction in the simulation result. In the experimental data shown in Figure 4.31, approximately a 24 Oe increase in the external field was required. On the other hand, both the experimental and simulation data showed that the presence of the particle had little influence on GMR profile under near-zero field. Thus, the GMR profile change as the particle was presented in the simulation exhibited a similar trend as the particle was detected in the experiment, showing a strong agreement between the simulation and experimental results.

Chapter 5. Conclusion and Future Work

A GMR-based multi-layer stack based on a Co/Cu/Co/NiFe spin-valve design with a bottom Co layer pinned by a Co/Ru/Co synthetic antiferromagnetic (SyAF) tri-layer has been deposited. The whole multi-layer stack was successfully optimized to maximize the GMR ratio to 13% in non-patterned films. Fabrication processes for a self-aligned contact technique using the PHOST/PMGI bilayer resist system were established. A 110 nm undercut length was successfully generated on the PMGI layer. Lithographic processes using a combination of e-beam and UV lithography to fabricate twelve 400 nm × 400 nm or 200 nm × 400 nm sensors and paired contacts on a chip were presented and verified.

Fe_3O_4 ferrimagnetic nanoparticles, 50 nm, 100nm and 225 nm in diameter, were successfully detected by the GMR-based sensor in different schemes. The detection of a single 225nm Fe_3O_4 nanoparticle landing on a GMR-based sensor was presented. The GMR peak is 24 Oe wider on the external field axis than the GMR peak corresponding to the sensor without any particles attached. This result demonstrated that the sensor coercivity increased from 48 Oe to 60 Oe as well as presented the capability of our spin-valve based biosensor to detect a single magnetic particle.

In the sensor corrosion test, it was first verified that there was not a significant change in the GMR profile before and after a passivation layer was deposited on the sensing area. Besides, evidence showed a 25nm thick Al_2O_3 passivation layer deposited on top of the sensing area effectively protected the sensor from being damaged by the PBS solution and reduced the resistance increase after the PBS solution was introduced.

The finite-element simulation based on the Landau-Lifshitz-Gilbert equation

demonstrated behaviors of magnetic domains of the free layer and pinned layer in the sensor associated with the presence of a Fe_3O_4 nanoparticle with various magnetic characteristics. The particle size, shape, M_s, K_c, and magnetic exchange coupling at the interface between the nanoparticle and the free layer were verified to have various degrees of influence on the sensor GMR profile diversification. A particle-sensor model with similar characteristics to those in the particle detection experiment exhibited a similar trend to the GMR change in which the width of the GMR peaks were at least 20 Oe wider than those corresponding to the sensor-only model. Therefore, a strong consistency in the established sensing model and experimental data was observed.

So far, the particle distribution method we use can only allow a relatively low probability of particles landing on the desired region. The particle distribution method can be improved by designing an approach that is able to wipe out non-sensing-area binding and enhance the probability of particles landing on the sensing area. One of the doable methods involving the mask design, UV lithography, and the lift-off processes are shown in Figure 5.1. A chip comprised of a fully developed sensor array will be prepared. A 1μm thick AZ-1512 photoresist will be spin-coated on the chip, followed by the UV lithography process. Twelve 2 μm × 2 μm square patterns will be overlapped on top of the twelve sensing areas. The chip will be developed in 2.2% TMAH. Appropriate amount of magnetic nanoparticles will be distributed on the chip randomly after development of AZ-1512, followed by a lift-off process using acetone. Particles which do not locate in the twelve square pattern regions will be washed out during the lift-off process. Few or single particles landing in those square patterns are constrained in a micro-scale area and hence increase the portion of the particle only attaching on sensing

area.

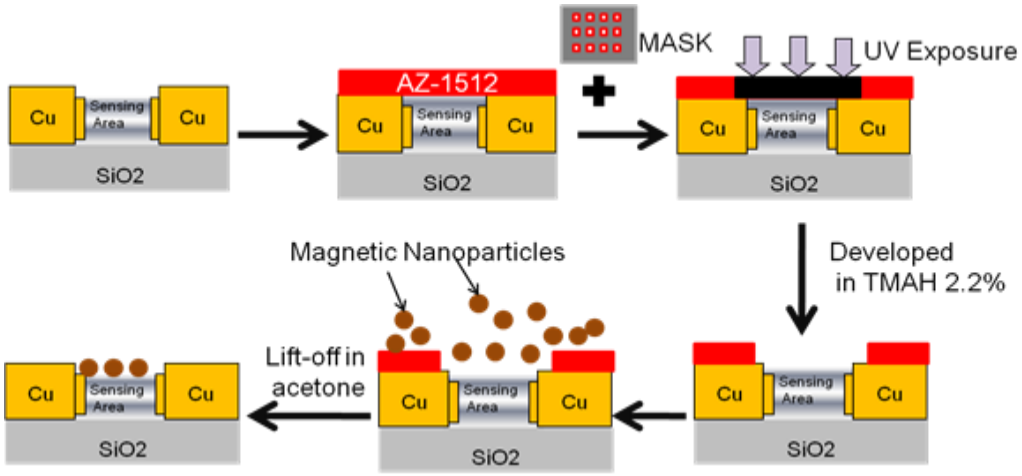

Figure 5.1: The scheme of distribution of nanoparticles in confined micro-scale area using UV lithography technique.

In the long-term future work, more knowledge in biochemistry is needed for sensing bio-conjugated magnetic particles. In order to verify the final sensing capability of a functionalized magnetic particle, strategy has to be developed involving the immobilization of biomolecules on nanoparticles and its corresponding binding targets on the sensing area of the sensor, followed by the magnetic pull-off technique used to remove non-specific binding particles. In addition, numbers and sizes of biomolecules need to be comparable to magnetic nanoparticles so that the detection strategy based on the GMR biosensing can be feasible.

References

[1] Ferreira, H. A., Graham, D. L., Freitas, P. P., & Cabral, J. M. S. (2003). Biodetection using magnetically labeled biomolecules and arrays of spin-valve sensors (invited). *Journal of Applied Physics*, 93(10), 7281-7286. doi: Doi 10.1063/1.1544449

[2] Kasatkin, S. I., Vasil'eva, N. P., & Murav'ev, A. M. (2010). Biosensors based on the thin-film magnetoresistive sensors. *Automation and Remote Control*, 71(1), 156-166.

[3] Xu, L., Yu, H., Akhras, M. S., Han, S. J., Osterfeld, S., White, R. L., Wang, S. X. (2008). Giant magnetoresistive biochip for DNA detection and HPV genotyping. *Biosensors & Bioelectronics*, 24(1), 99-103. doi: DOI 10.1016/j.bios.2008.03.030

[4] Graham, D. L., Ferreira, H., Bernardo, J., Freitas, P. P., & Cabral, J. M. S. (2002). Single magnetic microsphere placement and detection on-chip using current line designs with integrated spin valve sensors: Biotechnological applications. *Journal of Applied Physics*, 91(10), 7786-7788.

[5] De Palma, R., Reekmans, G., Liu, C., Wirix-Speetjens, R., Laureyn, W., Nilsson, O., & Lagae, L. (2007). Magnetic bead sensing platform for the detection of proteins. *Analytical chemistry*, 79(22), 8669-8677.

[6] Tamanaha, C. R., Mulvaney, S. P., Wahowski, K. A., Tondra, M. C., Whitman, L. J., & Colton, R. J. (2003). Cellular Genomic Analysis with GMR Sensor Arrays. NAVAL RESEARCH LAB WASHINGTON DC.

[7] Graham, D. L., Ferreira, H. A., Feliciano, N., Freitas, P. P., Clarke, L. A., &

Amaral, M. D. (2005). Magnetic field-assisted DNA hybridisation and simultaneous detection using micron-sized spin-valve sensors and magnetic nanoparticles. *Sensors and Actuators B: Chemical*, 107(2), 936-944.

[8] Han, S. J., & Wang, S. (2010). Magnetic Nanotechnology for Biodetection.*Journal of The Association for Laboratory Automation*, 15(2), 93-98.

[9] Choi, J. W., Oh, K. W., Thomas, J. H., Heineman, W. R., Halsall, H. B., Nevin, J. H., ... & Ahn, C. H. (2002). An integrated microfluidic biochemical detection system for protein analysis with magnetic bead-based sampling capabilities.*Lab on a Chip*, 2(1), 27-30.

[10] Inomata, K. (1998). Giant magnetoresistance and its sensor applications. *Journal of electroceramics*, 2(4), 283-293.

[11] Daughton, J. M. (1999). GMR applications. *Journal of Magnetism and Magnetic Materials*, 192(2), 334-342.

[12] Leal, J. L., & Kryder, M. H. (1998). Spin valves exchange biased by Co/Ru/Co synthetic antiferromagnets. *Journal of applied physics*, 83(7), 3720-3723.

[13] Parkin, S. S. P., More, N., & Roche, K. P. (1990). Oscillations in exchange coupling and magnetoresistance in metallic superlattice structures: Co/Ru, Co/Cr, and Fe/Cr. *Physical Review Letters*, 64(19), 2304.

[14] Zhu, J. G. (1999). Spin valve and dual spin valve heads with synthetic antiferromagnets. *Magnetics, IEEE Transactions on*, 35(2), 655-660.

[15] Dimitrov, D. V., Van Ek, J., Li, Y. F., & Xiao, J. Q. (2000). Enhanced magnetic stability in spin valves with synthetic antiferromagnet. *Journal of Applied*

Physics, 87(9), 6427-6429.

[16] Takenaga, T., Kuroiwa, T., Furukawa, T., Taki, M., Yoshiara, K., & Tokuda, Y. (2006). Thermal robustness in synthetic antiferromagnetic free layer for magnetic random access memory applications. *Journal of applied physics*,99(8), 08C911-08C911.

[17] Parat, K. K., Wada, G. N., Atwood, G. E., & Tang, D. N. (1998). *U.S. Patent No. 5,731,242*. Washington, DC: U.S. Patent and Trademark Office.

[18] Hisamoto, D., Lee, W. C., Kedzierski, J., Takeuchi, H., Asano, K., Kuo, C., & Hu, C. (2000). FinFET-a self-aligned double-gate MOSFET scalable to 20 nm. *Electron Devices, IEEE Transactions on*, 47(12), 2320-2325.

[19] Yang, H., Jin, A., Luo, Q., Li, J., Gu, C., & Cui, Z. (2008). Electron beam lithography of HSQ/PMMA bilayer resists for negative tone lift-off process. *Microelectronic Engineering*, 85(5), 814-817.

[20] Chen, W. S., Gu, P. Y., Kao, M. J., & Tsai, M. J. (2008, March). Gap-fill type HSQ/ZEP520A bilayer resist process-(II): HSQ island and spacer formation. InAdvanced Lithography (pp. 69232Y-69232Y). *International Society for Optics and Photonics*.

[21] Duan, H., Hu, H., Hui, H. K., Shen, Z., & Yang, J. K. (2013). Free-standing sub-10 nm nanostencils for the definition of gaps in plasmonic antennas.*Nanotechnology*, 24(18), 185301.

[22] Van Delft, F. C. (2002). Delay-time and aging effects on contrast and sensitivity of hydrogen silsesquioxane. *Journal of Vacuum Science & Technology B: Microelectronics and Nanometer Structures*, 20(6), 2932-2936.

[23] de Meftahi, M. V., & Fréchet, J. M. (1988). Study of the compatibility of blends of polymers and copolymers containing styrene, 4-hydroxystyrene and 4-vinylpyridine. *Polymer*, 29(3), 477-482.

[24] Lee, S. M., Frechet, J. M., & Willson, C. G. (1994). Photocrosslinking of Poly (4-hydroxystyrene) via Electrophilic Aromatic Substitution: Use of Polyfunctional Benzylic Alcohols in the Design of Chemically Amplified Resist Materials with Tunable Sensitivities. *Macromolecules*, 27(18), 5154-5159.

[25] Wallraff, G. M., Medeiros, D. R., Sanchez, M., Petrillo, K., Huang, W. S., Rettner, C.,& Bucchignano, J. (2004). *Journal of Vacuum Science & Technology B: Microelectronics and Nanometer Structures*, 22(6), 3479-3484.

[26] Golden, J., Miller, H., Nawrocki, D., & Ross, J. (2009). Optimization of Bi-layer Lift-Off Resist Process. *CS Mantech Technical Digest*.

[27] Wu, G., Ji, H., Hansen, K., Thundat, T., Datar, R., Cote, R., & Majumdar, A. (2001). Origin of nanomechanical cantilever motion generated from biomolecular interactions. *Proceedings of the National Academy of Sciences*, 98(4), 1560-1564.

[28] Hsing, I., Xu, Y., & Zhao, W. (2007). Micro- and Nano-Magnetic Particles for Applications in Biosensing. *Electroanalysis*, 19(7-8), 755-768.

[29] Horak, D., Babič, M., Mackova, H., & Beneš, M. J. (2007). Preparation and properties of magnetic nano-and microsized particles for biological and environmental separations. *Journal of separation science*, 30(11), 1751-1772.

[30] Deng, H., Li, X., Peng, Q., Wang, X., Chen, J., & Li, Y. (2005). Monodisperse Magnetic Single-Crystal Ferrite Microspheres. *Angewandte Chemie*, 117(18), 2842-2845.

[31] Sun, S., & Zeng, H. (2002). Size-controlled synthesis of magnetite nanoparticles. Journal of the American Chemical Society, 124(28), 8204-8205.

[32] Kang, Y. S., Risbud, S., Rabolt, J. F., & Stroeve, P. (1996). Synthesis and characterization of nanometer-size Fe3O4 and γ-Fe2O3 particles. *Chemistry of Materials*, 8(9), 2209-2211.

[33] Wang, S. X., & Li, G. (2008). Advances in giant magnetoresistance biosensors with magnetic nanoparticle tags: review and outlook. *Magnetics, IEEE Transactions on*, 44(7), 1687-1702.

[34] Baibich, M. N., Broto, J. M., Fert, A., Van Dau, F. N., Petroff, F., Etienne, P., ... & Chazelas, J. (1988). Giant magnetoresistance of (001) Fe/(001) Cr magnetic superlattices. *Physical Review Letters*, 61(21), 2472.

[35] Binasch, G., Grünberg, P., Saurenbach, F., & Zinn, W. (1989). Enhanced magnetoresistance in layered magnetic structures with antiferromagnetic interlayer exchange. *Physical review B*, 39, 4828-4830.

[36] Grünberg, P., Schreiber, R., Pang, Y., Brodsky, M. B., & Sowers, H. (1986). Layered magnetic structures: Evidence for antiferromagnetic coupling of Fe layers across Cr interlayers. *Physical Review Letters*, 57(19), 2442.

[37] Chappert, C., Fert, A., & Van Dau, F. N. (2007). The emergence of spin electronics in data storage. *Nature materials*, 6(11), 813-823.

[38] Schad, R., Potter, C. D., Belien, P., Verbanck, G., Moshchalkov, V. V., & Bruynseraede, Y. (1994). Giant magnetoresistance in Fe/Cr superlattices with very thin Fe layers. *Applied physics letters*, 64(25), 3500-3502.

[39] Mosca, D. H., Petroff, F., Fert, A., Schroeder, P. A., Pratt Jr, W. P., & Laloee, R.

(1991). Oscillatory interlayer coupling and giant magnetoresistance in Co/Cu multi-layers. *Journal of magnetism and magnetic materials*, 94(1), L1-L5.

[40] Kamiguchi, Y., Saito, K., Iwasaki, H., Sahashi, M., Ouse, M., & Nakamura, S. (1996). Giant magnetoresistance and soft magnetic properties of Co 90 Fe 10/Cu spin-valve structures. *Journal of applied physics*, 79(8), 6399-6401.

[41] Dieny, B., Speriosu, V. S., Metin, S., Parkin, S. S., Gurney, B. A., Baumgart, P., & Wilhoit, D. R. (1991). Magnetotransport properties of magnetically soft spin-valve structures. *Journal of Applied Physics*, 69(8), 4774-4779.

[42] Chopra, H. D., Hockey, B. J., Chen, P. J., Egelhoff, W. F., Wuttig, M., & Hua, S. Z. (1997). Nanostructural considerations in giant magnetoresistive Co-Cu-based symmetric spin valves. *Physical Review B*, 55(13), 8390.

[43] Coehoorn, R., Kools, J. C. S., Rijks, T. G., & Lenssen, K. M. (1998). Giant magnetoresistance materials for read heads. *Philips journal of research*, 51(1), 93-124.

[44] Van Driel, J., De Boer, F. R., Coehoorn, R., Rietjens, G. H., & Heuvelmans-Wijdenes, E. S. J. (2000). Magnetorefractive and magnetic-linear-dichroism effect in exchange-biased spin valves. *Physical Review B*, 61(22), 15321.

[45] Uji, K. F. (1990). Large magnetoresistance of field-induced giant ferrimagnetic multi-layers. *Journal of the Physical Society of Japan*, 59(9), 3061-3064.

[46] Dupas, C., Beauvillain, P., Chappert, C., Renard, J. P., Trigui, F., Veillet, P., & Renard, D. (1990). Very large magnetoresistance effects induced by antiparallel magnetization in two ultrathin cobalt films. *Journal of Applied Physics*, 67(9), 5680-5682.

[47] Tsang, C., Fontana, R. E., Lin, T., Heim, D. E., Speriosu, V. S., Gurney, B. A., & Williams, M. L. (1994). Design, fabrication and testing of spin-valve read heads for high density recording. *Magnetics, IEEE Transactions on*, 30(6), 3801-3806.

[48] Mao, S., Linville, E., Nowak, J., Zhang, Z., Chen, S., Karr, B., ... & Ryan, P. (2004). Tunneling magnetoresistive heads beyond 150 Gb/in^2. *Magnetics, IEEE Transactions on*, 40(1), 307-312.

[49] Nakamoto, K., Hoshiya, H., Katada, H., Okada, T., Hatatani, M., Hoshino, K., ... & Watanabe, K. (2005). CPP-GMR reader and wraparound shield writer for perpendicular recording. *Magnetics, IEEE Transactions on*, 41(10), 2914-2919.

[50] Nagasaka, K. (2009). CPP-GMR technology for magnetic read heads of future high-density recording systems. *Journal of Magnetism and Magnetic Materials*,321(6), 508-511.

[51] Rife, J. C., Miller, M. M., Sheehan, P. E., Tamanaha, C. R., Tondra, M., & Whitman, L. J. (2003). Design and performance of GMR sensors for the detection of magnetic microbeads in biosensors. *Sensors and Actuators A: Physical*, 107(3), 209-218.

[52] Seigler, M. A. (2006). *U.S. Patent No. 7,019,371*. Washington, DC: U.S. Patent and Trademark Office.

[53] Nozieres, J. P., Jaren, S., Zhang, Y. B., Zeltser, A., Pentek, K., & Speriosu, V. S. (2000). Blocking temperature distribution and long-term stability of spin-valve structures with Mn-based antiferromagnets. *Journal of Applied Physics*, 87(8), 3920-3925.

[54] Dimitrov, D. V., Van Ek, J., Li, Y. F., & Xiao, J. Q. (2000). Enhanced magnetic

stability in spin valves with synthetic antiferromagnet. *Journal of Applied Physics*, 87(9), 6427-6429.

[55] Lee, Y. M., Ando, Y., Miyazaki, T., & Kubota, H. (2007). Reduction of switching fields of submicrometer sized magnetic tunnel junction with NiFe-based synthetic ferrimagnetic free layer. *Journal of applied physics*, 101(2), 023905-023905.

[56] Ruderman, M. A., & Kittel, C. (1954). Indirect exchange coupling of nuclear magnetic moments by conduction electrons. *Physical Review*, 96(1), 99.

[57] Kasuya, T. (1956). A theory of metallic ferro-and antiferromagnetism on Zener's model. *Progress of theoretical physics*, 16(1), 45-57.

[58] Shieh, R., & Ackley, D. (1997). *WIPO Patent No. 1997045740*. Geneva, Switzerland: World Intellectual Property Organization.

[59] Baselt, D. R., Lee, G. U., Natesan, M., Metzger, S. W., Sheehan, P. E., & Colton, R. J. (1998). A biosensor based on magnetoresistance technology. *Biosensors and Bioelectronics*, 13(7), 731-739.

[60] Dieny, B. (1994). Giant magnetoresistance in spin-valve multi-layers. *Journal of Magnetism and Magnetic Materials*, 136(3), 335-359.

[61] Wang, S. X., Li, G. X., Sun, S. H., Wilson, R. J., White, R. L., & Pourmand, N. (2006). Spin-valve sensors for ultrasensitive detection of superparamagnetic nanoparticles for biological applications. *Sensors and Actuators a-Physical*, 126(1), 98-106.

[62] Li, G. X., Sun, S. H., Wilson, R. J., White, R. L., Pourmand, N., & Wang, S. X. (2006). Spin valve sensors for ultrasensitive detection of superparamagnetic

nanoparticles for biological applications. *Sensors and Actuators a-Physical*, 126(1), 98-106. doi: DOI 10.1016/j.sna.2005.10.001

[63] Li, G. X., Sun, S. H., & Wang, S. X. (2006). Spin valve biosensors: Signal dependence on nanoparticle position. *Journal of Applied Physics*, 99(8).

[64] Li, G. X., Joshi, V., White, R. L., Wang, S. X., Kemp, J. T., Webb, C., . . . Sun, S. H. (2003). Detection of single micron-sized magnetic bead and magnetic nanoparticles using spin valve sensors for biological applications. *Journal of Applied Physics*, 93(10), 7557-7559. doi: Doi 10.1063/1.1540176

[65] Young, H. D. (1992). *University Physics*. Massachusetts: Addison-Wesley.

[66] Pippard, A. B. (1989). *Magentoresistance in Metals* (Vol. 2). Cambridge University Press.

[67] Fuke, H. N., Saito, K., Kamiguchi, Y., Iwasaki, H., & Sahashi, M. (1997). Spin-valve giant magnetoresistive films with antiferromagnetic Ir-Mn layers.*Journal of applied physics*, *81*(8), 4004-4006.

[68] Egelhoff, W. F., Ha, T., Misra, R. D. K., Kadmon, Y., Nir, J., Powell, C. J., ... & Brug, J. A. (1995). Magnetoresistance values exceeding 21% in symmetric spin valves. *Journal of applied physics*, *78*(1), 273-277.

[69] Xue, S. S., He, Q. I., Wang, H., Duxstad, K. J., & Hintz, M. B. (2001). *U.S. Patent No. 6,278,592*. Washington, DC: U.S. Patent and Trademark Office.

[70] Brainard, R. L., Henderson, C., Cobb, J., Rao, V., Mackevich, J. F., Okoroanyanwu, U., ... & Connolly, S. (1999). Comparison of the lithographic properties of positive resists upon exposure to deep-and extreme-ultraviolet radiation. *Journal of Vacuum Science & Technology B: Microelectronics and*

Nanometer Structures, *17*(6), 3384-3389.

[71] Lorenz, H., Despont, M., Fahrni, N., LaBianca, N., Renaud, P., & Vettiger, P. (1997). SU-8: a low-cost negative resist for MEMS. *Journal of Micromechanics and Microengineering*, *7*(3), 121.

[72] Chen, Y., Peng, K., & Cui, Z. (2004). A lift-off process for high resolution patterns using PMMA/LOR resist stack. *Microelectronic engineering*, *73*, 278-281.

[73] Tam, G. (1989). *U.S. Patent No. 4,814,258*. Washington, DC: U.S. Patent and Trademark Office.

[74] Brody, J. P., & Yager, P. (1997). Diffusion-based extraction in a microfabricated device. *Sensors and Actuators A: Physical*, *58*(1), 13-18.

[75] Chen, W., & Ahmed, H. (1993). Fabrication of 5–7 nm wide etched lines in silicon using 100 keV electron-beam lithography and polymethylmethacrylate resist. *Applied physics letters*, *62*(13), 1499-1501.

[76] Zailer, I., Frost, J. E. F., Chabasseur-Molyneux, V., Ford, C. J. B., & Pepper, M. (1996). Crosslinked PMMA as a high-resolution negative resist for electron beam lithography and applications for physics of low-dimensional structures.*Semiconductor science and technology*, *11*(8), 1235.

[77] Chou, S. Y., Krauss, P. R., Zhang, W., Guo, L., & Zhuang, L. (1997). Sub-10 nm imprint lithography and applications. *Journal of Vacuum Science & Technology B: Microelectronics and Nanometer Structures*, *15*(6), 2897-2904.

[78] Brewer, G. (Ed.). (1980). *Electron-beam technology in microelectronic fabrication*. Academic press.

[79] Owen, G., & Rissman, P. (1983). Proximity effect correction for electron beam lithography by equalization of background dose. *Journal of Applied Physics*,*54*(6), 3573-3581.

[80] Quirk, M., & Serda, J. (2001). *Semiconductor manufacturing technology* (Vol. 1). NJ, USA: Prentice Hall.

[81] Kern, W. (1991). *Thin film processes II* (Vol. 2). Access Online via Elsevier.

[82] Dennis, J. O., Ahmad, F., & Khir, M. H. (2013). *CMOS Compatible Bulk Micromachining*.

[83] Patnaik, P. (2003). *Handbook of inorganic chemicals* (Vol. 28). New York: McGraw-Hill.

[84] Litvinov, J., Wang, Y. J., George, J., Chinwangso, P., Brankovic, S., Willson, R. C., & Litvinov, D. (2013). Development of pinhole-free amorphous aluminum oxide protective layers for biomedical device applications. *Surface and Coatings Technology*.

[85] Liu, Z., Wang, Y. J., Litvinov, J., Chinwangso, P., Willson, R., & Litvinov, D. (2011). Corrosion Inhibitor for Use in Giant Magnetoresistance (GMR) Biosensors. *ECS Transactions*, *33*(30), 103-111.

[86] Landau, L. D., Lifshitz, E. M., Sykes, J. B., Reid, W. H., & Dill, E. H. (1960). Theory of Elasticity: Vol. 7 of Course of Theoretical Physics. *Physics Today*,*13*, 44.

[87] Gilbert, T. L. (2004). A phenomenological theory of damping in ferromagnetic materials. *Magnetics, IEEE Transactions on*, *40*(6), 3443-3449.

[88] Ross, C. A. (2001). Patterned magnetic recording media. *Annual Review of*

Materials Research, *31*(1), 203-235.

[89] Yang, B., & Fredkin, D. R. (1996). Dynamical micromagnetics of a ferromagnetic particle: Numerical studies. *Journal of applied physics*, *79*(8), 5755-5757.

[90] Scheinfein, M. R., & Price, E. (1998). LLG micromagnetics simulator. *Tempe, AZ USA, 85282*.